# The finite element method and convergence theory for the EEG forward problem solution

Institute for Biomagnetism and Biosignalanalysis

Westfälische Wilhelms-Universität Münster


Carsten H. Wolters

Institut für Biomagnetismus und Biosignalanalyse, Westf. Wilhelms-Universität Münster, Germany


*Lectures on Nov.19+26, 2024*

# Saint Venant source modeling approach

# The Venant source model

$$\begin{aligned} \nabla \cdot (\sigma \nabla u_{dip}) &= \nabla \cdot (\overrightarrow{M}\ \delta_{x_0}(x)) \quad \text{in } \Omega \\ \sigma \nabla u_{dip} \cdot n &= 0 \quad \text{on } \partial\Omega. \end{aligned}$$

Instead we now want to compute $u_{mon}$ for the monopole problem and solve

$$\begin{aligned} \nabla \cdot (\sigma \nabla u_{mon}) &= \sum_{i=1}^{n} q_i\ \ \delta_{x_i}(x) \quad \text{in } \Omega \\ \sigma \nabla u_{mon} \cdot n &= 0 \quad \text{on } \partial\Omega. \end{aligned}$$

$$\Delta x_i = x_i - x_0$$

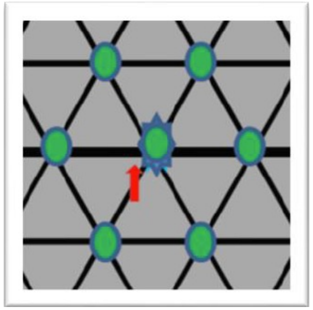

for $u_{mon}$.

The $u$ symbolizes the electric potential. In the first equation $u_{dip}$ is the electric potential of the dipole and in the second equation $u_{mon}$ is the electric potential of a monopole distribution.

Those potentials should be the same. To ensure this, we use Multipole expansion to expand the dipole potential and the monopole distribution potential.

[Hanrath, *Dissertation in Maths, RWTH Aachen*, 2019]

# The Venant source model

For this, we require the assumption

**Assumption 4.** *Let* $\mathbb{R}^+$. *Let* $x_1, \ldots, x_n, x_+, x_- \in \Omega_h$ *fulfill that a small ball around the origin with radius* $\delta \in \mathbb{R}^{>0}$ *exists such that* $x_1, \ldots, x_n \in B_\delta(0) := \{x \in \Omega_h \mid |x| < \delta\}$ *and a* $\sigma_0 \in \mathbb{R}^+$ *such that*

$$\sigma(x) = \sigma_0 \text{ for all } x \in B_\delta(0). \tag{3.3.1}$$

*We define* $\delta_0$ *as the maximal* $\delta \in \mathbb{R}$ *such that* (3.3.1) *holds.*

We will also need the definition

**Definition 4.** *For the expansion of the monopole distribution we define*

$$\delta_1 := \inf\{\delta \in \mathbb{R} \mid \delta_0 \geq \delta_1 > \max\{|x_1|, \ldots, |x_n|\}\}. \tag{3.3.2}$$

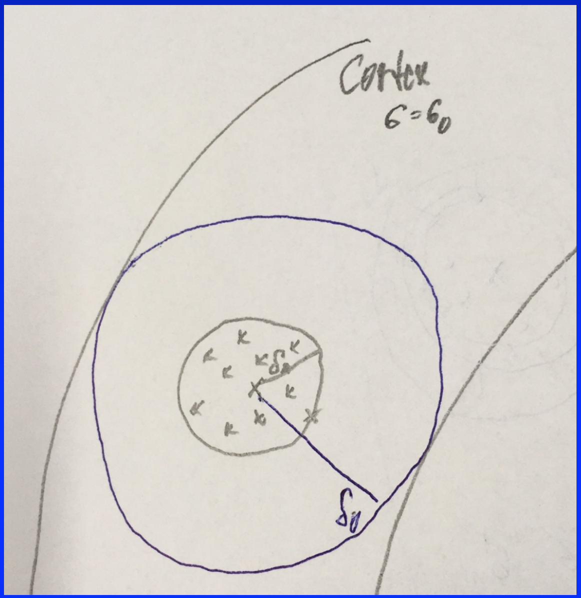


So we choose the norm

$$\|v\|_* := \|v\|_{L_2(B_{\delta_0}(0) \setminus B_{\delta_1}(0))}. \tag{3.3.3}$$

[Hanrath, *Dissertation in Maths, RWTH Aachen*, 2019]

# The Venant source model

The potential of the dipole, which is also the solution of 2, can be represented by the fundamental solution

$$\Phi_{\mathrm{D}}(x) = \frac{1}{4\pi\sigma_0} \cdot \frac{\langle \overrightarrow{M}, x\rangle}{|x|^3}. \tag{3.3.4}$$

This potential is a pure dipole potential and cannot be expanded further. Every moment except the dipole moment is zero.
The potential of the monopole distribution is

$$\Phi_{\mathrm{M}}(x) = \frac{1}{4 \cdot \sigma_0 \pi} \cdot \sum_{i=1}^{n} \frac{q_i}{\|x - x_i\|_2}. \tag{3.3.5}$$

# The Venant source model

Multipole expansion transforms the potential of the monopole distribution into an infinite sum, where every summand is the respective higher order moment [31]. We then can conclude with the definitions of the scalar product and the $l_2$-Norm, that

$$\frac{1}{\|x - x_i\|_2} = (|x|^2 + |x_i|^2 - 2\langle x_i, x\rangle)^{-1/2}$$
$$= |x|^{-1}\left(1 + \frac{|x_i|^2}{|x|^2} - \frac{\langle 2 \cdot x_i, x\rangle}{|x|^2}\right)^{-1/2}$$

for all $i \in \{1, \ldots, n\}$.
With the last factor we have used the Taylor expansion with the simplified function $(1 + y)^{-1/2}$, where we substituted $\frac{|x_i|^2}{|x|^2} - \frac{\langle 2 \cdot x_i, x\rangle}{|x|^2}$ with $y$.
This Taylor expansion can be used only for $y < 1$, which means that $|x| \gg |x_i|$ must hold.
Inserting and re-substituting gives the expression

$$\Phi_{\mathrm{M}}(x) = \frac{1}{4\pi\sigma_0} \sum_{l=1}^{\infty} \sum_{i=1}^{n} \frac{q_i \cdot |x_i|^l}{|x|^{l+1}} \mathcal{P}_l(\cos(\theta_i)), \tag{3.3.6}$$

where $\mathcal{P}_l(x)$ are the *Legendre Polynomials* of order $l \in \mathbb{N}$ and $\theta_i$ is the angle between the position vectors of the evaluation point $x$ and the monopole location $x_i$.

[Hanrath, *Dissertation in Maths, RWTH Aachen*, 2019]

# The Venant source model

Ideally, we would then want to compute the strength of the monopole distribution in such a way that the potentials are the same.

This would mean to solve the problem

**Problem 6.** *Given are the monopole locations* $x_1, \ldots, x_n$ *and the dipole potential* $\Phi_D$*. Compute* $q_1, \ldots, q_n$ *such that*

$$\|\Phi_D - \Phi_M\|_* = \min_{(\tilde{q}_1, \ldots, \tilde{q}_n)} \left\| \frac{1}{4\pi\sigma_0} \cdot \frac{\langle \overrightarrow{M}, x\rangle}{|x|^3} - \frac{1}{4\pi\sigma_0} \sum_{l=1}^{\infty} \sum_{i=1}^{n} \frac{\tilde{q}_i \cdot |x_i|^l}{|x|^{l+1}} \mathcal{P}_l(cos(\theta_i)) \right\|_* .$$

We can minimize the norm with the help of comparing the coefficients of both expansions.

Unfortunately, this would require solving an infinite sum of equations.

# The Venant source model

To compute the loads $q_i$ with a computable algorithm, we have to reduce the problem to a finite number of sums.

The dipole potential contains only the second order term – every other term is equal to zero. Terms within the monopole expansion decay with at least $\frac{1}{\delta_0^l}$. Hence, the decision to cut the potential of the monopoles after the third term seems reasonable. What remains is to compute $q_1, \ldots, q_n$ fulfilling

$$\left\| \Phi_D(x) - \frac{1}{4\pi\sigma_0} \sum_{l=0}^{2} \sum_{i=1}^{n} \frac{q_i \cdot |x_i|^l}{|x|^{l+1}} \mathcal{P}_l(cos(\theta_i)) \right\|_* \rightarrow min.$$

Let $\tilde{\Phi}_M(x) := \frac{1}{4\pi\sigma_0} \sum_{l=0}^{2} \sum_{i=1}^{n} \frac{q_i \cdot |x_i|^l}{|x|^{l+1}} \mathcal{P}_l(\cos(\theta_i))$. With the definition of the scalar product we acquire

$$\begin{aligned} \tilde{\Phi}_{\mathrm{M}}(x) = & \frac{1}{4\pi\sigma_0|x|} \sum_{i=1}^{n} q_i \\ & + \frac{1}{4\pi\sigma_0|x|^2} \left\langle \sum_{i=1}^{n} q_i \cdot x_i, \frac{x}{|x|} \right\rangle \\ & + \frac{1}{4\pi\sigma_0 2|x|^3} \left\langle \frac{x}{|x|}, \frac{\sum_{i=1}^{n} q_i \ \left(3x_i \otimes x_i - |x_i|^2 \ I_{3\times 3}\right)}{2} \frac{x}{|x|} \right\rangle. \end{aligned}$$

Die ersten Legendre-Polynome lauten:

$$P_0(x) = 1$$
$$P_1(x) = x$$
$$P_2(x) = \frac{1}{2}(3x^2 - 1)$$

[Hanrath, *Dissertation in Maths, RWTH Aachen*, 2019]

# The Venant source model

If one then compares both potentials, one has to fulfill the following conditions:

$$
\begin{aligned}
0 &= \frac{1}{4\pi\sigma_0|x|} \sum_{i=1}^{n} q_i \\
\frac{1}{4\pi\sigma_0}\frac{\langle \overrightarrow{M}, x\rangle}{|x|^3} &= \frac{1}{4\pi\sigma_0|x|^2} \left\langle \sum_{i=1}^{n} q_i x_i, \frac{x}{|x|} \right\rangle \qquad (3.3.7)\\
0 &= \frac{1}{4\pi\sigma_0 2|x|^3} \left\langle \frac{x}{|x|}, \frac{\sum_{i=1}^{n} q_i \left(3x_i \otimes x_i - |x_i|^2 I_{3\times 3}\right)}{2} \cdot \frac{x}{|x|} \right\rangle.
\end{aligned}
$$

These conditions should hold for all $x \in \Omega$, so they are transformed into equations independent of $x$, namely

$$
\begin{aligned}
0 &= \sum_{i=1}^{\mathrm{n}} q_i \\
\overrightarrow{M} &= \sum_{i=1}^{\mathrm{n}} q_i x_i \qquad (3.3.8)\\
0_{3x3} &= \sum_{i=1}^{\mathrm{n}} \frac{q_i}{2} \left(3x_i \otimes x_i - |x_i|^2 I_{3\times 3}\right)
\end{aligned}
$$

[Hanrath, *Dissertation in Maths, RWTH Aachen*, 2019]

# The Venant source model

We can interpret these conditions as linear equations of $q_1, \dots, q_n$ and thus we get a matrix $\bar{X}$ and vectors $\overrightarrow{q}$ and $\overrightarrow{t}$ such that

$$\underbrace{\begin{pmatrix} 0 \\ \overrightarrow{M}_1 \\ \overrightarrow{M}_2 \\ \overrightarrow{M}_3 \\ 0 \\ \vdots \\ 0 \end{pmatrix}}_{=:\overrightarrow{t}} = \underbrace{\begin{pmatrix} 1 & 1 & \dots & 1 \\ x_{11} & x_{21} & \dots & x_{n1} \\ x_{12} & x_{22} & \dots & x_{n2} \\ x_{13} & x_{23} & \dots & x_{n3} \\ 3 \cdot x_{1\,1}^{\;2} - |x_1|^2 & 3 \cdot x_{2\,1}^{\;2} - |x_2|^2 & \dots & 3 \cdot x_{n\,1}^{\;2} - |x_n|^2 \\ 3 \cdot x_{1\,2}^{\;2} - |x_1|^2 & 3 \cdot x_{2\,2}^{\;2} - |x_2|^2 & \dots & 3 \cdot x_{n\,2}^{\;2} - |x_n|^2 \\ 3 \cdot x_{1\,3}^{\;2} - |x_1|^2 & 3 \cdot x_{2\,3}^{\;2} - |x_2|^2 & \dots & 3 \cdot x_{n\,3}^{\;2} - |x_n|^2 \\ 3 \cdot x_{11} \cdot x_{12} & 3 \cdot x_{21} \cdot x_{22} & \dots & 3 \cdot x_{n1} \cdot x_{n2} \\ 3 \cdot x_{11} \cdot x_{13} & 3 \cdot x_{21} \cdot x_{23} & \dots & 3 \cdot x_{n1} \cdot x_{n3} \\ 3 \cdot x_{13} \cdot x_{12} & 3 \cdot x_{23} \cdot x_{22} & \dots & 3 \cdot x_{n3} \cdot x_{n2} \end{pmatrix}}_{=:\bar{X}} \cdot \underbrace{\begin{pmatrix} q_1 \\ q_2 \\ \\ \vdots \\ \\ \vdots \\ q_n \end{pmatrix}}_{=:\overrightarrow{q}} . \qquad (3.3.9)$$

Computing the $\overrightarrow{q}$ now means to minimize the functional

$$F(\overrightarrow{q}) = \| \bar{X} \cdot \overrightarrow{q} - \overrightarrow{t} \|_2^2 \to \min. \qquad (3.3.10)$$

# The Venant source model

Since the number of degrees of freedom $n$ is in general larger than the number of determined parameters on the left-hand side in (9), no unique solution exists. To select a solution with minimal energy, which is a physiologically plausible approach, we define a regularization matrix $\overline{W}$ by $(\overline{W})_{(m,s)} = (\|\Delta\overline{x}_m\|_2)^{r/2}\delta_{m,s}$ for $r = 1$ or $r = 2$ to solve (9). Now, the vector $q$ is the result of minimizing the functional

$$F_\lambda(q) = \|\overline{t} - \overline{X}q\|_2^2 + \lambda\|\overline{W}q\|_2^2 \qquad (10)$$

with $\overline{X}_j$ and $\overline{t}_j$ defined as in (9). The first term measures the difference between the original dipole moment and our approximation, whereas the second term penalizes loads of large absolute value $|q_i|$. Thereby, spatially high-frequent, unphysiological sources with large absolute values that do not contribute to the far-field, so-called blind sources, are avoided (Louis, 2013). Furthermore, this additional term ensures the uniqueness of the solution of minimizing $F_\lambda$.

[Vorwerk, Hanrath, Wolters & Grasedyck, *NeuroImage*, 2019]

# The Venant source model

Differentiation with respect to the $q_i$ yields the solution of the minimization problem:

$$\left(\overline{X}^T\overline{X} + \lambda\overline{W}^T\overline{W}\right)q = \overline{X}^T\overline{t}, \tag{11}$$

and as result for the vector $q$,

$$q = \left(\overline{X}^T\overline{X} + \lambda\overline{W}^T\overline{W}\right)^{-1} \cdot \overline{X}^T\overline{t}. \tag{12}$$

The choice $r = 2$ for the regularization matrix results in a spatial concentration of loads around the dipole node, since large products $\Delta\overline{\mathbf{x}}_i q_i$ are penalized. The parameter $\lambda$ should be chosen as small as possible in order to approximate the desired moments accurately, but large enough to avoid indetermination of the linear system.

# The Venant source model

[Wolters, *Lecture scriptum*]

In the direct Venant potential approach that uses the blurred dipole, the total potential $\Phi(\mathbf{x}) \approx \Phi_h(\mathbf{x}) = \sum_{j=1}^{N_h} \varphi_j(\mathbf{x}) \underline{u}_h^{[j]}$ is projected into the FE space and, using variational and FE techniques, the linear system

$$K_h \underline{u}_h = \underline{j}_{\text{Venant},h} \tag{6.126}$$

with the same stiffness matrix as in (6.111) is derived. The right-hand side vector $\underline{j}_{\text{Venant},h} \in \mathbb{R}^{N_h}$ has only $C$ non-zero entries at the neighboring FE nodes to the considered dipole location.

Right-hand side vector has only about 27 (for tetrahedra models) non-zero entries and can be computed similarly fast as PI.

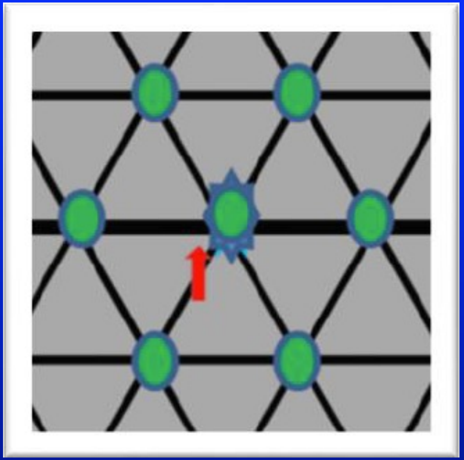

# Whitney source modeling approach

[Bauer, Pursiainen, Vorwerk, Köstler & Wolters, *IEEE TBME*, 2015]
[Pursiainen, Vorwerk & Wolters, *Phys Med Biol*, 2016]
[Miinalainen, Rezaei, Us, Nüßing, Engwer, Wolters & Pursiainen, *NeuroImage*, 2019]

# Whitney source model

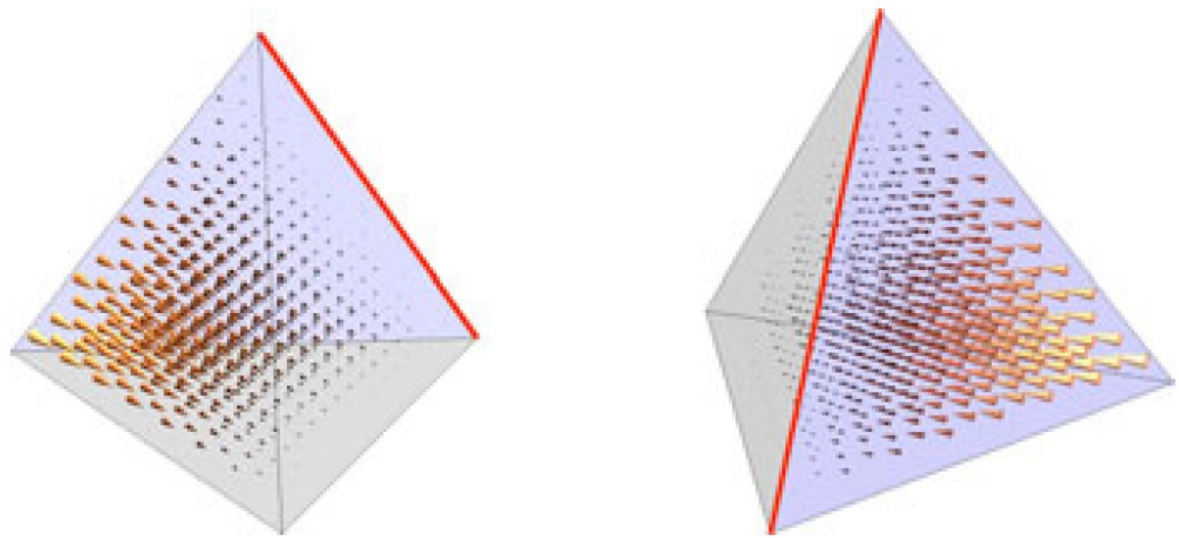

Fig. 6. Two views of a linear Nédélec's edge-based face function restricted to a single tetrahedron $T$. The face $F$ and edge $E \subset F$ determining the function have been visualized with light blue and red (bold line) color, respectively.

**One of the three edge based face functions of a Whitney source model**

[Bauer, Pursiainen, Vorwerk, Köstler & Wolters, *IEEE TBME*, 2015]
[Pursiainen, Vorwerk & Wolters, *Phys Med Biol*, 2016]
[Miinalainen, Rezaei, Us, Nüßing, Engwer, Wolters & Pursiainen, *NeuroImage*, 2019]

# Whitney source model

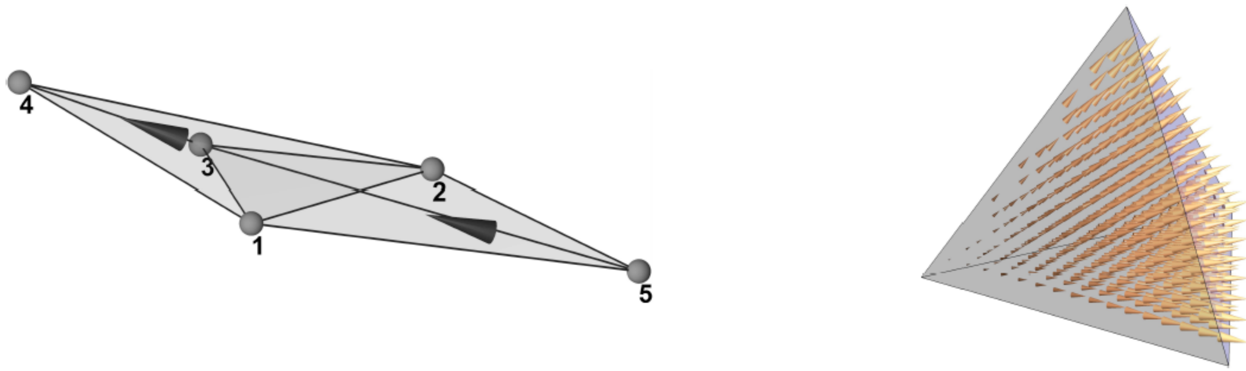


**Figure 3.** On the left: A lowest order Raviart-Thomas basis function is supported on two adjacent tetrahedral elements. On the right: The vector field of a Raviart-Thomas basis function restricted to one tetrahedral element.

**On the right: Whitney source built up of all three edge-based face functions (each weighted with 1/3)**

# Source model extent

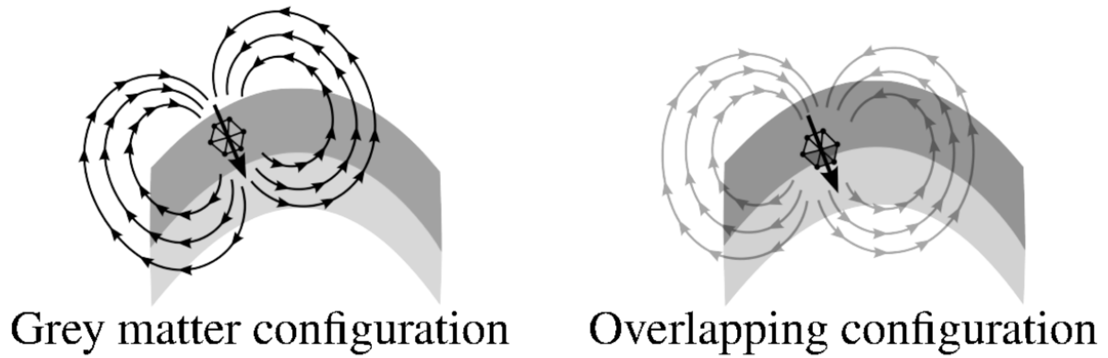


**Figure 1.** A schematic visualization of a situation in which a focal primary source current (large arrow) is approximated using a configuration of six finite element mesh nodes (point stencil). **Left:** If all the mesh nodes are contained in the compartment of the grey matter (grey layer), the correct volume current field resulting from this source might look like indicated by the dark field lines. **Right:** If one or more nodes in the configuration overlap with compartment (light grey layer) other than that of the grey matter, then the volume current and thereby also the electric potential obtained will differ from the actual distribution with regard to both topography (field lines) and magnitude (field line color) due to the conductivity jump between the compartments (Appendix). Consequently, the focality (compactness) of the source configuration is vital in order to avoid forward errors.

[Pursiainen, Vorwerk & Wolters, *Phys Med Biol*, 2016]

# Source model extent

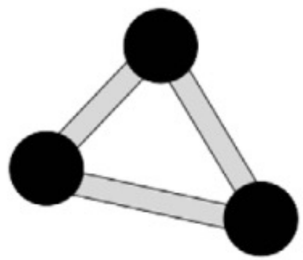

(E)

- A single element
- 4 FE mesh nodes
- 4 monopolar sources

**PI**

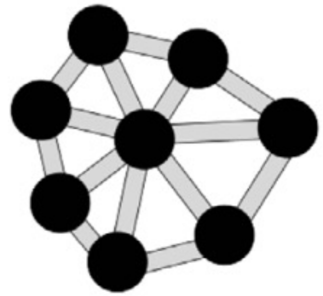

(F)

- Elements sharing a given node
- ≈16–27 FE mesh nodes
- ≈16–27 monopolar sources

**Venant**

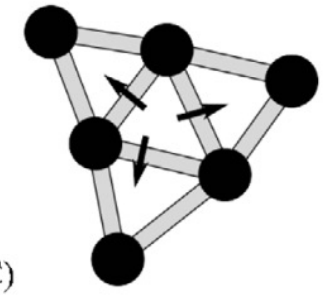

(C)

- Elements that share a face with a given element
- 8 FE mesh nodes
- 4 dipolar sources
- 4 FI sources (black)

**Whitney**

# Summary: FEM source models

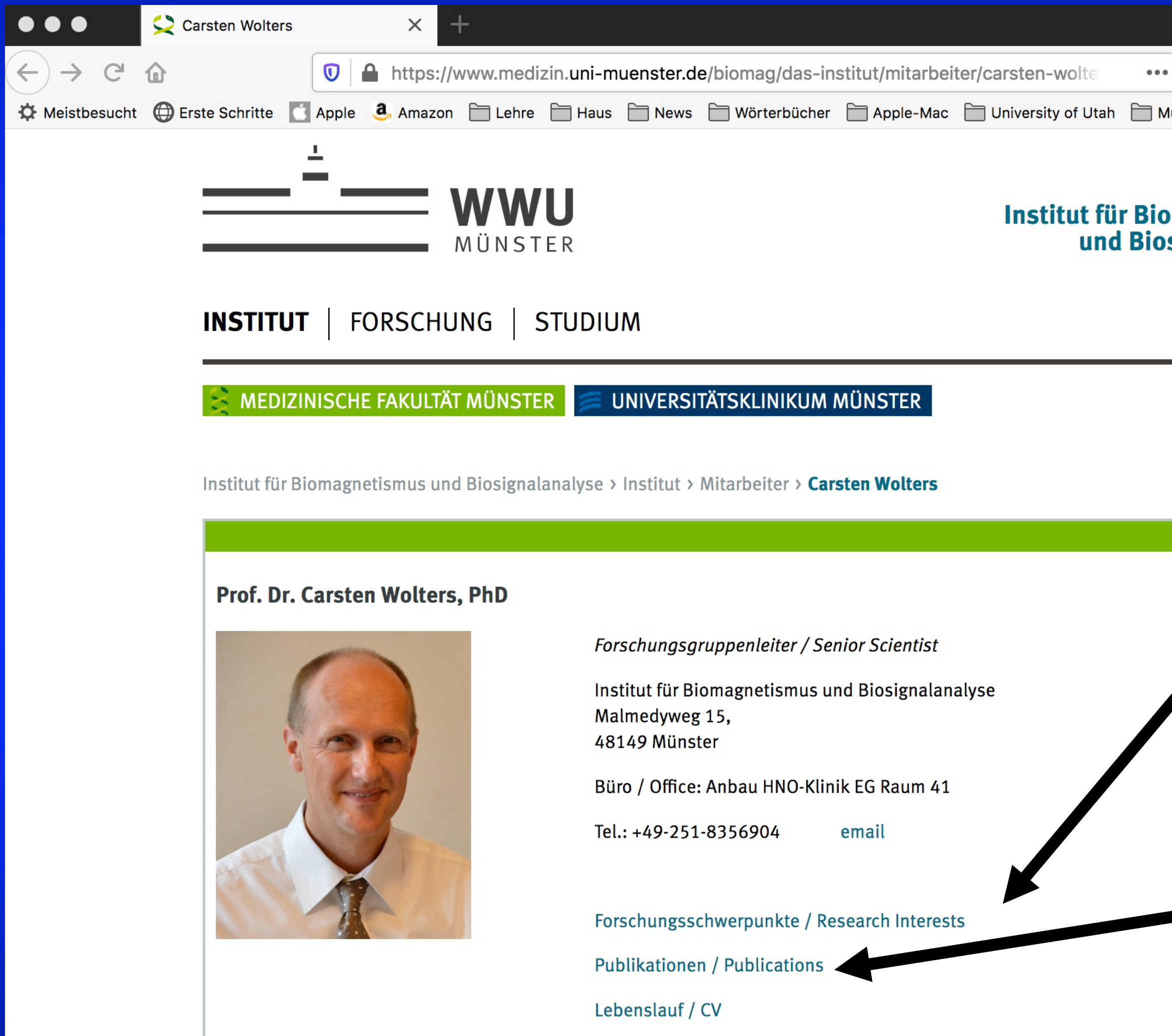


Links to all Bachelor/Master/PhD theses

All own publications

# Summary: FEM source models

- **For FEM based forward modeling, the following source models exist:**
  - **Subtraction source model (Höltershinken et al., SIAM SISC, 2024; Drechsler et al., NeuroImage, 2009; Wolters et al., SIAM SISC, 2007)**

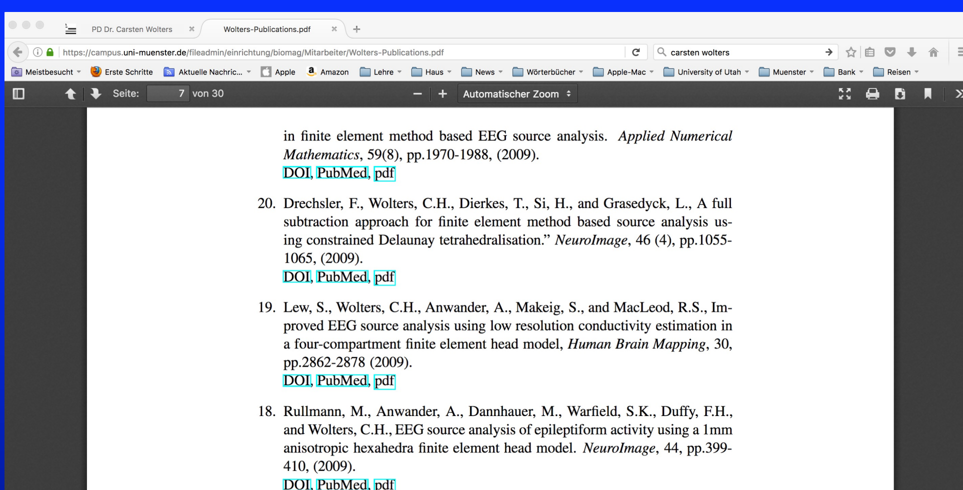

in finite element method based EEG source analysis. *Applied Numerical Mathematics*, 59(8), pp.1970-1988, (2009).
DOI, PubMed, pdf

20. Drechsler, F., Wolters, C.H., Dierkes, T., Si, H., and Grasedyck, L., A full subtraction approach for finite element method based source analysis using constrained Delaunay tetrahedralisation." *NeuroImage*, 46 (4), pp.1055-1065, (2009).
DOI, PubMed, pdf

19. Lew, S., Wolters, C.H., Anwander, A., Makeig, S., and MacLeod, R.S., Improved EEG source analysis using low resolution conductivity estimation in a four-compartment finite element head model, *Human Brain Mapping*, 30, pp.2862-2878 (2009).
DOI, PubMed, pdf

18. Rullmann, M., Anwander, A., Dannhauer, M., Warfield, S.K., Duffy, F.H., and Wolters, C.H., EEG source analysis of epileptiform activity using a 1mm anisotropic hexahedra finite element head model. *NeuroImage*, 44, pp.399-410, (2009).
DOI, PubMed, pdf

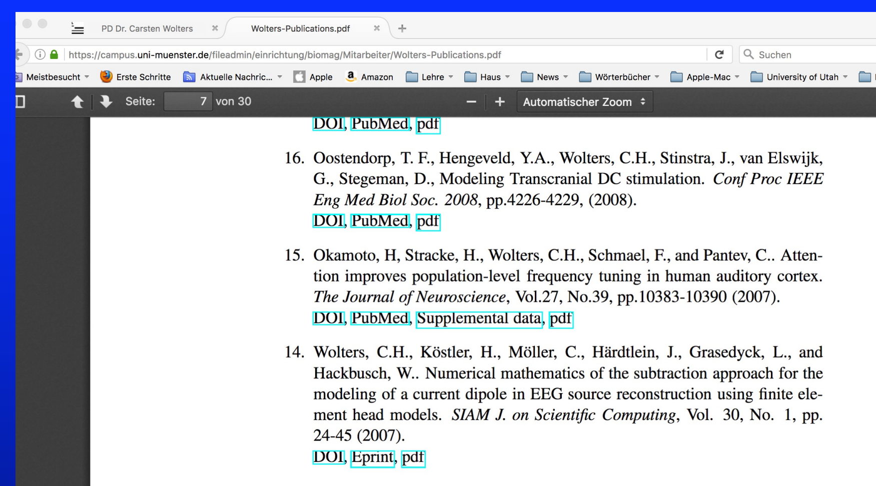

DOI, PubMed, pdf

16. Oostendorp, T. F., Hengeveld, Y.A., Wolters, C.H., Stinstra, J., van Elswijk, G., Stegeman, D., Modeling Transcranial DC stimulation. *Conf Proc IEEE Eng Med Biol Soc. 2008*, pp.4226-4229, (2008).
DOI, PubMed, pdf

15. Okamoto, H, Stracke, H., Wolters, C.H., Schmael, F., and Pantev, C.. Attention improves population-level frequency tuning in human auditory cortex. *The Journal of Neuroscience*, Vol.27, No.39, pp.10383-10390 (2007).
DOI, PubMed, Supplemental data, pdf

14. Wolters, C.H., Köstler, H., Möller, C., Härdtlein, J., Grasedyck, L., and Hackbusch, W.. Numerical mathematics of the subtraction approach for the modeling of a current dipole in EEG source reconstruction using finite element head models. *SIAM J. on Scientific Computing*, Vol. 30, No. 1, pp. 24-45 (2007).
DOI, Eprint, pdf

# Summary: FEM source models

- **For FEM based forward modeling, the following source models exist:**
  - **Subtraction source model**
  - **Partial integration (PI) source model (Wolters et al., ICS, 2007)**

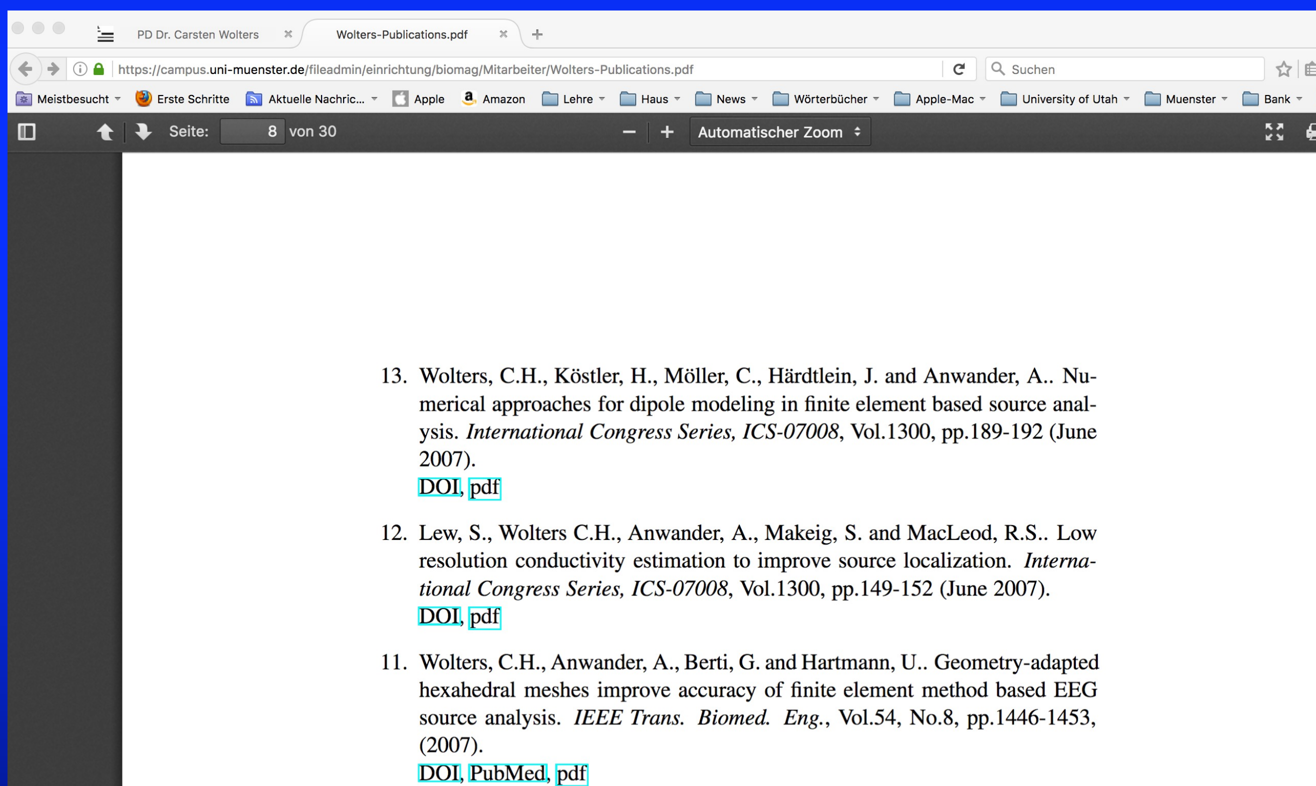


13. Wolters, C.H., Köstler, H., Möller, C., Härdtlein, J. and Anwander, A.. Numerical approaches for dipole modeling in finite element based source analysis. *International Congress Series, ICS-07008*, Vol.1300, pp.189-192 (June 2007).
DOI, pdf

12. Lew, S., Wolters C.H., Anwander, A., Makeig, S. and MacLeod, R.S.. Low resolution conductivity estimation to improve source localization. *International Congress Series, ICS-07008*, Vol.1300, pp.149-152 (June 2007).
DOI, pdf

11. Wolters, C.H., Anwander, A., Berti, G. and Hartmann, U.. Geometry-adapted hexahedral meshes improve accuracy of finite element method based EEG source analysis. *IEEE Trans. Biomed. Eng.*, Vol.54, No.8, pp.1446-1453, (2007).
DOI, PubMed, pdf

# Summary: FEM source models

- For FEM based forward modeling, the following source models exist:
  - Subtraction source model
  - Partial integration (PI) source model
  - Venant source model (Hanrath, 2019; Vorwerk et al., 2019)

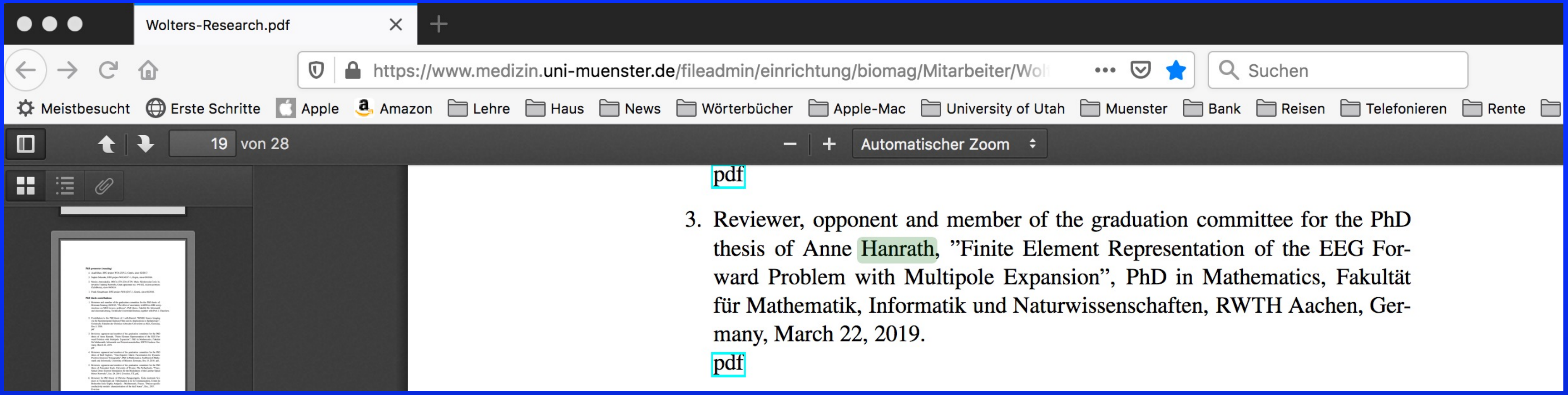

# Summary: FEM source models

- For FEM based forward modeling, the following source models exist:
  - Subtraction source model
  - Partial integration (PI) source model
  - Saint-Venant source model
  - Whitney source model (Bauer et al., 2015; Pursiainen et al., 2016; Miinalainen et al., 2019)

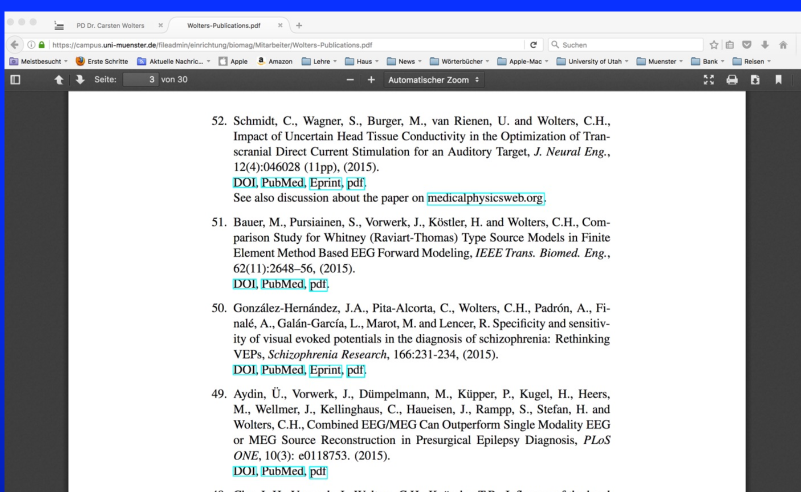

52. Schmidt, C., Wagner, S., Burger, M., van Rienen, U. and Wolters, C.H., Impact of Uncertain Head Tissue Conductivity in the Optimization of Transcranial Direct Current Stimulation for an Auditory Target, *J. Neural Eng.*, 12(4):046028 (11pp), (2015).
DOI, PubMed, Eprint, pdf.
See also discussion about the paper on medicalphysicsweb.org.

51. Bauer, M., Pursiainen, S., Vorwerk, J., Köstler, H. and Wolters, C.H., Comparison Study for Whitney (Raviart-Thomas) Type Source Models in Finite Element Method Based EEG Forward Modeling, *IEEE Trans. Biomed. Eng.*, 62(11):2648–56, (2015).
DOI, PubMed, pdf.

50. González-Hernández, J.A., Pita-Alcorta, C., Wolters, C.H., Padrón, A., Finalé, A., Galán-García, L., Marot, M. and Lencer, R. Specificity and sensitivity of visual evoked potentials in the diagnosis of schizophrenia: Rethinking VEPs, *Schizophrenia Research*, 166:231-234, (2015).
DOI, PubMed, Eprint, pdf.

49. Aydin, Ü., Vorwerk, J., Dümpelmann, M., Küpper, P., Kugel, H., Heers, M., Wellmer, J., Kellinghaus, C., Haueisen, J., Rampp, S., Stefan, H. and Wolters, C.H., Combined EEG/MEG Can Outperform Single Modality EEG or MEG Source Reconstruction in Presurgical Epilepsy Diagnosis, *PLoS ONE*, 10(3): e0118753. (2015).
DOI, PubMed, pdf

48. Cho, J.-H., Vorwerk, J., Wolters, C.H., Knösche, T.R., Influence of the head

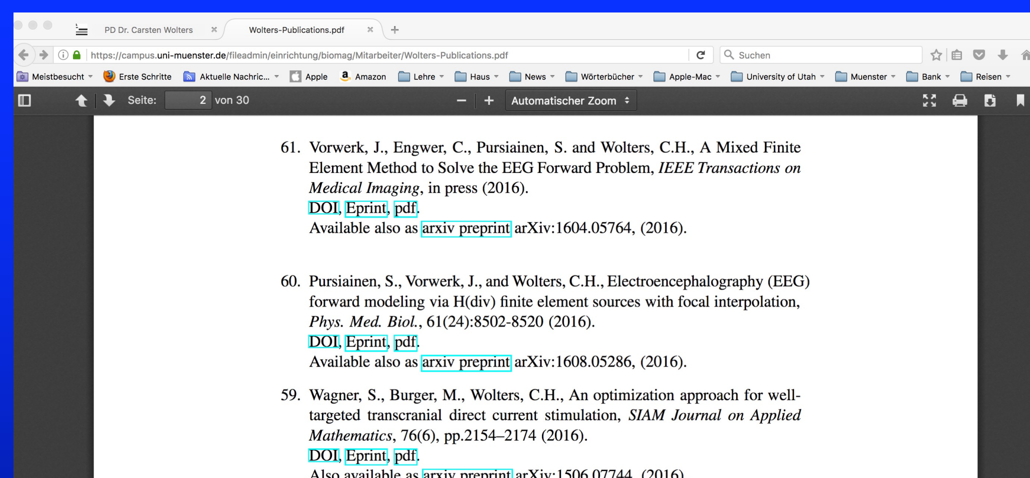

61. Vorwerk, J., Engwer, C., Pursiainen, S. and Wolters, C.H., A Mixed Finite Element Method to Solve the EEG Forward Problem, *IEEE Transactions on Medical Imaging*, in press (2016).
DOI, Eprint, pdf.
Available also as arxiv preprint arXiv:1604.05764, (2016).

60. Pursiainen, S., Vorwerk, J., and Wolters, C.H., Electroencephalography (EEG) forward modeling via H(div) finite element sources with focal interpolation, *Phys. Med. Biol.*, 61(24):8502-8520 (2016).
DOI, Eprint, pdf.
Available also as arxiv preprint arXiv:1608.05286, (2016).

59. Wagner, S., Burger, M., Wolters, C.H., An optimization approach for well-targeted transcranial direct current stimulation, *SIAM Journal on Applied Mathematics*, 76(6), pp.2154–2174 (2016).
DOI, Eprint, pdf.
Also available as arxiv preprint arXiv:1506.07744, (2016).

# Structure of the lecture

- Convergence analysis for FEM subtraction approach (sections 6.5.1-6.5.3 of lecture scriptum)
- Other source models (section 6.5.4 of lecture scriptum)
- Overview: Multi-layer sphere model (section 6.2 of lecture scriptum)
- Forward modeling results

[de Munck and Peters, *IEEE TBME*, 1993]
[Wolters, *Lecture scriptum*]

# The multi-layer sphere model

## 6.2 Analytical solutions in multi-layer sphere models

### 6.2.1 The potential in a multilayer sphere model

De Munck [68] and de Munck and Peters [73] derived series expansion formulas for the direct problem (6.1) with boundary condition (6.2) and reference potential (6.3) for a mathematical dipole (6.4) in a multilayer sphere model as shown in Figure 6.2. A rough overview of the formulas will be given now. Refer to the original literature for a more detailed derivation.

$$\nabla \cdot (\sigma \nabla \Phi) = \nabla \cdot \mathrm{j}^p = \mathrm{J}^p \quad \text{in } \Omega, \tag{6.1}$$

$$\langle \sigma \nabla \Phi, \mathrm{n} \rangle |_{\Gamma} = 0, \tag{6.2}$$

$$\Phi(x_{\mathrm{ref}}) = 0\,. \tag{6.3}$$

$$\mathrm{J}^p(x) = \nabla \cdot \mathrm{j}^p(x) := \nabla \cdot \mathrm{M}\delta(x - x_0)\,. \tag{6.4}$$

# The multi-layer sphere model

[de Munck and Peters, *IEEE TBME*, 1993]
[Wolters, *Lecture scriptum*]

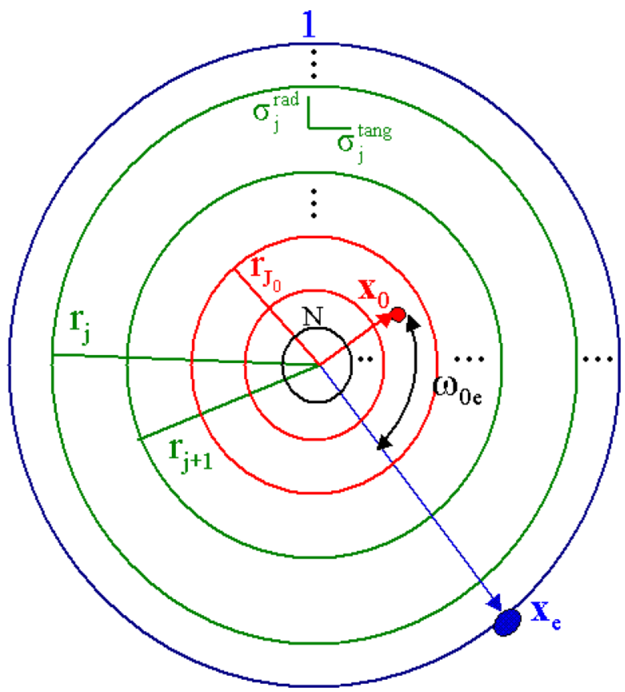


Figure 6.2: *The multilayer sphere model.*

As shown in Figure 6.2, the model consists of shells $N$ up to 1 with radii $r_N < r_{N-1} < \ldots < r_1$ and constant radial, $\sigma^{rad}(r) = \sigma_j^{rad} \in \mathbb{R}^+$, and tangential conductivity, $\sigma^{tang}(r) = \sigma_j^{tang} \in \mathbb{R}^+$, within each layer $r_{j+1} < r < r_j$. It is assumed in the following, that the source at position $\mathbf{x}_0$ with radial coordinate $r_0 \in \mathbb{R}$ is in a more interior layer than the measurement electrode at position $\mathbf{x}_e \in \mathbb{R}^3$ on the outer surface with radial coordinate $r_e = r_1 \in \mathbb{R}$ and $r_0 < r_{J_0} \leq r_e$.

# The multi-layer sphere model

[de Munck and Peters, *IEEE TBME*, 1993]
[Wolters, *Lecture scriptum*]

### 6.2.2 Series expansion formulas for a monopole source

The potential for a monopole source, $\mathrm{J}^p(\mathbf{x}) = \delta(\mathbf{x} - \mathbf{x}_0)$, can be expressed by the spherical harmonics expansion

$$4\pi \mathrm{u}_{\mathrm{mon}} = \sum_{n=0}^{\infty} (2n+1) R_n(r_0, r_e) P_n(\cos \omega_{0e}) \tag{6.42}$$

with $\omega_{0e}$ the angular distance between source and electrode as shown in Figure 6.2, $P_n$ the Legendre polynomials [394] and $R_n$ the solution of the inhomogeneous differential equation

$$\frac{\partial}{\partial r}\left(r^2 \sigma^{\mathrm{rad}}(r) \frac{\partial}{\partial r} R_n(r_0, r)\right) - n(n+1)\sigma^{\mathrm{tang}}(r) R_n(r_0, r) = \delta(r_0 - r). \tag{6.43}$$

As will be shown now, the solution of the above equation, i.e., the coefficients $R_n$, can be computed analytically and the series (6.42) converges.

# The multi-layer sphere model

[de Munck and Peters, *IEEE TBME*, 1993]
[Wolters, *Lecture scriptum*]

$$R_n(r_0,r_e) = \frac{\left\{ M_{J_0}(r_0, r_{J_0+1}) \prod_{j=N}^{J_0-1} M_j(r_j,r_{j+1}) \right\}_{12}}{\left\{ -r_e^2 \prod_{j=N}^{1} M_j(r_j,r_{j+1}) \right\}_{22}} \zeta_0^{\nu_{J_0}} \prod_{j=1}^{J_0-1} \zeta_j^{\nu_j}. \qquad (6.44)$$

In this formula, it is $\zeta_0 = r_0/r_{J_0} < 1$ and $\zeta_j = r_{j+1}/r_j < 1$, and, with

$$S_j^-(r_j,r_{j+1}) = \begin{pmatrix} \frac{r_j \nu_j}{r_{j+1}} & -\frac{r_j}{\sigma_j^{\text{rad}}} \\ \frac{-\sigma_j^{\text{rad}} \nu_j(\nu_j+1)}{r_{j+1}} & \nu_j+1 \end{pmatrix}, \quad S_j^+(r_j,r_{j+1}) = \begin{pmatrix} \nu_j+1 & \frac{r_{j+1}}{\sigma_j^{\text{rad}}} \\ \frac{\nu_j(\nu_j+1)\sigma_j^{\text{rad}}}{r_j} & \frac{r_{j+1}\nu_j}{r_j} \end{pmatrix},$$

the matrices $M_j$ are defined as

$$M_j(r_j,r_{j+1}) = \zeta_j^{2\nu_j+2} \frac{1}{2\nu_j+1} S_j^-(r_j,r_{j+1}) + \frac{1}{2\nu_j+1} S_j^+(r_j,r_{j+1}). \qquad (6.45)$$

$$\nu_j(n) = \frac{1}{2}\left(-1+\sqrt{1+4n(n+1)\sigma_j^{\text{tang}}/\sigma_j^{\text{rad}}}\right)$$

# The multi-layer sphere model

[de Munck and Peters, *IEEE TBME*, 1993]
[Wolters, *Lecture scriptum*]

### 6.2.3 Series expansion formulas for a dipole source

The spherical harmonics expansion for the mathematical dipole (6.4) was expressed in terms of the gradient of the monopole potential (6.42) with respect to the source point $\mathbf{x}_0$ [68; 73],

$$\mathrm{u}(\mathbf{x}_0, \mathbf{x}_e) = (\mathbf{M}, \mathrm{grad}_0\, \mathrm{u}_{\mathrm{mon}}(\mathbf{x}_0, \mathbf{x}_e)).$$

With the help of

$$\mathrm{grad}_0\, r_0 = \frac{\mathbf{x}_0}{r_0} = \hat{\mathbf{x}}_0 \qquad \mathrm{grad}_0 \cos\omega_{0e} = \mathrm{grad}_0 \frac{(\mathbf{x}_0, \mathbf{x}_e)}{r_0 r_e} = \frac{1}{r_0}(\hat{\mathbf{x}}_e - \cos\omega_{0e}\hat{\mathbf{x}}_0),$$

a simple substitution yields the dipole potential

$$4\pi \mathrm{u}(\mathbf{x}_0, \mathbf{x}_e) = (\mathbf{M}, S_0\hat{\mathbf{x}}_e + (S_1 - \cos\omega_{0e} S_0)\hat{\mathbf{x}}_0)$$

with

$$S_0 = \frac{1}{r_0}\sum_{n=1}^{\infty}(2n+1)R_n(r_0, r_e)P_n'(\cos\omega_{0e}) \qquad (6.47)$$

and

$$S_1 = \sum_{n=1}^{\infty}(2n+1)R_n'(r_0, r_e)P_n(\cos\omega_{0e}). \qquad (6.48)$$

# The multi-layer sphere model

[de Munck and Peters, *IEEE TBME*, 1993]
[Wolters, *Lecture scriptum*]

The derivative of the Legendre polynomial can be computed by means of the recursion

$$P_n'(\cos\omega) \equiv \frac{d}{d\cos\omega} P_n(\cos\omega) = nP_{n-1}(\cos\omega) + \cos\omega P_{n-1}'(\cos\omega).$$

The computation of $R_n'(r_0, r_e)$ can again be performed analytically.

# The multi-layer sphere model

[de Munck and Peters, *IEEE TBME*, 1993]
[Wolters, *Lecture scriptum*]

A low convergence speed of the series (6.47) and (6.48) is found if the source approaches the electrode . Therefore, an asymptotic approximation was proposed [73], yielding the series of differences

$$S_0 = \frac{F_0}{r_0}\frac{\Lambda}{R^3} + \frac{1}{r_0}\sum_{n=1}^{\infty}\{(2n+1)R_n(r_0,r_e) - F_0\Lambda^n\}P_n'(\cos\omega_{0e}) \qquad (6.49)$$

and

$$S_1 = F_1\frac{\Lambda\cos\omega_{0e} - \Lambda^2}{R^3} + \sum_{n=1}^{\infty}\{(2n+1)R_n'(r_0,r_e) - F_1 n\Lambda^n\}P_n(\cos\omega_{0e}) \qquad (6.50)$$

with a higher speed of convergence [1]. Refer to the further derivations below and the original literature for the definition of $F_0$, $F_1$, $\Lambda$ and $R$ (all those terms are independent of $n$ and can be computed from the given radii and conductivities of layers between source and electrode and of the radial coordinate of the source) and for a derivation of the above series of differences. The computation of the series (6.49) and (6.50) are stopped after the k's term, if the following criterion is fulfilled

$$\frac{t_k}{t_0} \leq \upsilon, \qquad t_k := (2k+1)R_k' - F_1 k\Lambda^k. \qquad (6.51)$$

In the following simulations, a value of $10^{-6}$ is chosen for $\upsilon$ in (6.51). Using the asymptotic expansion (see below), no more than 30 terms are needed for the series computation at each electrode.

# Structure of the lecture

- Convergence analysis for FEM subtraction approach (sections 6.5.1-6.5.3 of lecture scriptum)
- Other source models (section 6.5.4 of lecture scriptum)
- Overview: Multi-layer sphere model (section 6.2 of lecture scriptum)
- Forward modeling results
- The local subtraction approach

[Li et al., *NeuroImage*, 2014]

# Cortical thickness in infants

- The cortical thickness in infants is smaller than in adults
- Important for our developments in EU-project www.childbrain.eu (2015-2019)

[Li et al., *NeuroImage*, 2014]

# Development of cortical thickness

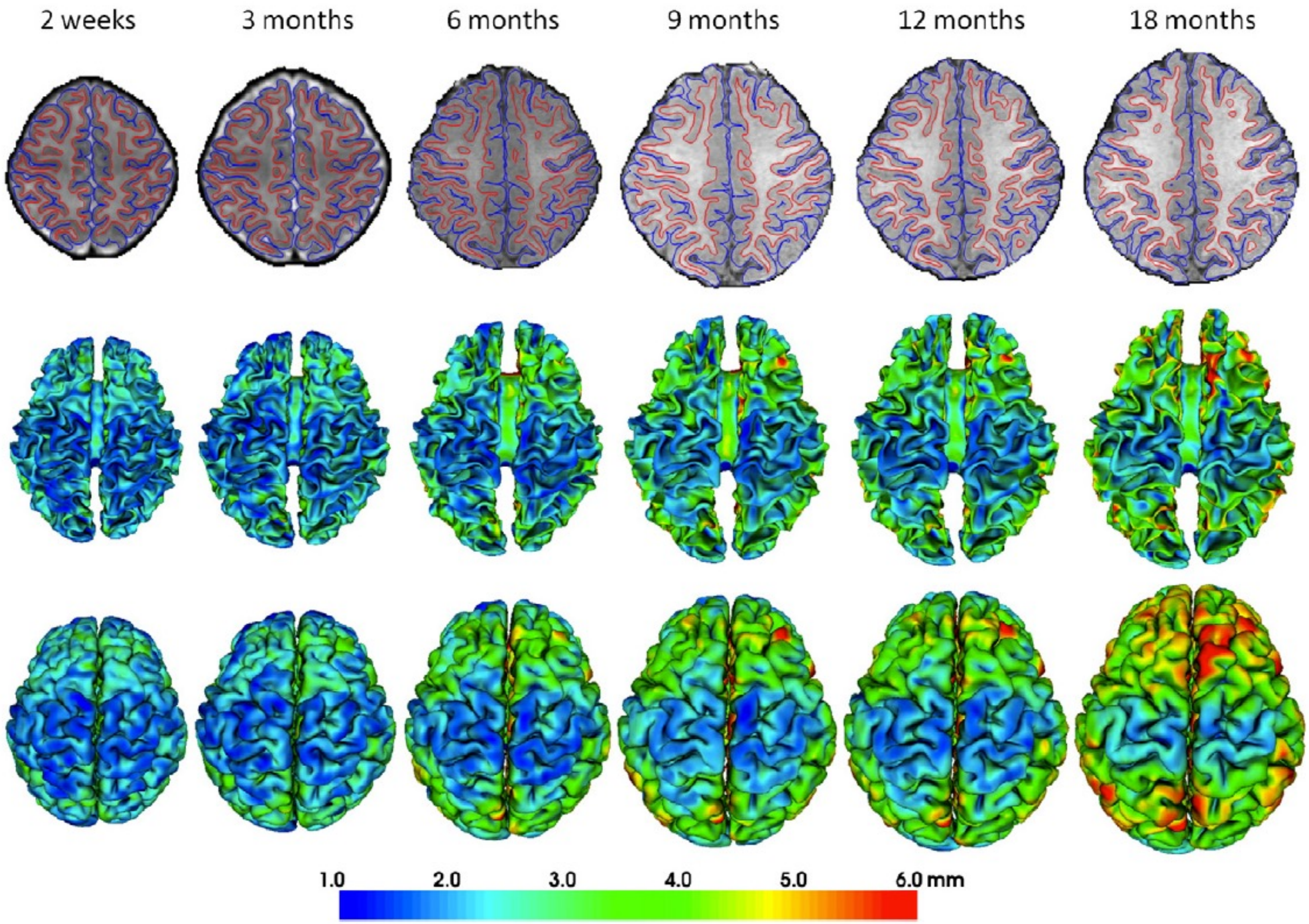


**Fig. 2.** Reconstructed longitudinal inner and outer cortical surfaces of a representative infant from 2 weeks to 18 months of age by the proposed method. The first row shows the longitudinal inner (red curves) and outer (blue curves) cortical surfaces embedded in their respective image spaces. The second and third rows show the longitudinal inner and outer surfaces, respectively, color-coded by the cortical thickness.

# Development of cortical thickness

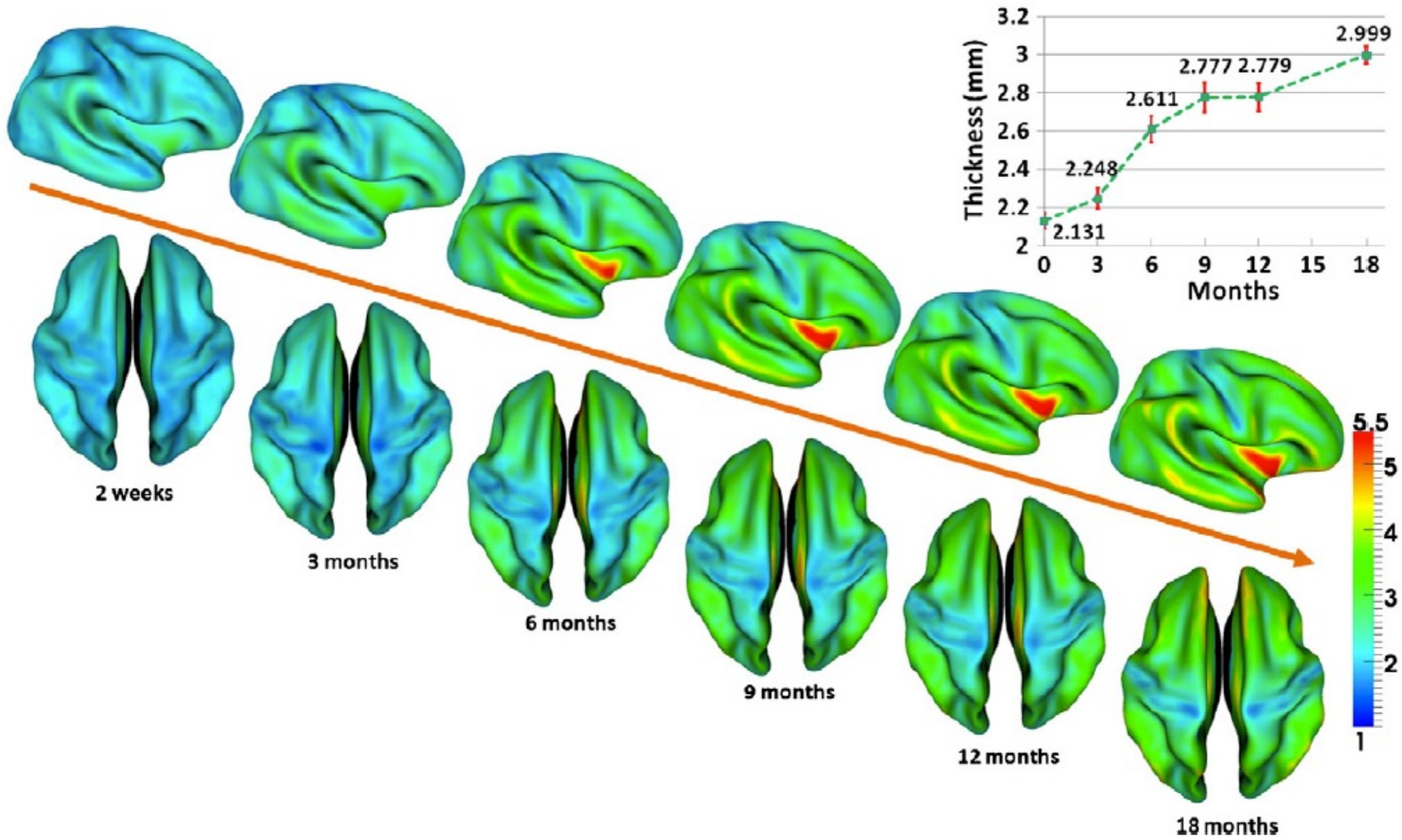


**Fig. 13.** Vertex-wise mapping of the average developmental trajectory of the cortical thickness (mm) of 13 infants from 2 weeks to 18 months of age, obtained using our proposed method. Also, the mean value and standard deviation of cortical thickness at each age, obtained from 13 infants, are shown in the top-right panel.

[Li et al., *NeuroImage*, 2014]

# Development of cortical thickness

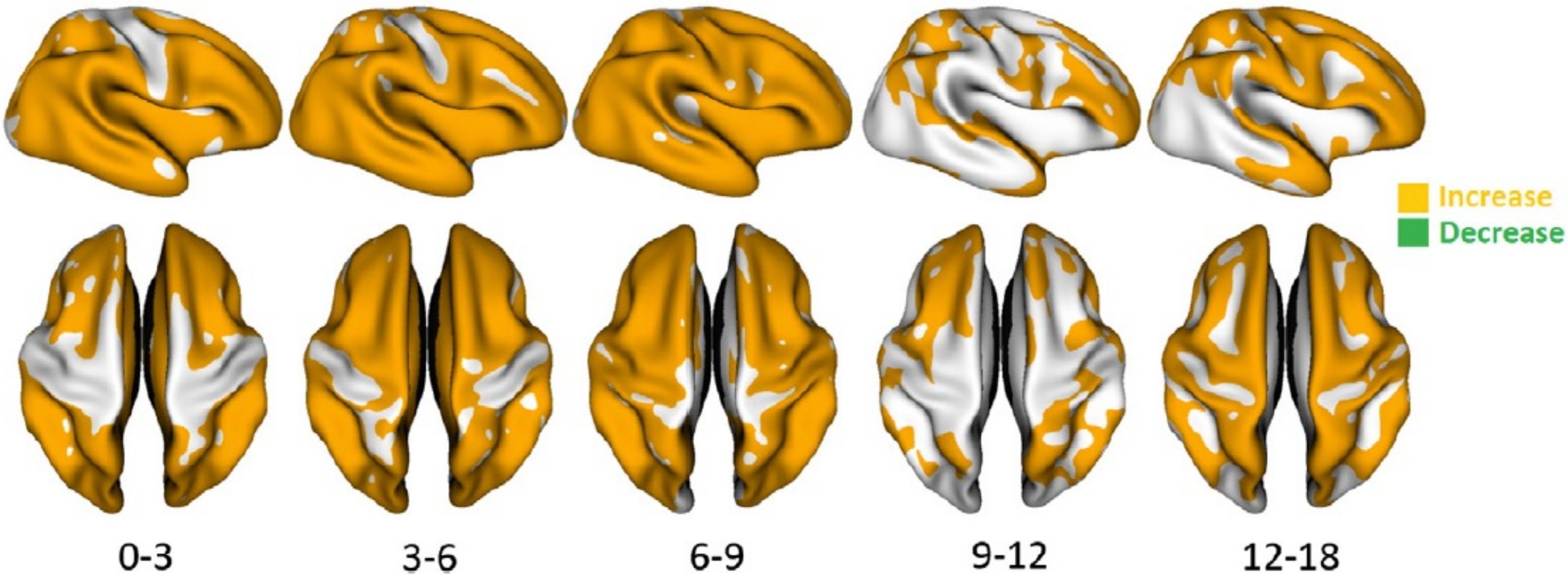


**Fig. 14.** Regions with statistically-significant cortical-thickness increase between each pair of successive time points of 13 infants from 2 weeks to 18 months of age, using TFCE ($p < 0.05$). No region showed the statistically significant decrease of cortical thickness during the first 18 months of life.

# Cortical thickness in infants

- If cortical thickness is smaller than in adults, it might also be smaller relative to the resolution of MRI and resulting FEM volume conductor models
- Therefore, appropriate FEM source models are needed especially for infants
- Distance of the sources to the next conductivity jump at the interface brain/CSF might go down to less than 2 mm, possibly even only 1 mm
- However, highly eccentric sources are known to cause modeling errors

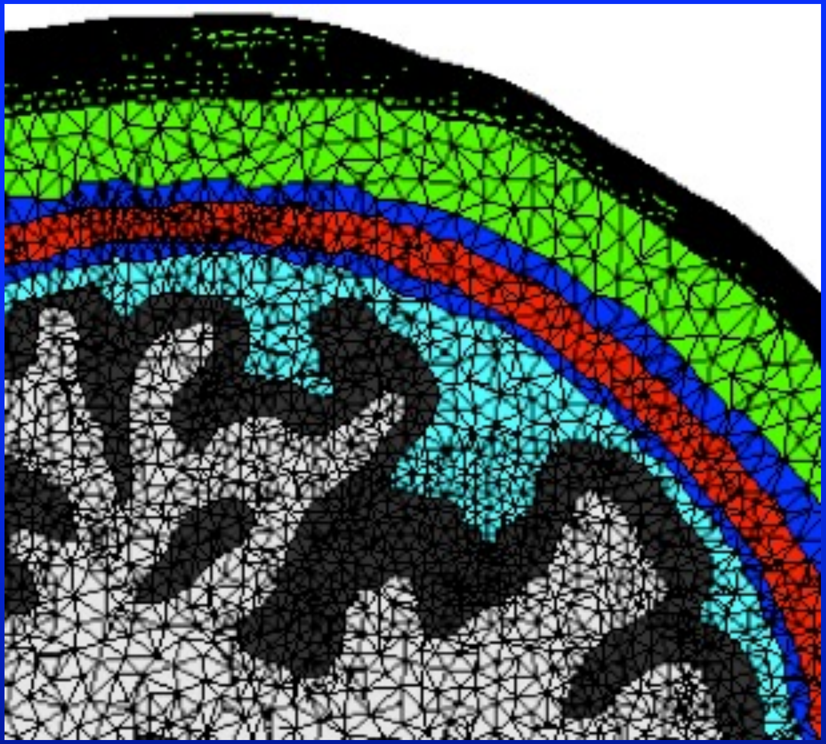

# PI, Venant, full subtraction and projected (or approx.) subtraction source models

[Drechsler, Wolters, Dierkes & Grasedyck, *NeuroImage*, 2009]
[Wolters, *Lecture scriptum*, 2016]

# Model and sensors

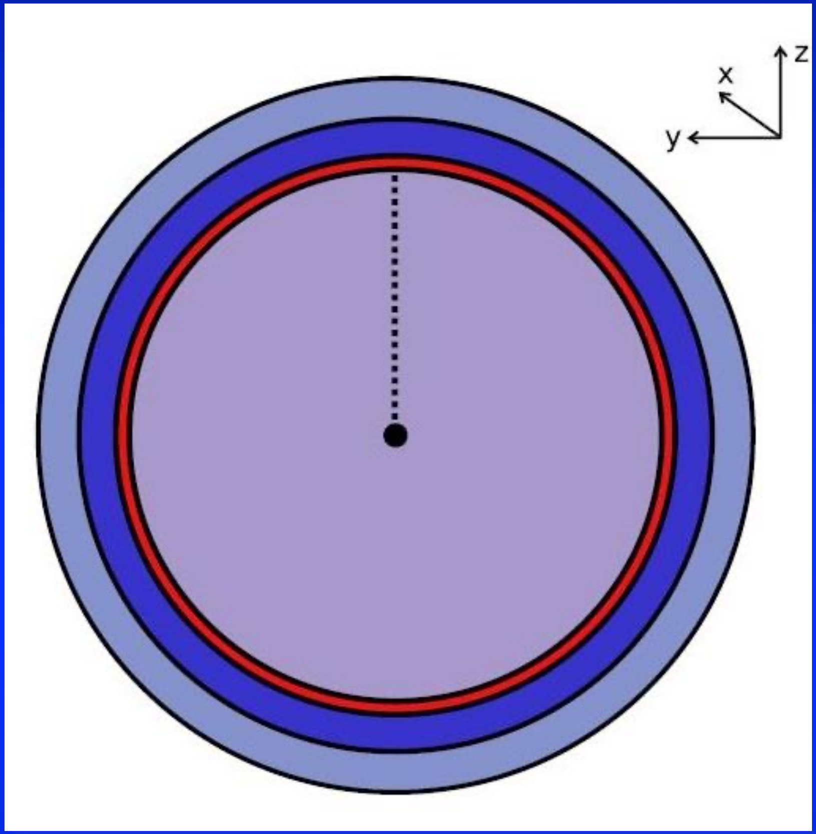


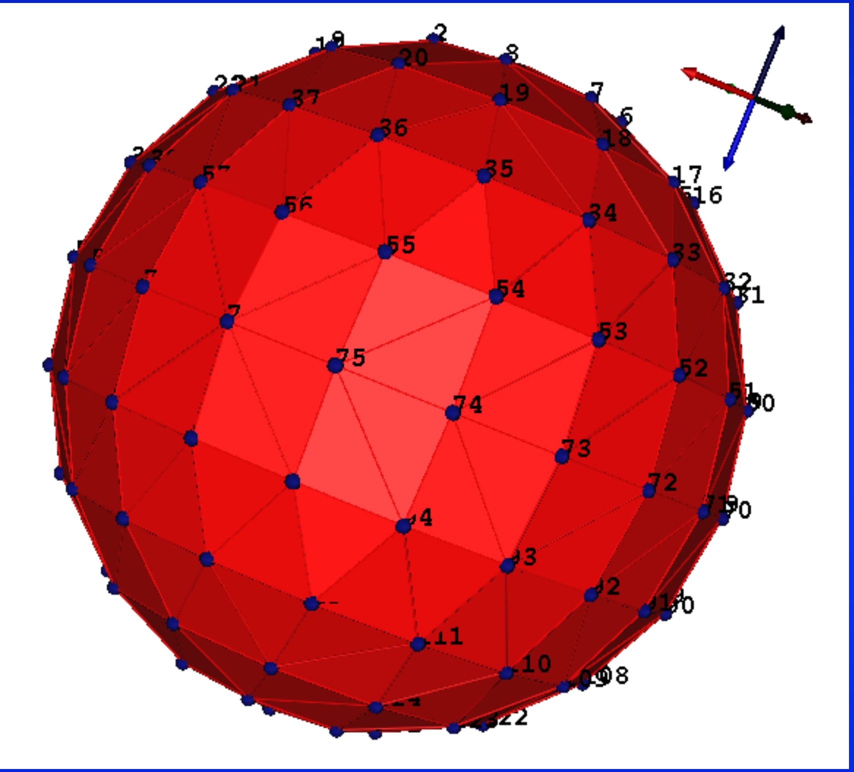

**<u>4-layer sphere model:</u>**
**Radii: 92, 86, 80, 78mm;**
**Cond.: 0.33, 0.0042:0.042, 1.79, 0.33 S/m**
**<u>Sources:</u>**
**Depth of 1mm below CSF up to midpoint**

**<u>748 regularly distributed electrodes:</u>**
**On a sphere with radius: 92mm**
**Needle electrode (“point in space”)**

[Meijs, Peters, Boom & Lopes da Silva, *Med.& Biol. Eng.&Comput.*, 1988]
[Meijs, Weier, Peters & van Oosterom, *IEEE Trans. Biomed. Eng.*, 1989]

# Validation: Error measures

**Relative error**

$$RE = \frac{||\Phi^{num} - \Phi^{ana}||_2}{||\Phi^{ana}||_2}$$

**Topography error**

$$RDM = \sqrt{\sum_{i=1}^{S} \left( \frac{\Phi_i^{num}}{||\Phi^{num}||_2} - \frac{\Phi_i^{ana}}{||\Phi^{ana}||_2} \right)^2}$$

**Magnitude error**

$$MAG = \frac{||\Phi^{num}||_2}{||\Phi^{ana}||_2}$$

[Drechsler, Wolters, Dierkes & Grasedyck, *NeuroImage*, 2009]
[Wolters, *Lecture scriptum*, 2016]

# "Optimal" FE mesh for the subtraction approach

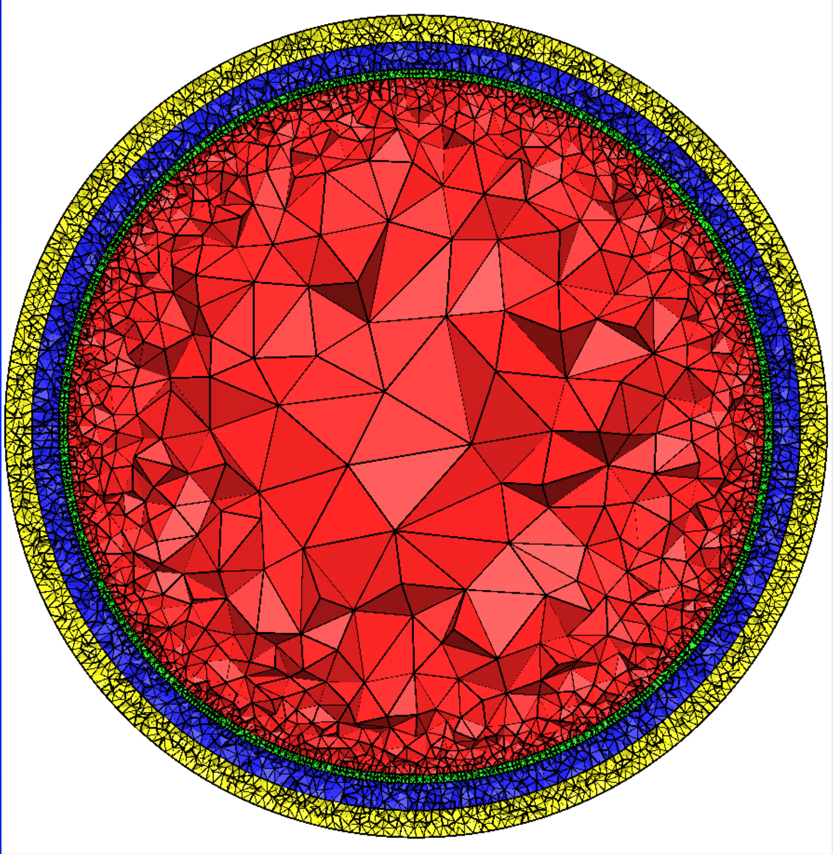

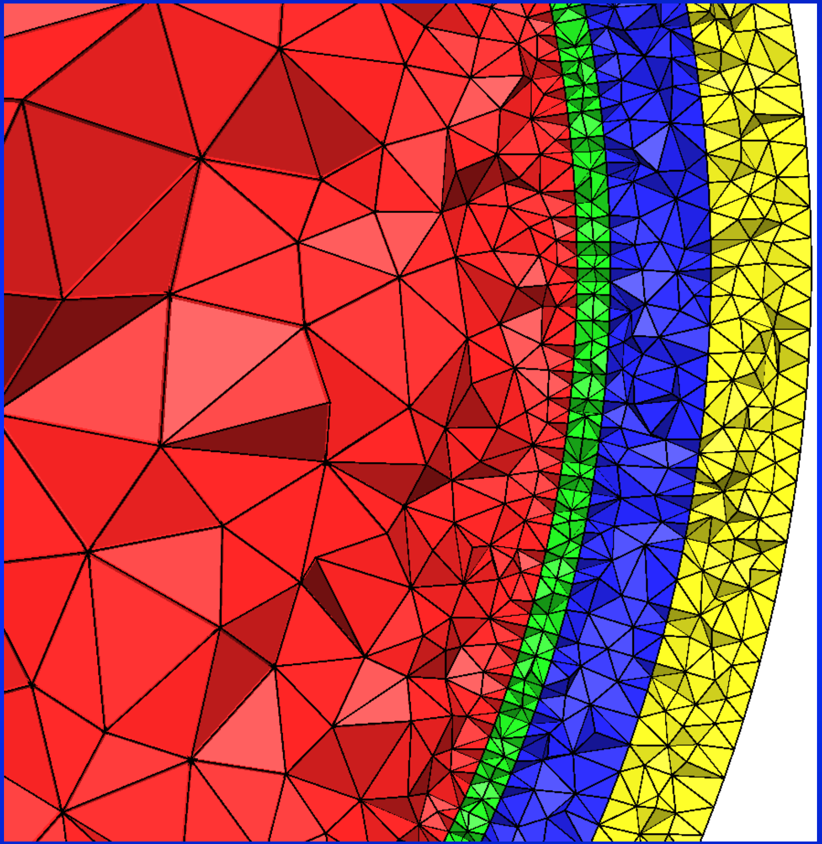

**Tetrahedra mesh: Coarse in brain, fine in CSF/skull/skin compartment:**
**Nodes: 360,056**
**Elements: 2,165,281**

[Drechsler, Wolters, Dierkes & Grasedyck, *NeuroImage*, 2009]
[Wolters, *Lecture scriptum*, 2016]

# Quadrature order for full subtraction approach

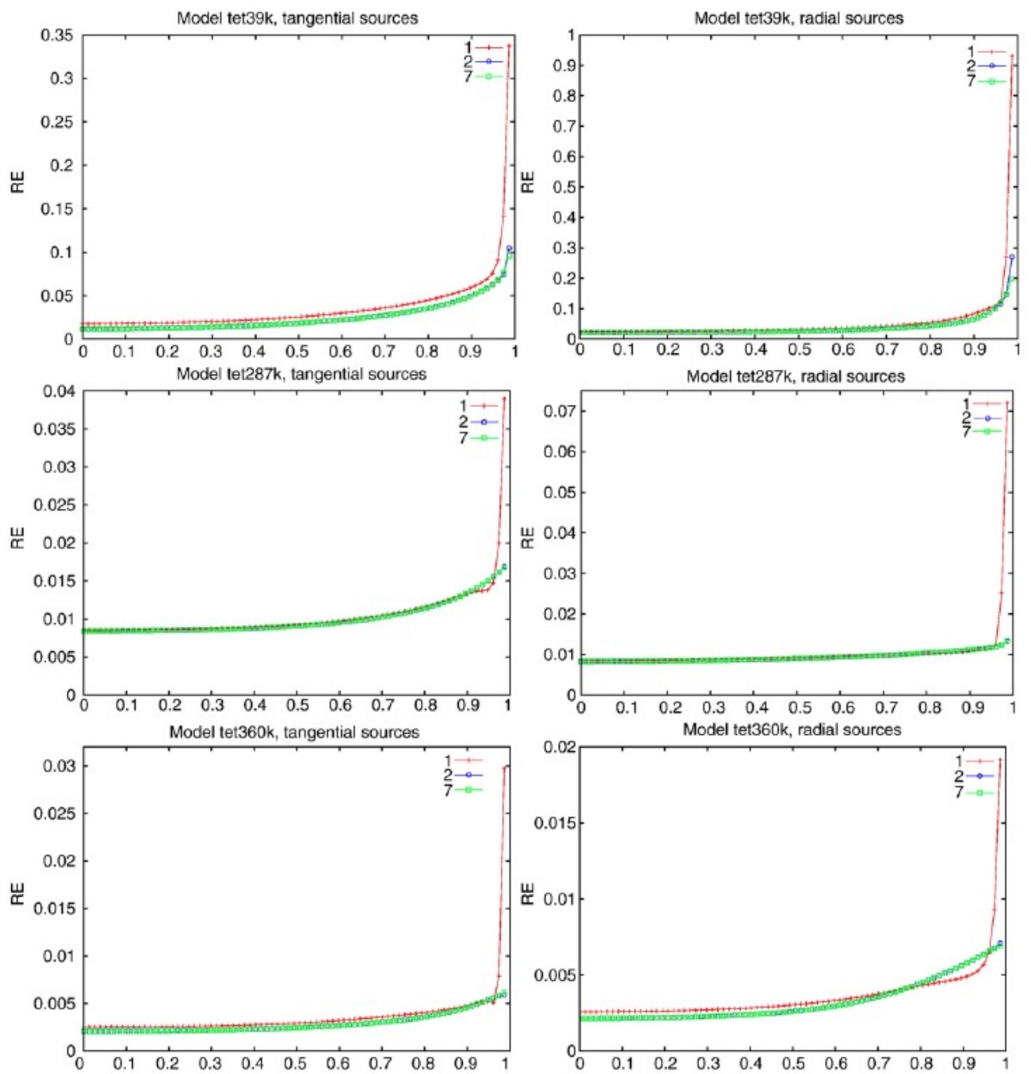


**Fig. 2.** Relative error for tangentially (left) and radially (right) oriented dipoles with quadrature orders of 1, 2 and 7: Model tet39k (top row), tet287k (middle row) and tet360k (bottom row). Note the different scaling for the RE.

[Drechsler, Wolters, Dierkes & Grasedyck, *NeuroImage*, 2009]
[Wolters, *Lecture scriptum*, 2016]

# Convergence behavior of full subtraction

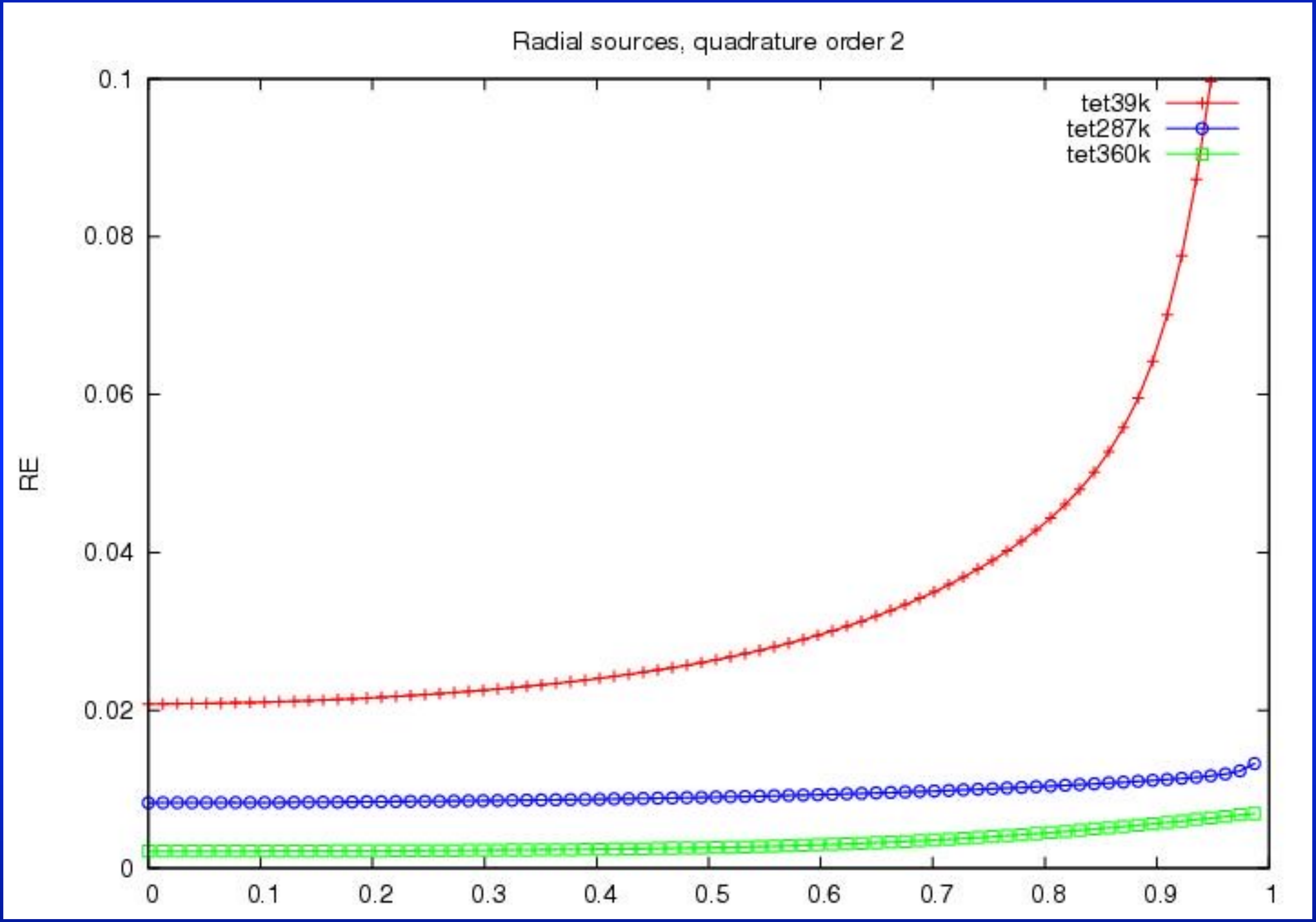

# RDM and MAG of full subtraction approach

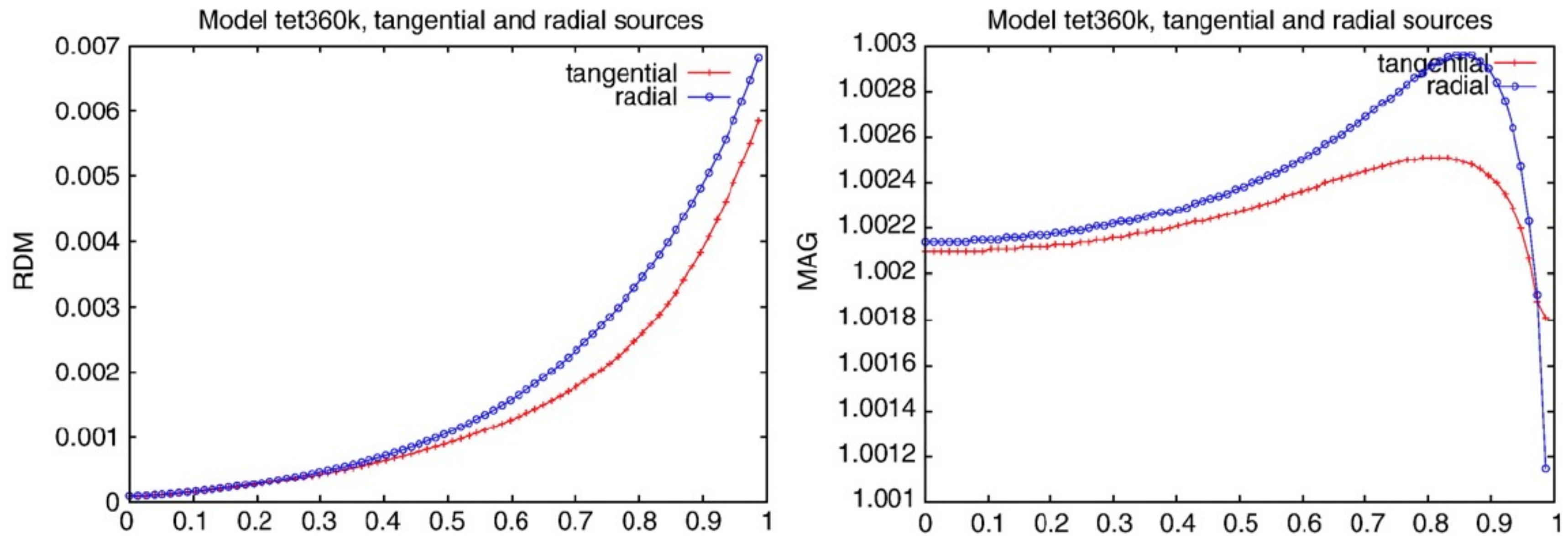


**Fig. 4.** RDM (left) and MAG errors (right) for model tet360k for tangentially and radially oriented dipoles.

[Drechsler, Wolters, Dierkes & Grasedyck, *NeuroImage*, 2009]
[Wolters, *Lecture scriptum*, 2016]

# Full against projected subtraction approach

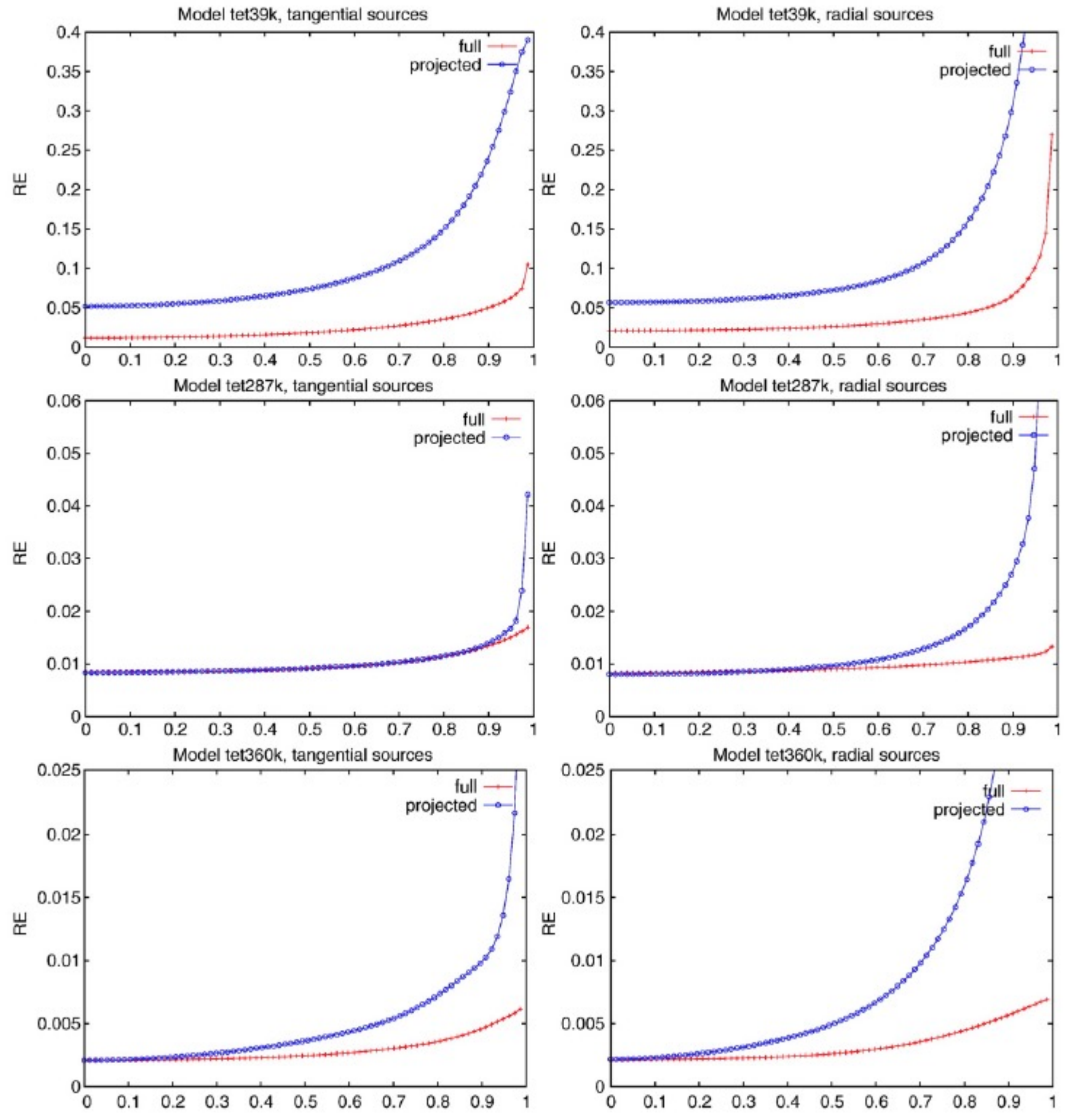


**Fig. 5.** Comparison between the presented full subtraction approach and the projected subtraction approach from Wolters et al. (2007a) with regard to the relative error for tangential (left) and radial sources (right): Model tet39k (top row), tet287k (middle row) and tet360K (bottom row).

[Drechsler, Wolters, Dierkes & Grasedyck, *NeuroImage*, 2009]
[Wolters, *Lecture scriptum*, 2016]

# "Optimal" FE mesh for the subtraction approach

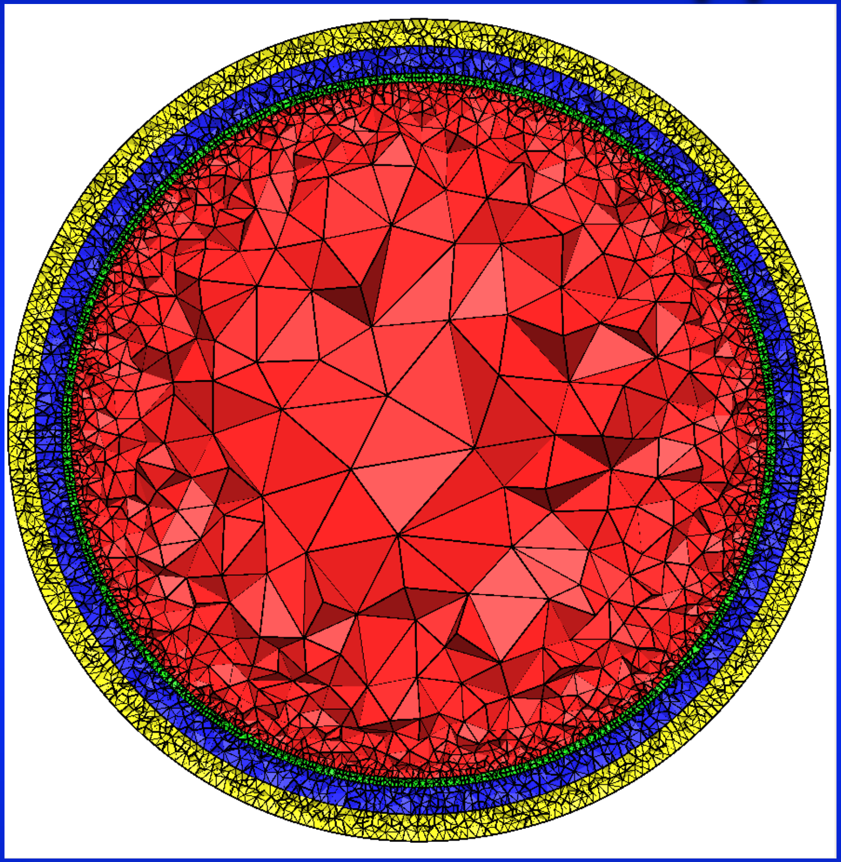

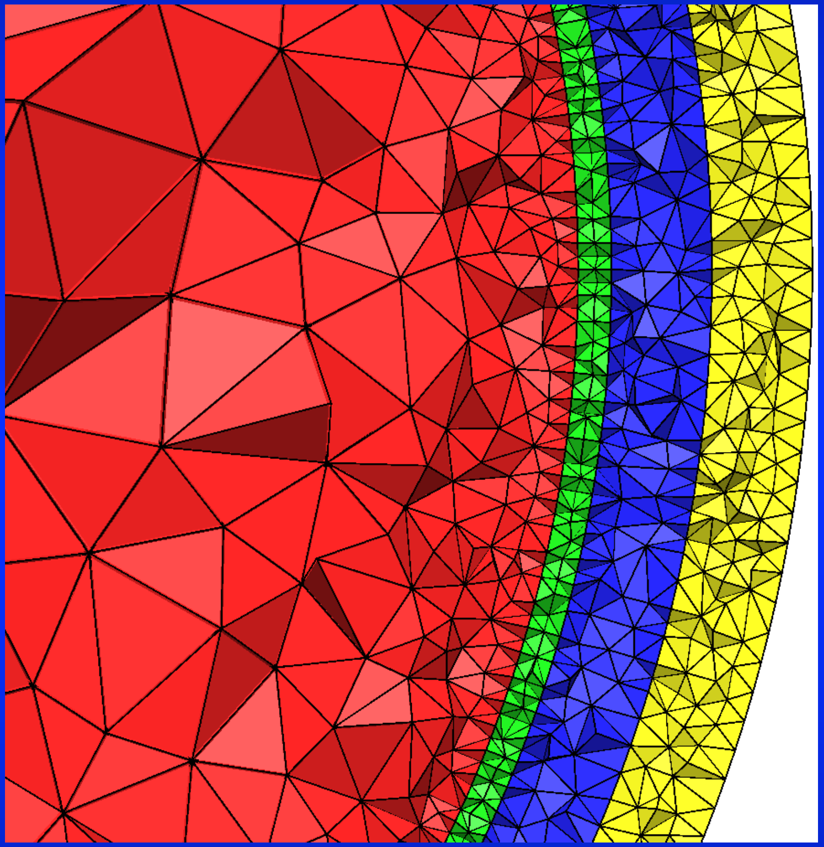

**Tetrahedra mesh: Coarse in brain, fine in CSF/skull/skin compartment:**
**Nodes: 360,056**
**Elements: 2,165,281**

# "Optimal" FE mesh for the subtraction approach

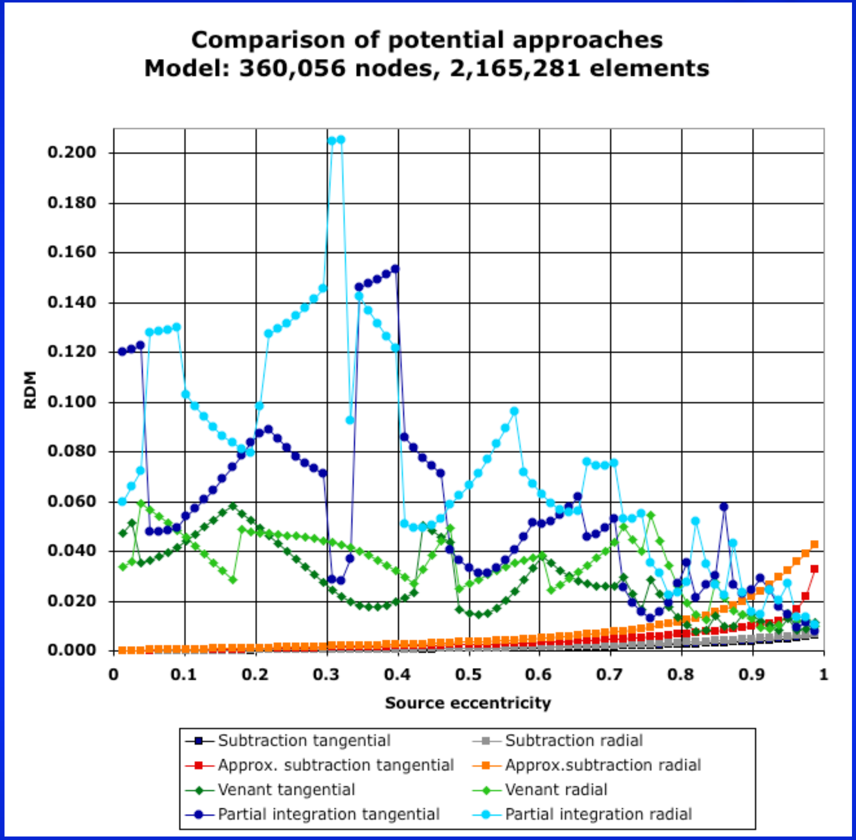


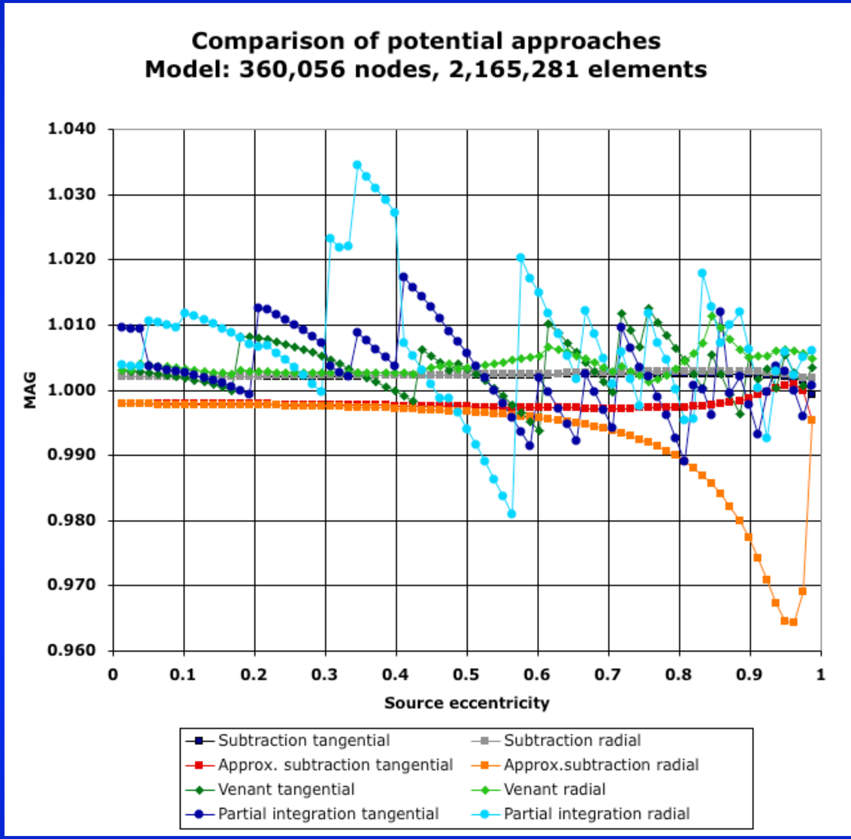


**TETGEN tetrahedra mesh, coarse in brain, fine in CSF/skull/skin compartment:**
**Nodes: 360,056**
**Elements: 2,165,281**

# Dipole fit localization error

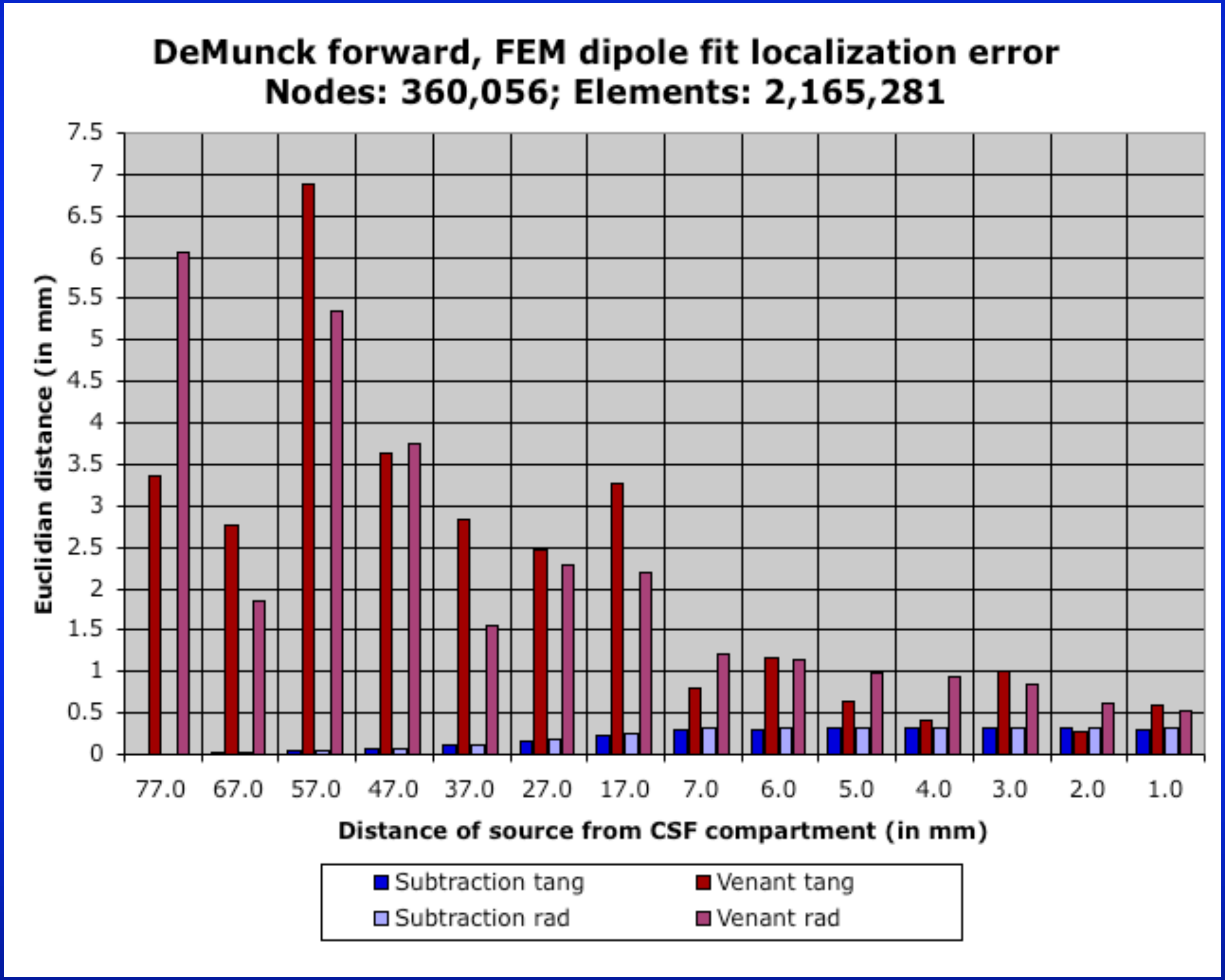

# "Optimal" FE mesh for the direct potential approaches

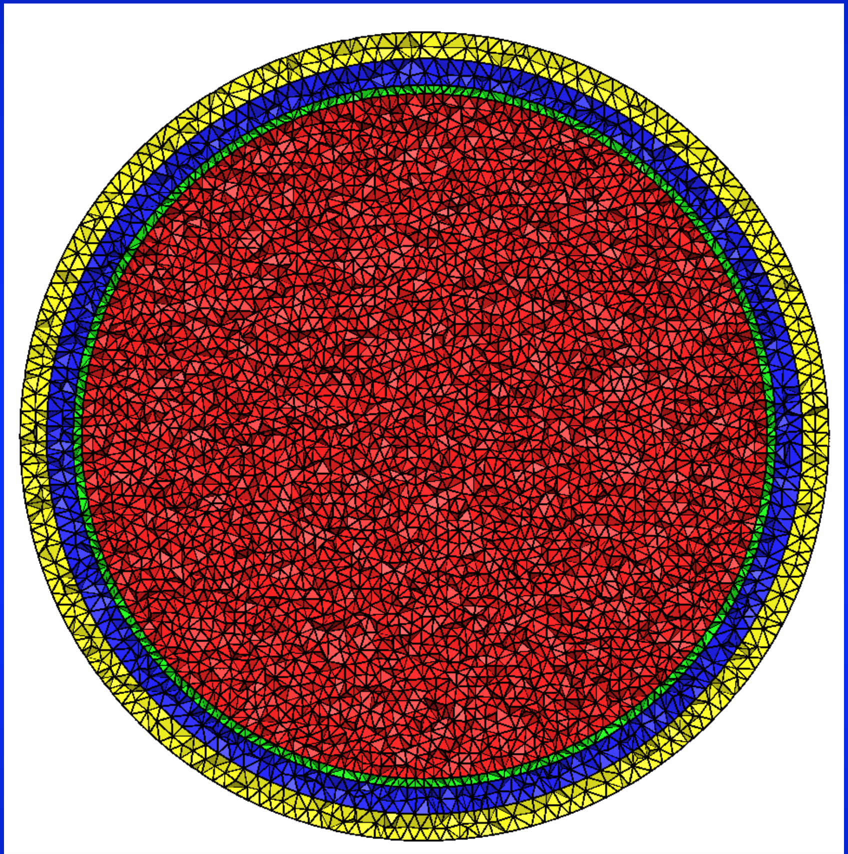

**Tetrahedra mesh, regularly refined in all 4 compartments:**
**Nodes: 161,086**
**Elements: 987,582**

# “Optimal” FE mesh for the direct potential approaches

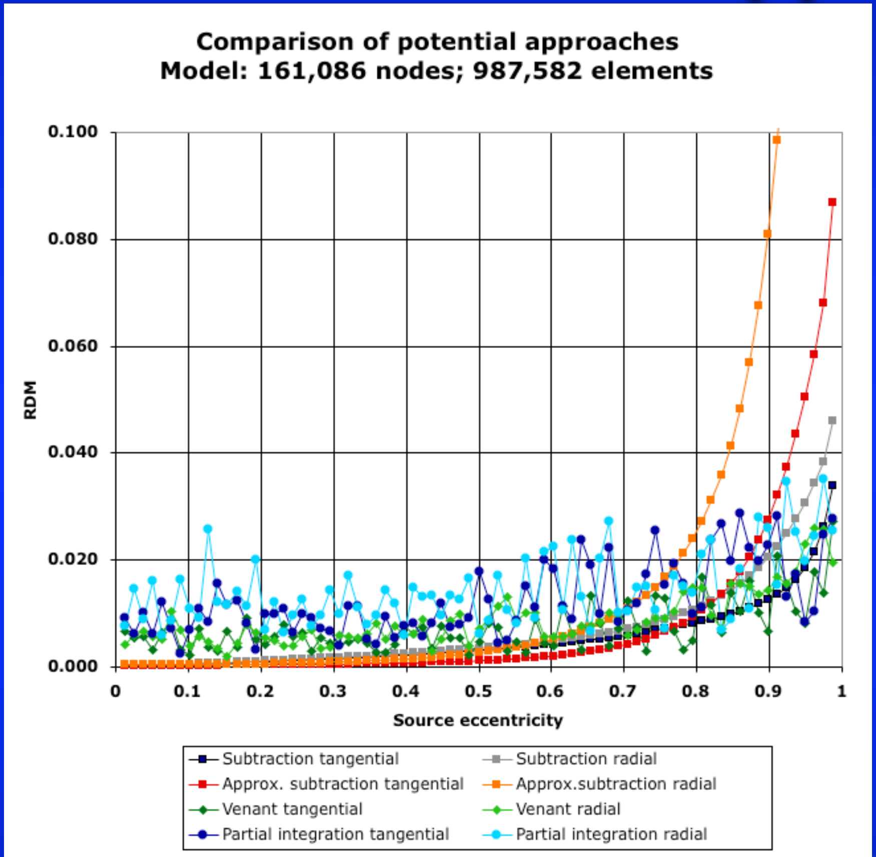


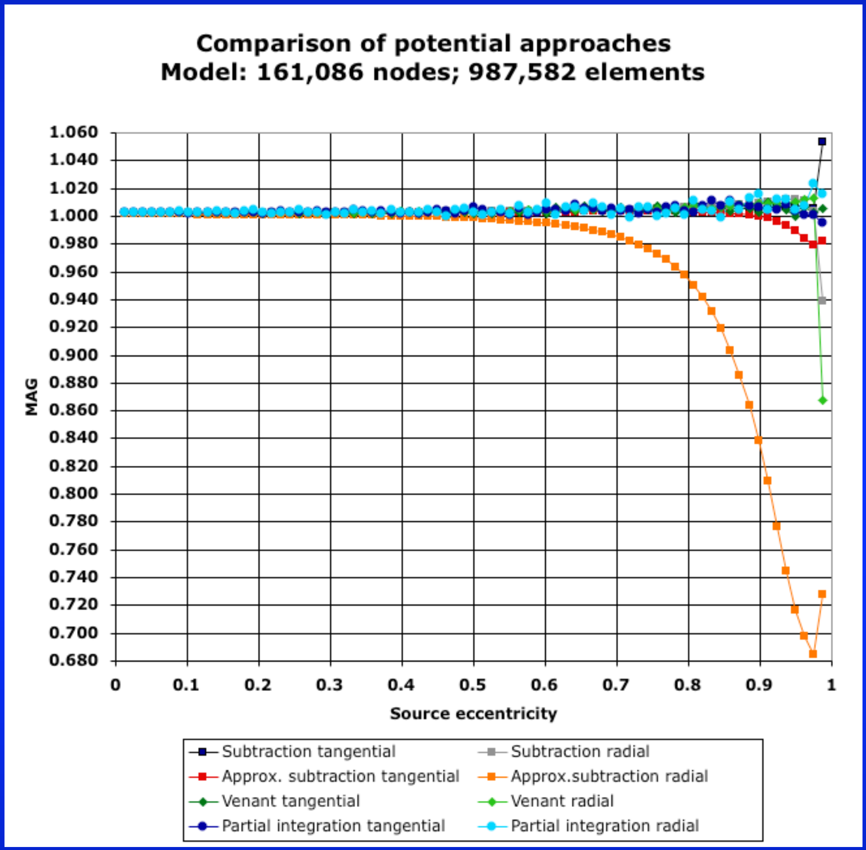


**TETGEN tetrahedra mesh, volume constraint of 5 in all 4 compartments:**
**Nodes: 161,086**
**Elements: 987,582**

# Dipole fit localization error

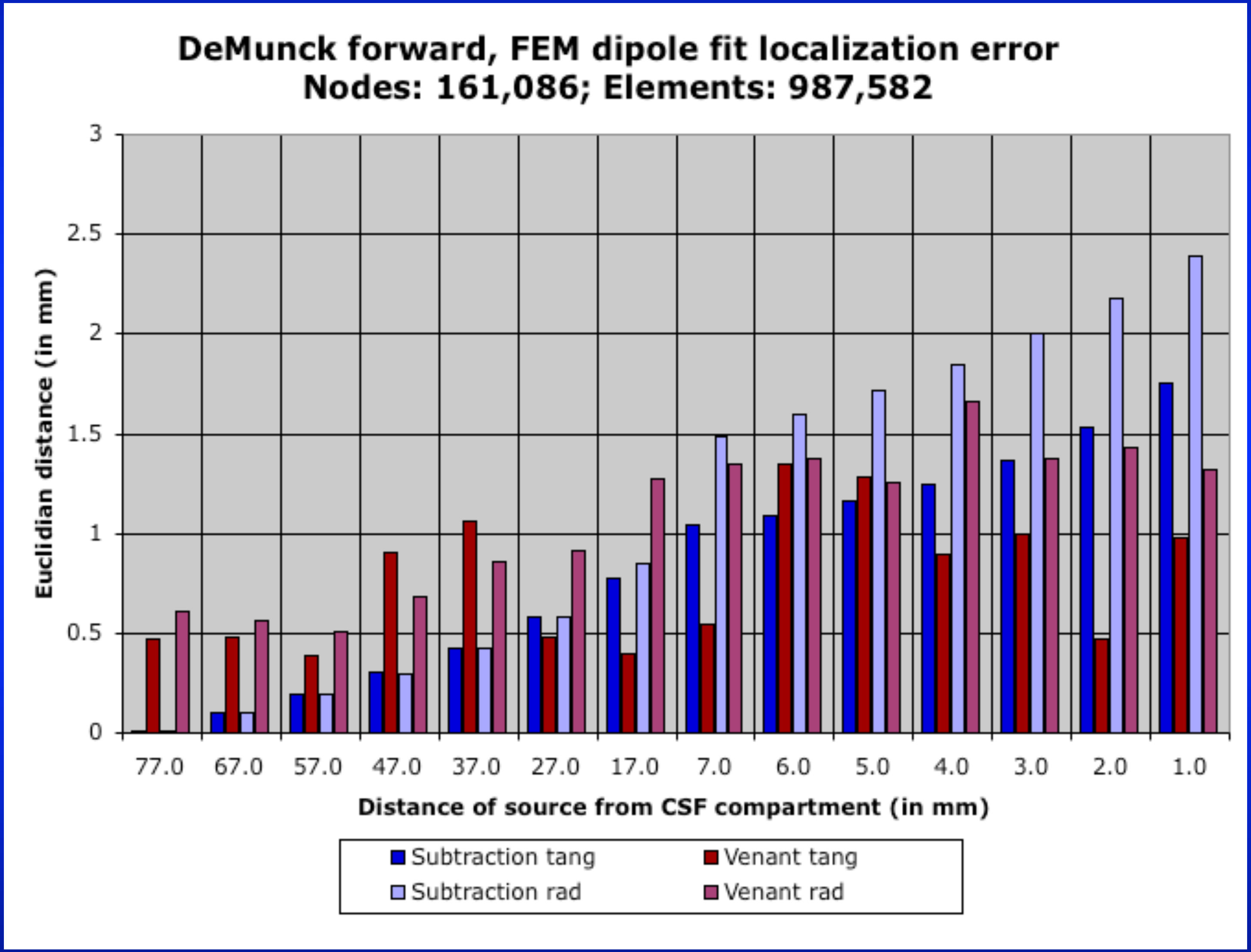

# Higher degree FEM basis functions for full subtraction source model

[Florian Grüne, Master thesis Mathematics, *University of Münster,* 2014]

# Reminder: Link for literature to own work:

**https://campus.uni-muenster.de/biomag/das-institut/mitarbeiter/carsten-wolters/**

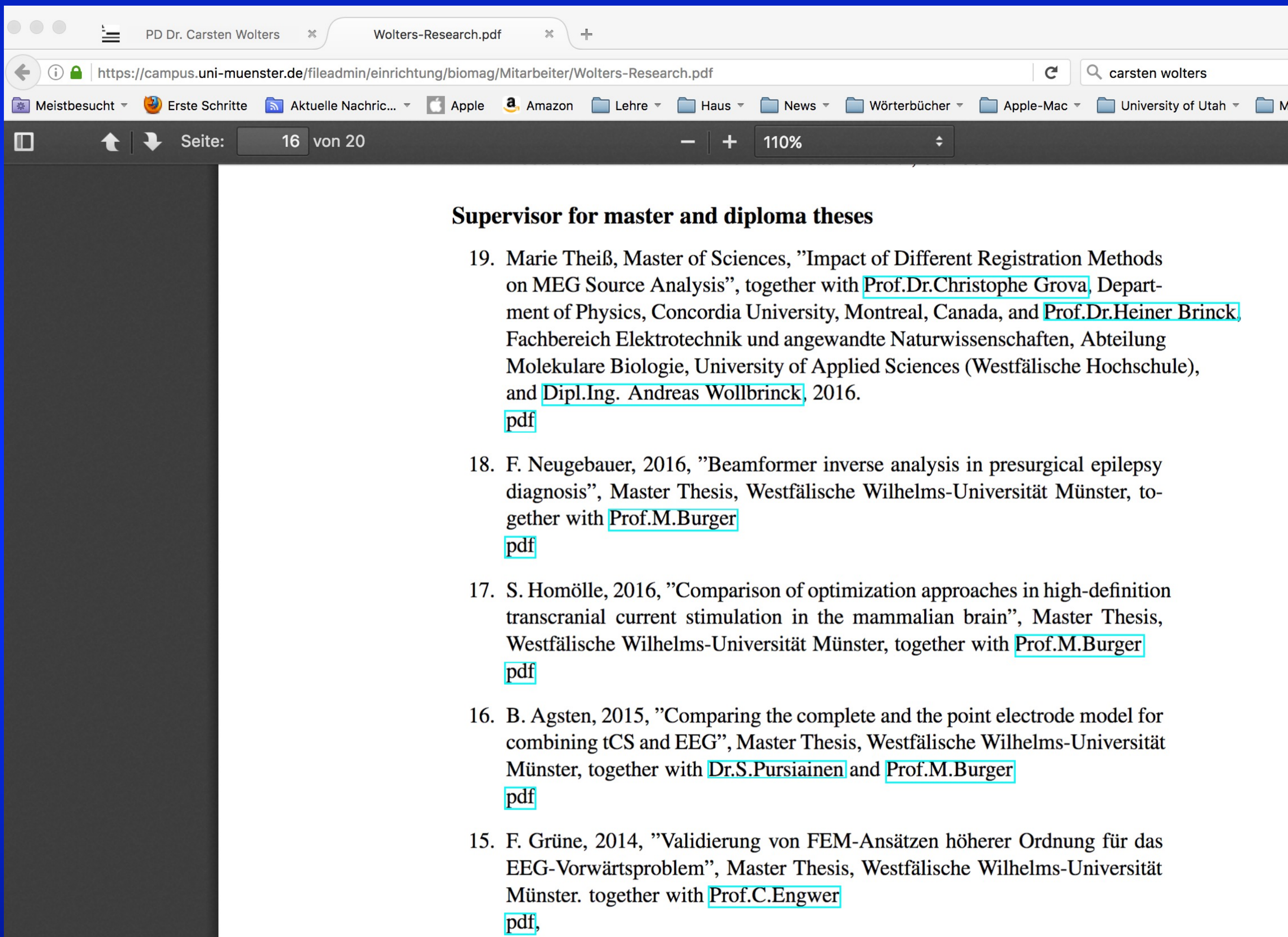


**Supervisor for master and diploma theses**

19. Marie Theiß, Master of Sciences, "Impact of Different Registration Methods on MEG Source Analysis", together with Prof.Dr.Christophe Grova, Department of Physics, Concordia University, Montreal, Canada, and Prof.Dr.Heiner Brinck, Fachbereich Elektrotechnik und angewandte Naturwissenschaften, Abteilung Molekulare Biologie, University of Applied Sciences (Westfälische Hochschule), and Dipl.Ing. Andreas Wollbrinck, 2016.
pdf

18. F. Neugebauer, 2016, "Beamformer inverse analysis in presurgical epilepsy diagnosis", Master Thesis, Westfälische Wilhelms-Universität Münster, together with Prof.M.Burger
pdf

17. S. Homölle, 2016, "Comparison of optimization approaches in high-definition transcranial current stimulation in the mammalian brain", Master Thesis, Westfälische Wilhelms-Universität Münster, together with Prof.M.Burger
pdf

16. B. Agsten, 2015, "Comparing the complete and the point electrode model for combining tCS and EEG", Master Thesis, Westfälische Wilhelms-Universität Münster, together with Dr.S.Pursiainen and Prof.M.Burger
pdf

15. F. Grüne, 2014, "Validierung von FEM-Ansätzen höherer Ordnung für das EEG-Vorwärtsproblem", Master Thesis, Westfälische Wilhelms-Universität Münster. together with Prof.C.Engwer
pdf,

[Florian Grüne, Master thesis Mathematics, *University of Münster,* 2014]

# Florian Grüne

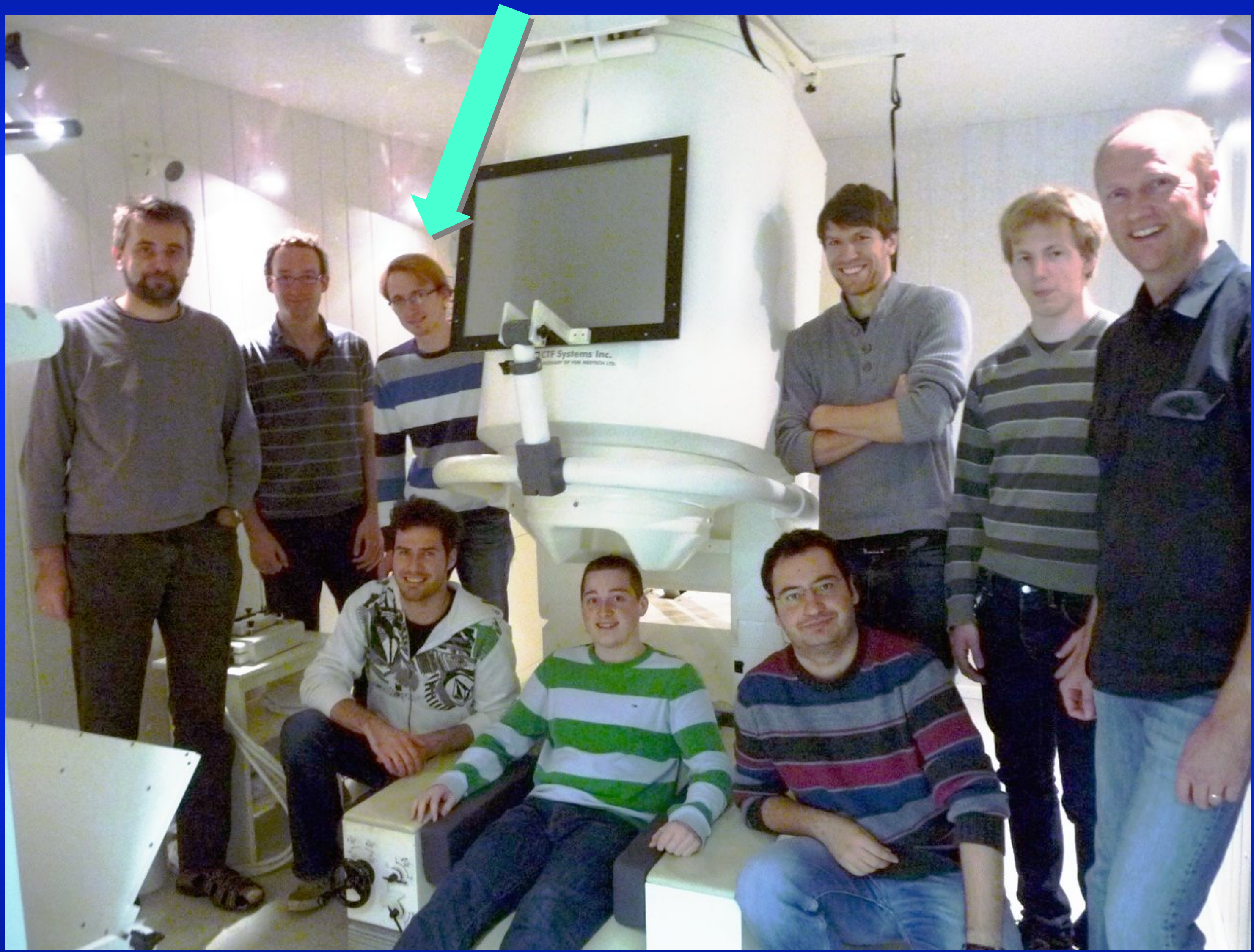


[Florian Grüne, Master thesis Mathematics, *University of Münster,* 2014]

# 4 layer sphere model and meshes

| Gewebetyp | Radius [mm] | Leitfähigkeit [S/m] |
|---|---|---|
| Gehirn | 78 | 0.33 |
| Liquor | 80 | 1.79 |
| Schädel | 86 | 0.0042 |
| Haut | 92 | 0.33 |

Tabelle 4.1: Parametrisierung des 4-Schalen-Kugelmodells

# 4 layer sphere model and meshes

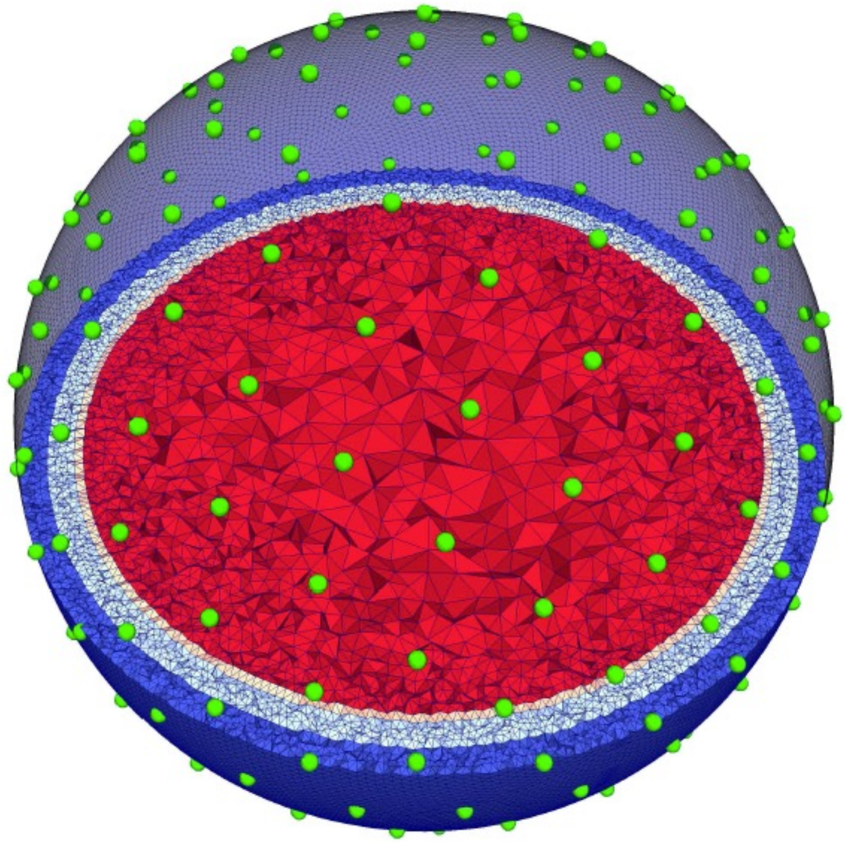

Abbildung 4.1: Schnitt durch das feine Rechennetz (tet519K) des vierschichtigen Kopfmodells. Die Elektroden sind grün gefärbt. Die anderen Farben repräsentieren die unterschiedlichen Gewebetypen.

[Florian Grüne, Master thesis Mathematics, *University of Münster,* 2014]

# 4 layer sphere model and meshes

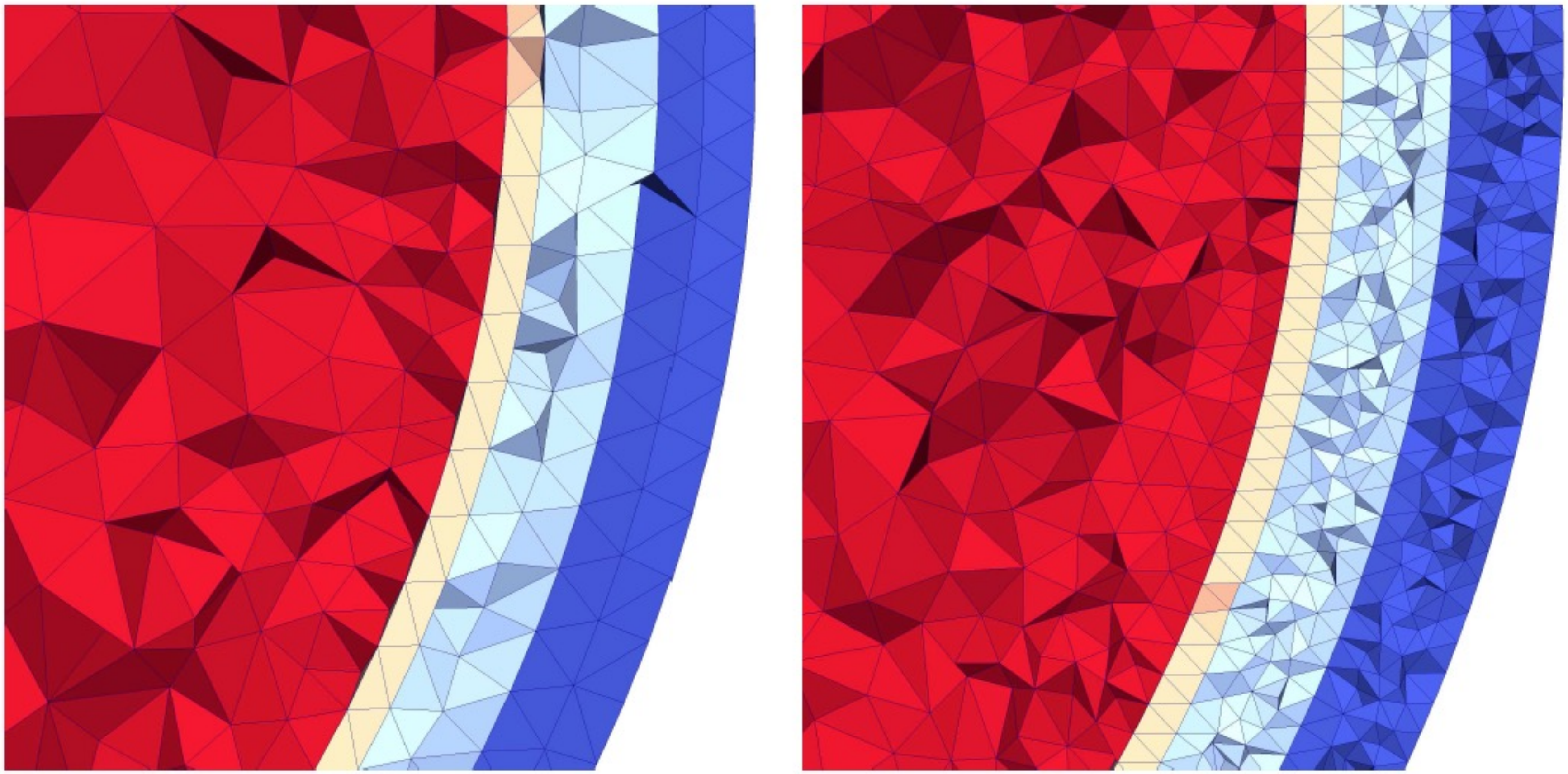

Abbildung 4.2: Links: Detailansicht des grobe Rechennetzes (tet64K). Rechts: Detailansicht des feinen Rechennetzes (tet519K). Die Farben repräsentieren die unterschiedlichen Gewebetypen.

[Florian Grüne, Master thesis Mathematics, *University of Münster,* 2014]

# 4 layer sphere model and meshes

| Rechennetz | #Knoten | #Elemente | #DoF $P_1$ | #DoF $P_2$ | #DoF $P_3$ |
|---|---|---|---|---|---|
| tet64K | 64.060 | 371.947 | 64.060 | 507.956 | 1.703.636 |
| tet519K | 518.730 | 3.159.575 | 518.730 | 4.232.665 | −− |

Tabelle 4.2: Daten der Rechennetze (tet64K) und (tet519K) für die Validierung

[Florian Grüne, Master thesis Mathematics, *University of Münster,* 2014]

# Difference measures between analytical and numerical EEG forward solution

$$\mathrm{RDM}(u_{\mathrm{num}}, u_{\mathrm{ana}}) := \left\| \frac{u_{\mathrm{num}}}{\| u_{\mathrm{num}} \|_2} - \frac{u_{\mathrm{ana}}}{\| u_{\mathrm{ana}} \|_2} \right\|_2$$

$$\mathrm{MAG}(u_{\mathrm{num}}, u_{\mathrm{ana}}) := \frac{\| u_{\mathrm{num}} \|_2}{\| u_{\mathrm{ana}} \|_2}$$

RDM(%)=RDM / 2*100

$$\mathrm{MAG}(\%) = |1 - \mathrm{MAG}| \cdot 100\%.$$

# Boxplots

## Boxplot

Der **Boxplot** (auch **Box-Whisker-Plot** oder deutsch **Kastengrafik**) ist ein Diagramm, das zur grafischen Darstellung der Verteilung eines mindestens ordinalskalierten Merkmals verwendet wird. [1] [2] [3] Es fasst dabei verschiedene robuste Streuungs- und Lagemaße in einer Darstellung zusammen. Ein Boxplot soll schnell einen Eindruck darüber vermitteln, in welchem Bereich die Daten liegen und wie sie sich über diesen Bereich verteilen. Deshalb werden alle Werte der sogenannten Fünf-Punkte-Zusammenfassung, also der Median, die zwei Quartile und die beiden Extremwerte, dargestellt.

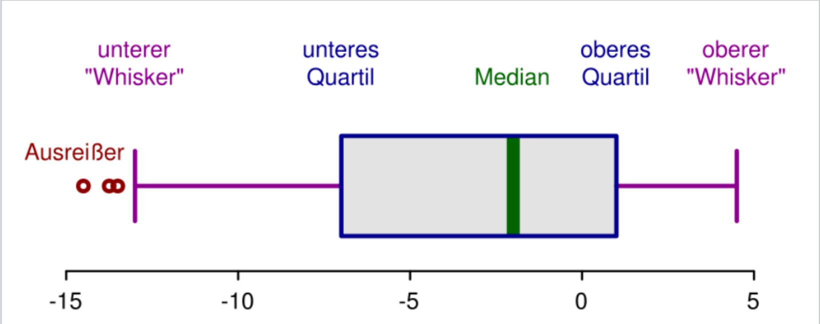


Ein horizontaler Boxplot über einem Zahlenstrahl dargestellt

**Inhaltsverzeichnis** [Verbergen]

Der **Median** oder **Zentralwert** ist ein Mittelwert in der Statistik und ein Lageparameter. Der Median einer Auflistung von Zahlenwerten ist der Wert, der an der mittleren (zentralen) Stelle steht, wenn man die Werte der Größe nach sortiert. Beispielsweise ist für die Werte 4, 1, 37, 2, 1 die Zahl 2 der Median, nämlich die mittlere Zahl in 1, 1, 2, 4, 37.

### Box [ Bearbeiten | Quelltext bearbeiten ]

Die Box entspricht dem Bereich, in dem die mittleren 50 % der Daten liegen. Sie wird also durch das obere und das untere Quartil begrenzt, und die Länge der Box entspricht dem Interquartilsabstand (englisch *interquartile range*, IQR). Dieser ist ein Maß der Streuung der Daten, welches durch die Differenz des oberen und unteren Quartils bestimmt wird. Des Weiteren wird der Median als durchgehender Strich in der Box eingezeichnet. Dieser Strich teilt das gesamte Diagramm in zwei Bereiche, in denen jeweils 50 % der Daten liegen. Durch seine Lage innerhalb der Box bekommt man also einen Eindruck von der Schiefe der den Daten zugrunde liegenden Verteilung vermittelt. Ist der Median im linken Teil der Box, so ist die Verteilung rechtsschief, und umgekehrt.

[Florian Grüne, Master thesis Mathematics, *University of Münster,* 2014]

# Boxplots

## Antenne (Whisker) [ Bearbeiten | Quelltext bearbeiten ]

Durch die Antennen werden die außerhalb der Box liegenden Werte dargestellt. Im Gegensatz zur Definition der Box ist die Definition der Antennen nicht einheitlich.

Eine mögliche Definition, die von John W. Tukey stammt, besteht darin, die Länge der Whisker auf maximal das 1,5-Fache des Interquartilsabstands (1,5×IQR) zu beschränken. Dabei endet der Whisker jedoch nicht genau nach dieser Länge, sondern bei dem Wert aus den Daten, der noch innerhalb dieser Grenze liegt. Die Länge der Whisker wird also durch die Datenwerte und nicht allein durch den Interquartilsabstand bestimmt. Dies ist auch der Grund, warum die Whisker nicht auf beiden Seiten gleich lang sein müssen. Gibt es keine Werte außerhalb der Grenze von 1,5×IQR, wird die Länge des Whiskers durch den maximalen und minimalen Wert festgelegt. Andernfalls werden die Werte außerhalb der Whisker separat in das Diagramm eingetragen. Diese Werte können dann als ausreißerverdächtig behandelt werden oder werden direkt als Ausreißer bezeichnet.

Häufig werden Ausreißer, die zwischen 1,5×IQR und 3×IQR liegen, als „milde“ Ausreißer bezeichnet und Werte, die über 3×IQR liegen, als „extreme“ Ausreißer. Diese werden dann auch meist unterschiedlich im Diagramm gekennzeichnet.

Eine weitere mögliche Definition ist diese, dass die Whisker bis zum größten bzw. kleinsten Wert aus den Daten reichen. In dieser Darstellung sind dann keine Ausreißer mehr erkennbar, da die Box inklusive Whisker die gesamte Spannweite der Daten abdeckt.

In einer anderen Variante erfolgt die Berechnung des unteren Whisker als 2,5-%-Quantil und die Berechnung des oberen als 97,5-%-Quantil. Innerhalb der Whiskergrenzen liegen somit 95 % aller beobachteten Werte. In dieser Darstellung gibt es also (je nach Quantilsdefinition) ab einem bestimmten Stichprobenumfang immer einzeln dargestellte Punkte (die man dann nicht automatisch als Ausreißer interpretieren sollte).

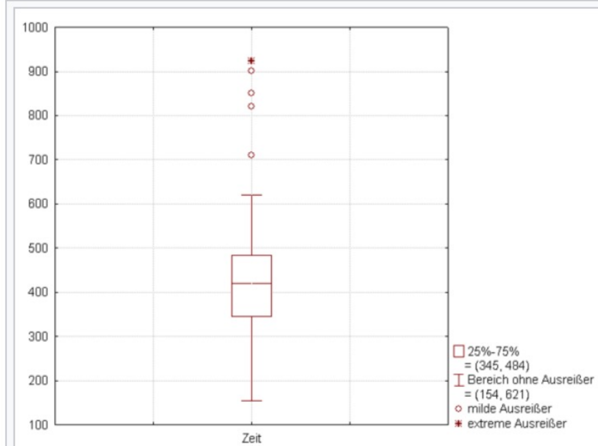


Box-Plot mit Whiskern der Länge 1,5×IQR

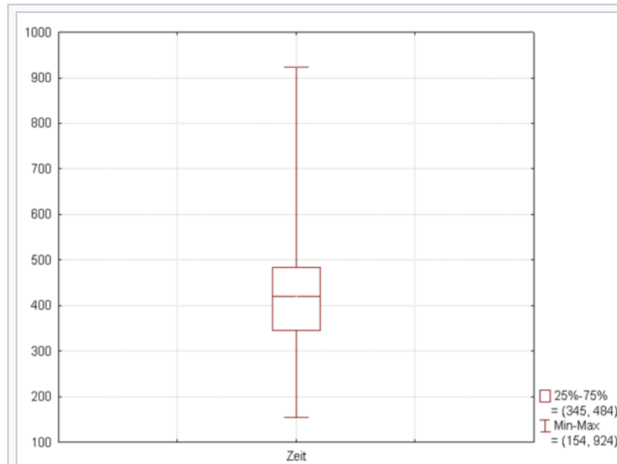


Box-Plot derselben Daten mit Whiskern vom Minimum bis zum Maximum der Daten

[Florian Grüne, Master thesis Mathematics, *University of Münster,* 2014]

# Higher order basis functions for subtraction

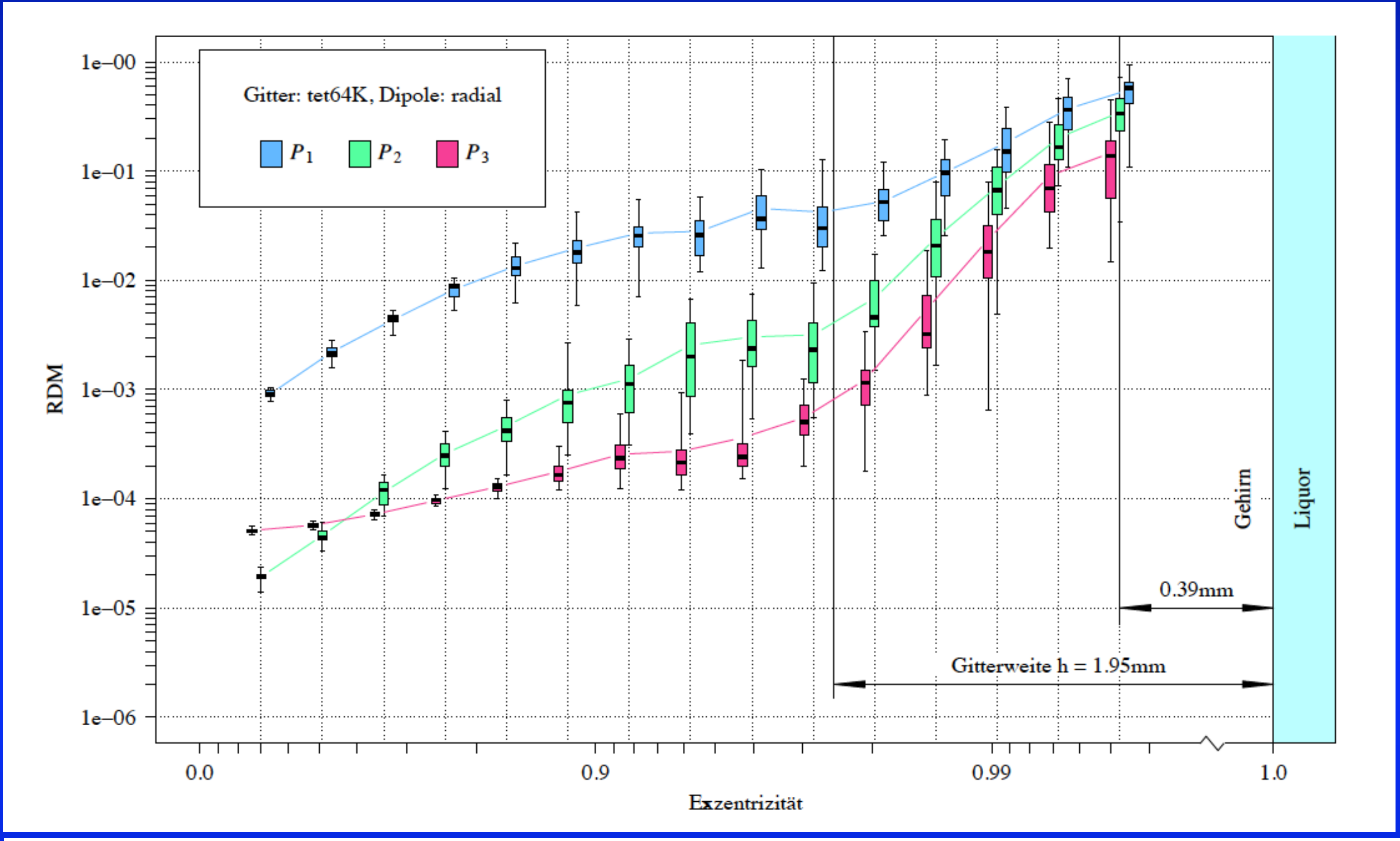


Abbildung 4.3: RDM für radiale Dipole, dargestellt durch Boxplots. Jede Box repräsentiert 25 Dipole. Die Boxen wurden zur besseren Darstellung seitlich verschoben. Die senkrechten Linien des Gitters geben die tatsächliche Exzentrizität der Dipole wieder. Die Kurven zeigen zusätzlich das arithmetische Mittel des RDM.

**0.99 means 0.78 mm to CSF**

[Florian Grüne, Master thesis Mathematics, *University of Münster,* 2014]

# Higher order basis functions for subtraction

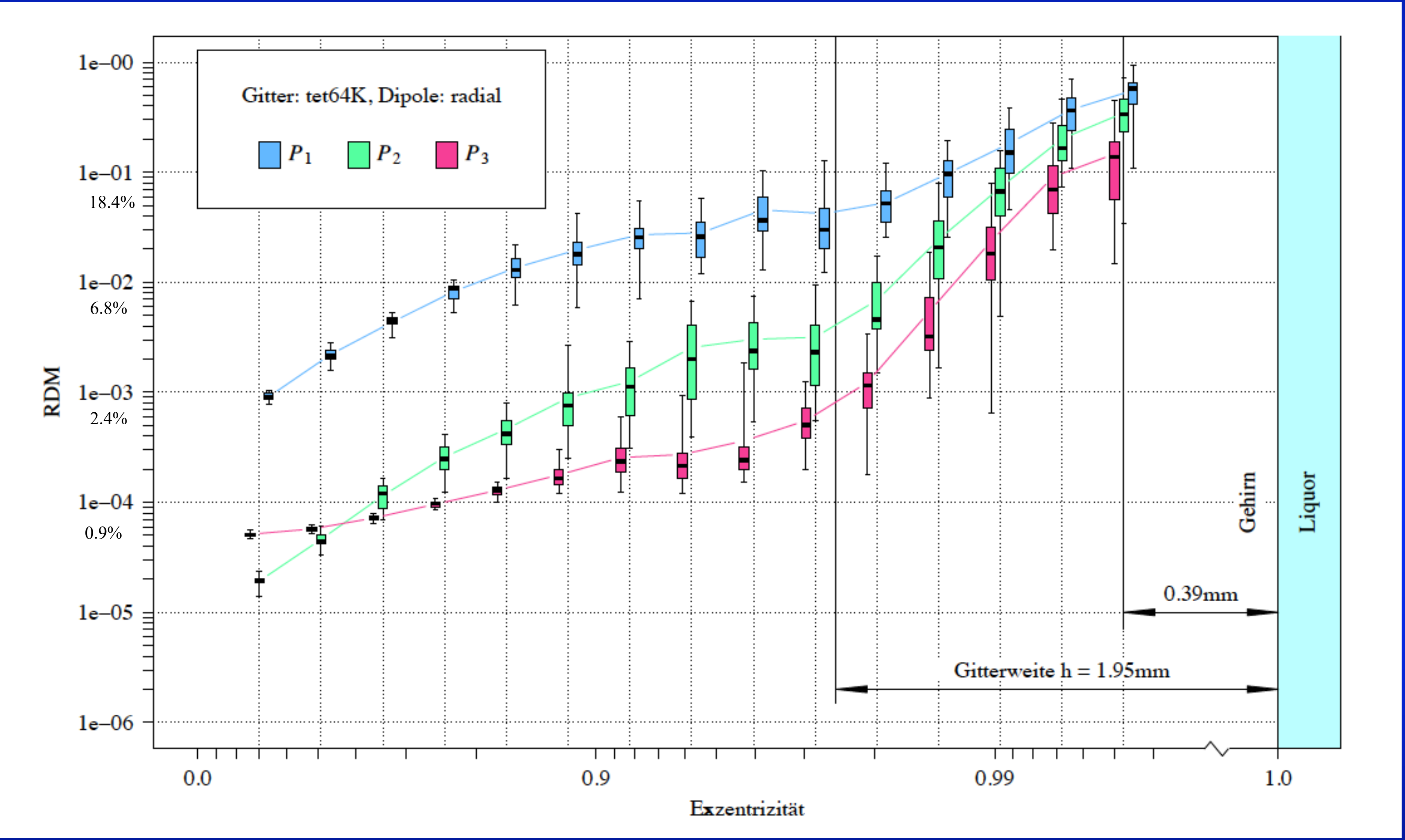

[Florian Grüne, Master thesis Mathematics, *University of Münster,* 2014]

# Higher order basis functions for subtraction

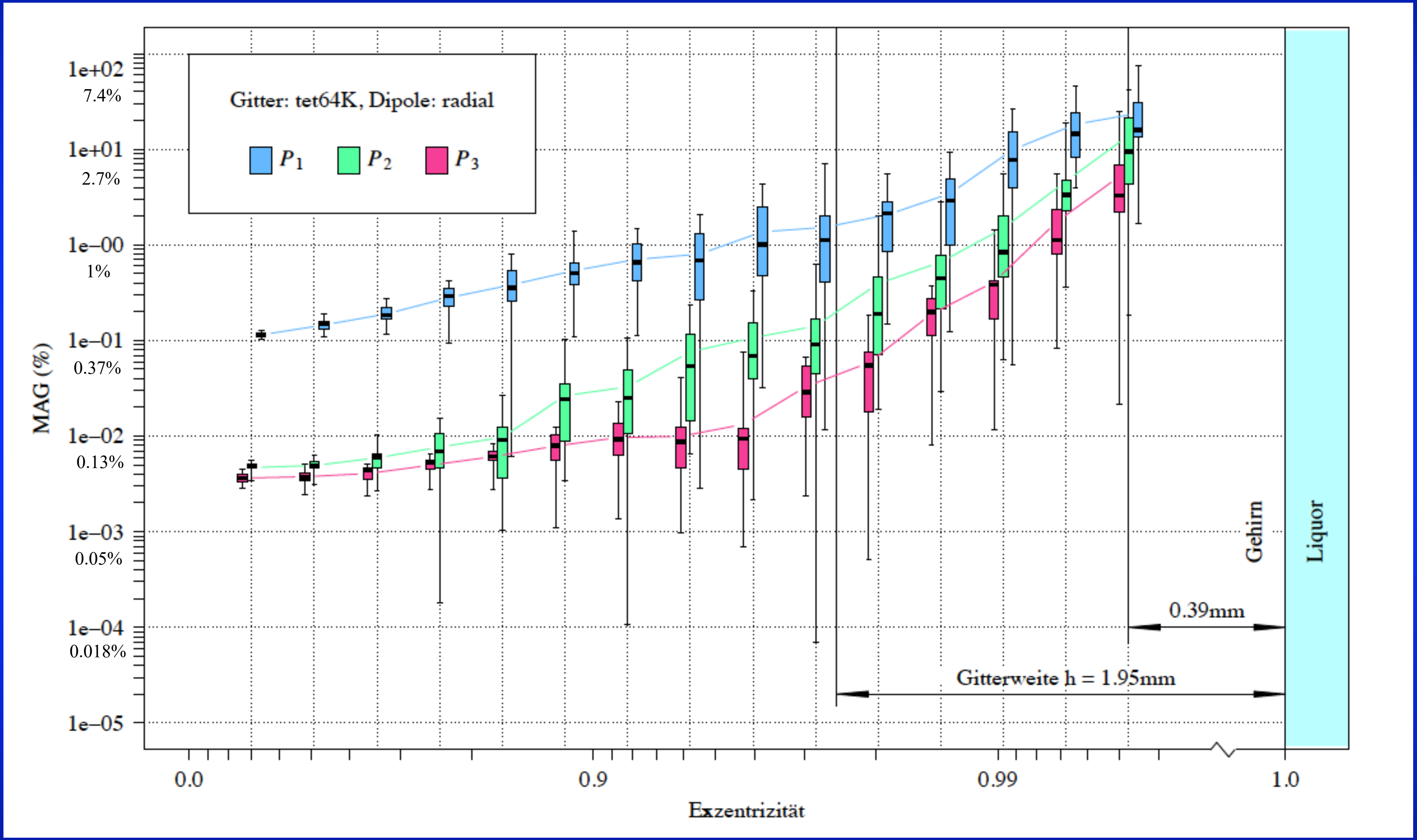

[Florian Grüne, Master thesis Mathematics, *University of Münster,* 2014]

# Higher order basis functions for subtraction

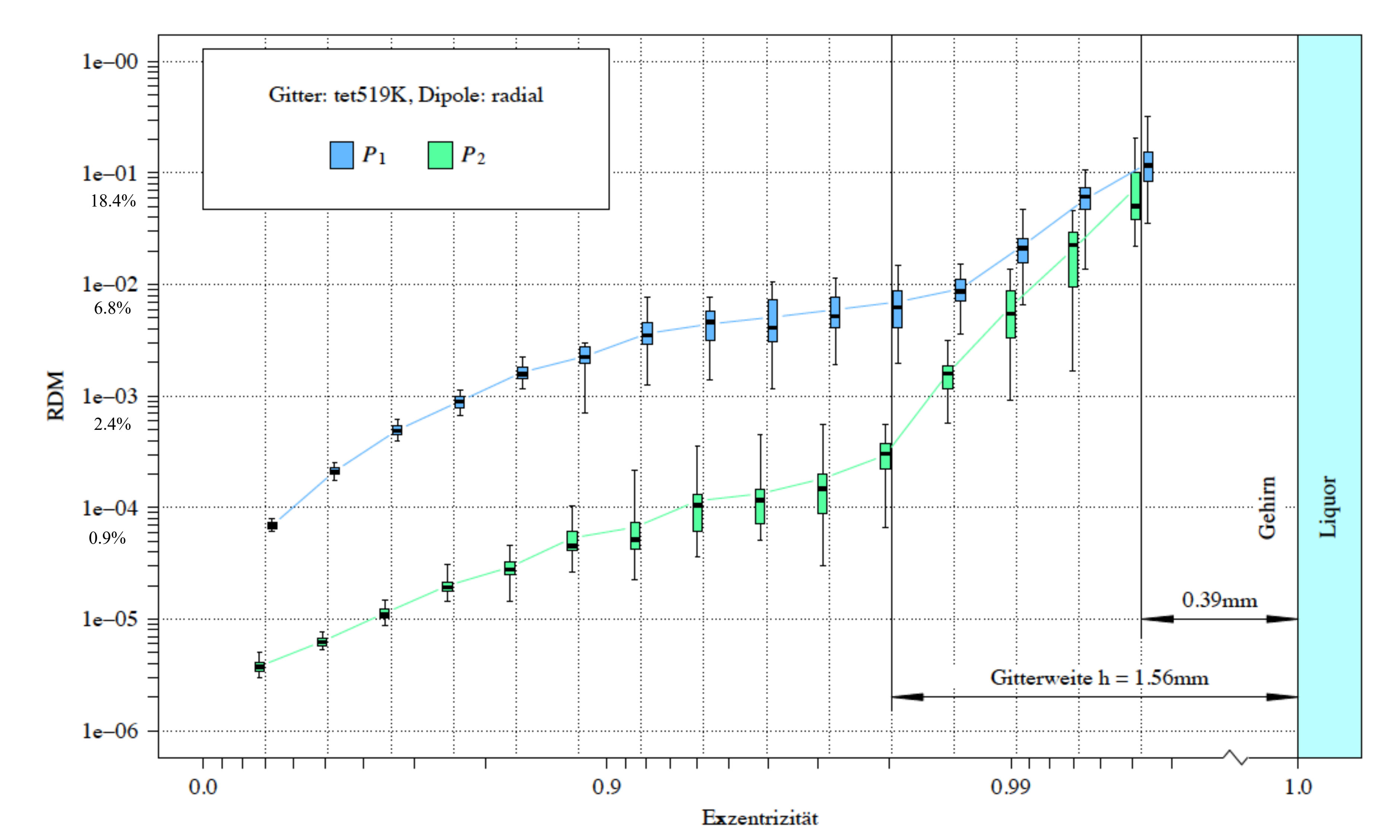

[Florian Grüne, Master thesis Mathematics, *University of Münster,* 2014]

# Higher order basis functions for subtraction

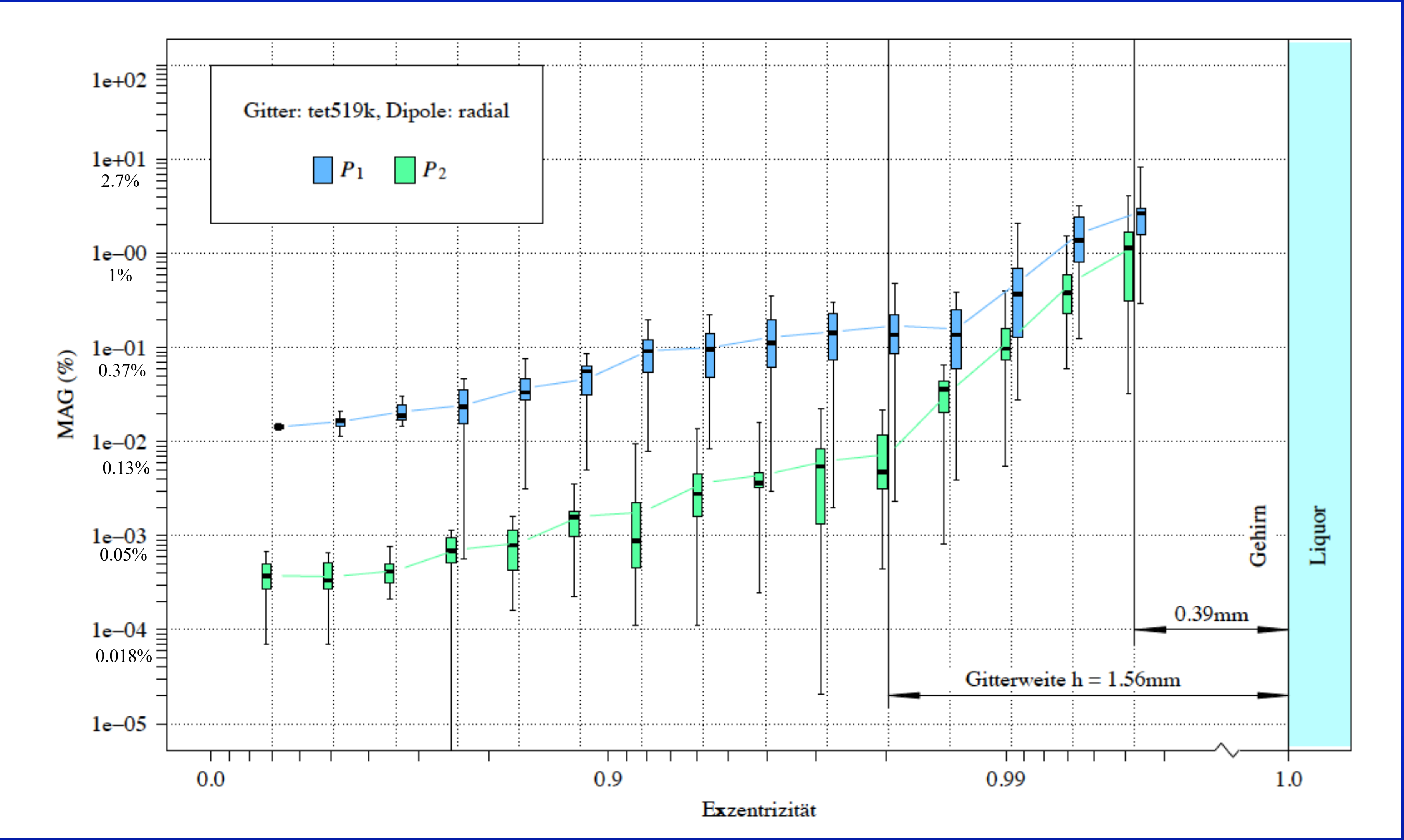

[Florian Grüne, Master thesis Mathematics, *University of Münster,* 2014]

# Higher order basis functions for subtraction

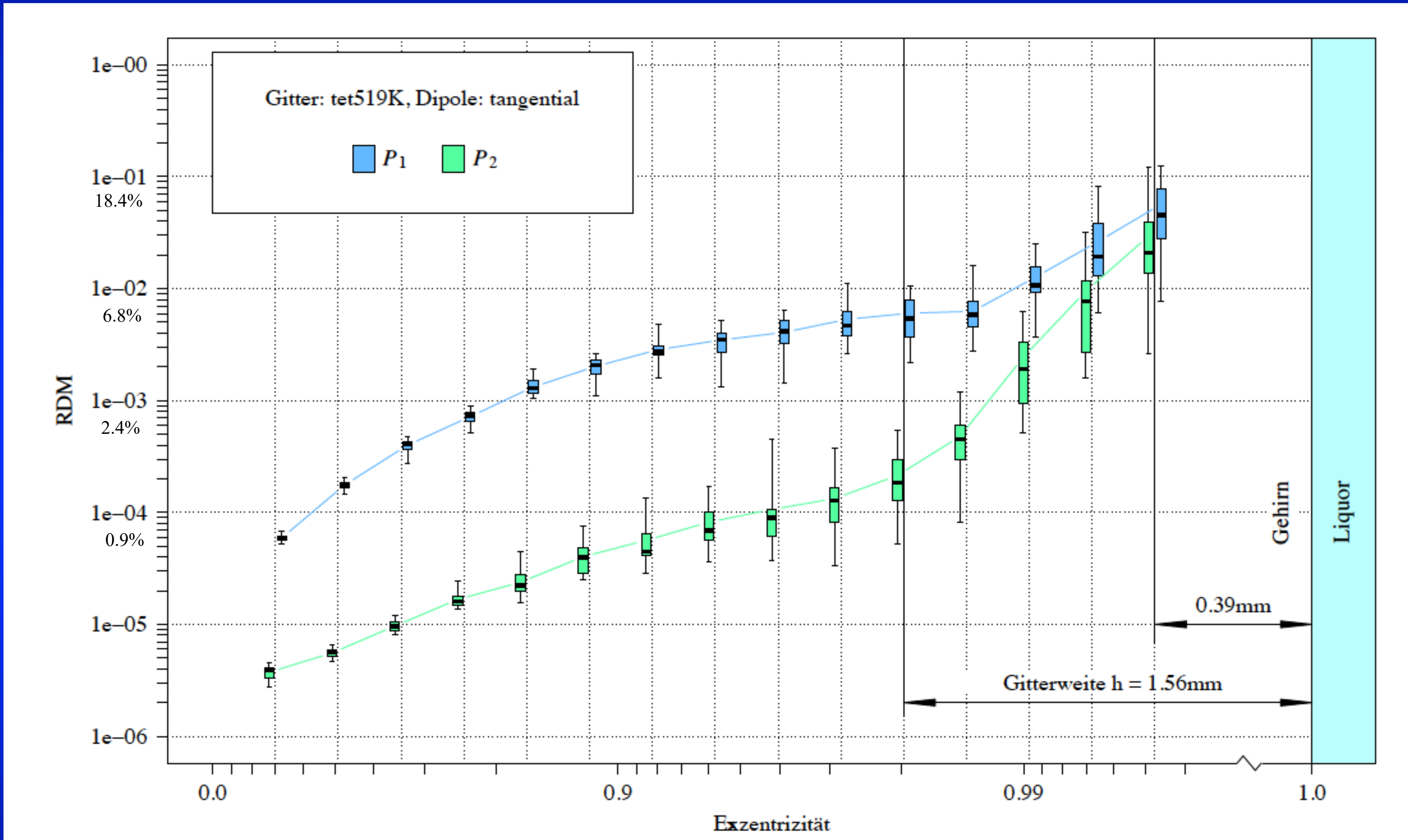

[Florian Grüne, Master thesis Mathematics, *University of Münster*, 2014]

# Higher order basis functions for subtraction

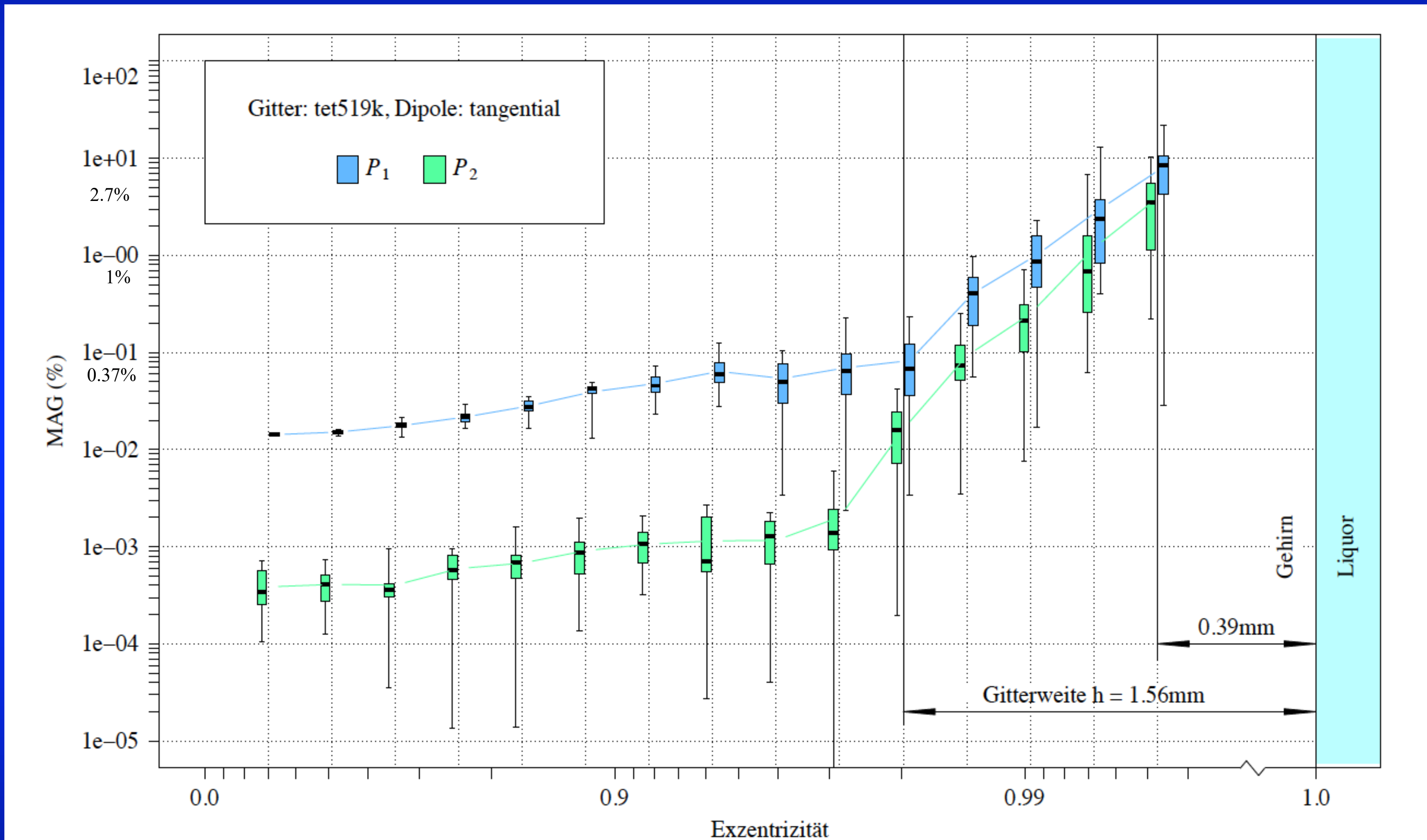

[Florian Grüne, Master thesis Mathematics, *University of Münster,* 2014]

# Higher order basis functions for subtraction

| Rechennetz | #Knoten | #Elemente | #DoF $P_1$ | #DoF $P_2$ | #DoF $P_3$ |
|---|---|---|---|---|---|
| tet64K | 64.060 | 371.947 | 64.060 | 507.956 | 1.703.636 |
| tet519K | 518.730 | 3.159.575 | 518.730 | 4.232.665 | −− |

Tabelle 4.2: Daten der Rechennetze (tet64K) und (tet519K) für die Validierung

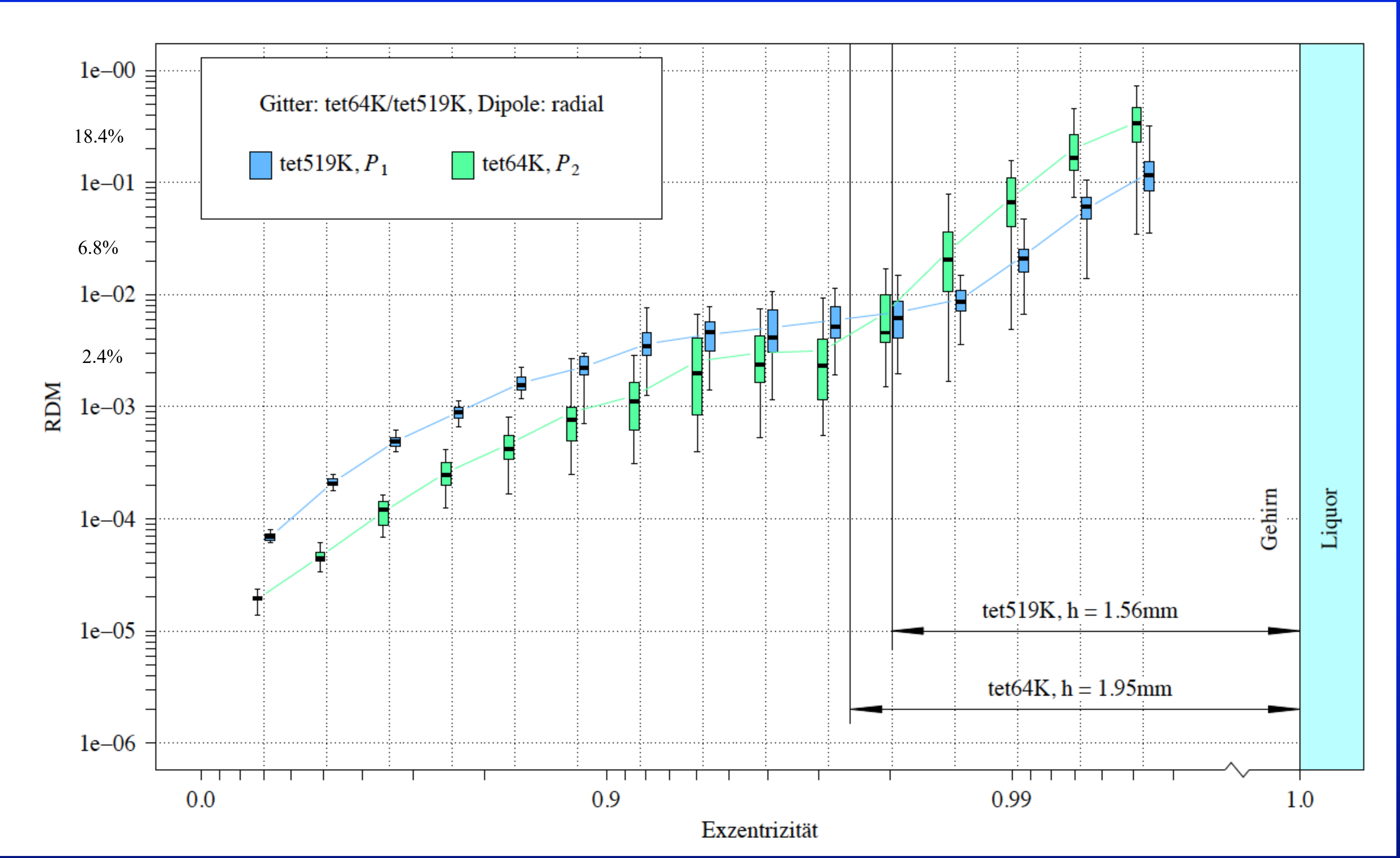

[Florian Grüne, Master thesis Mathematics, *University of Münster,* 2014]

# Computational amount of work for subtraction source model

Ausgeführt wurden die Simulationen auf einem Rechencluster von Amazon Web Services [2]. In Verbindung mit dem Interface StarCluster des MIT [25], kann dort auf einfache Weise Hardware gemietet werden. Unsere Simulationen wurden auf einer Instanz mit einer Intel(R) Xeon(R) CPU E5-2680 v2 @ 2.80GHz und 60 GB RAM durchgeführt. Die CPU besteht aus zehn physikalischen Kernen die insgesamt bis zu 32 Threads unterstützen.

| | tet64K $P_1$ | tet64K $P_2$ | tet64K $P_3$ | tet519K $P_1$ | tet519K $P_2$ |
|---|---|---|---|---|---|
| Residuum Assemblieren | 2.84 s | 10.39 s | 73.10 s | 25.52 s | 86.69 s |
| LGS Lösen | 1.23 s | 51.42 s | 523.79 s | 27.28 s | 1168.90 s |
| Gesamtzeit für Dipol | 5.54 s | 63.71 s | 599.36 s | 65.89 s | 1273.10 s |

Tabelle 4.3: Sequenzielle Rechenzeiten

# Computational amount of work for subtraction source model in DUNEuro

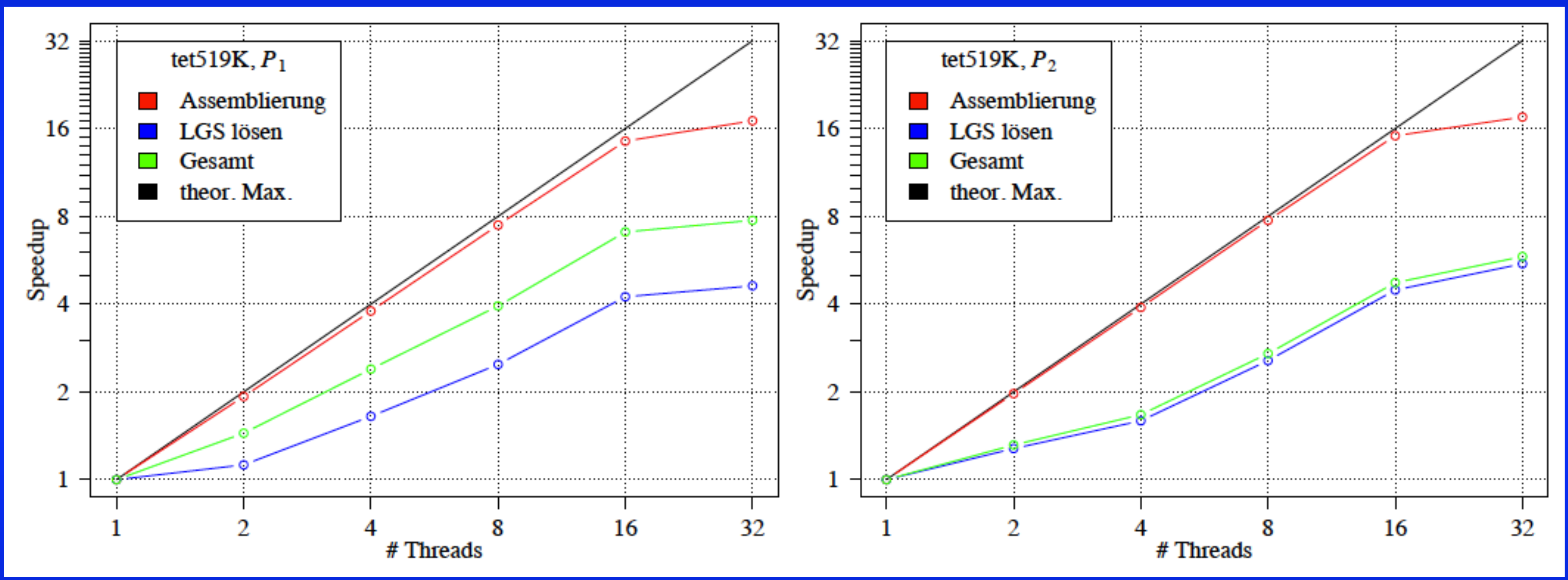


SSORk-CG was used for non-overlapping domain decomposition as a solver.
AMG-CG solver might further decrease computational speed

# PI, Venant and Whitney source models

# Introduction





2648 IEEE TRANSACTIONS ON BIOMEDICAL ENGINEERING, VOL. 62, NO. 11, NOVEMBER 2015

## Comparison Study for Whitney (Raviart–Thomas)-Type Source Models in Finite-Element-Method-Based EEG Forward Modeling

Martin Bauer, Sampsa Pursiainen*, Johannes Vorwerk, Harald Köstler, and Carsten H. Wolters

M. Bauer and H. Köstler are with the Department of Computer Science, Friedrich-Alexander-University Erlangen-Nürnberg.

*S. Pursiainen is with the Department of Mathematics and Systems Analysis, Aalto University, Helsinki, Finland, and also with the Department of Mathematics, Tampere University of Technology, 33720 Tampere, Finland (e-mail: sampsa.pursiainen@iki.fi).

J. Vorwerk and C. H. Wolters are with the Institute for Biomagnetism and Biosignalanalysis, University of Münster.

[Bauer, Pursiainen, Vorwerk, Köstler & Wolters, *IEEE TBME*, 2015]

# Reminder: Link for literature to own work:

**https://campus.uni-muenster.de/biomag/das-institut/mitarbeiter/carsten-wolters/**

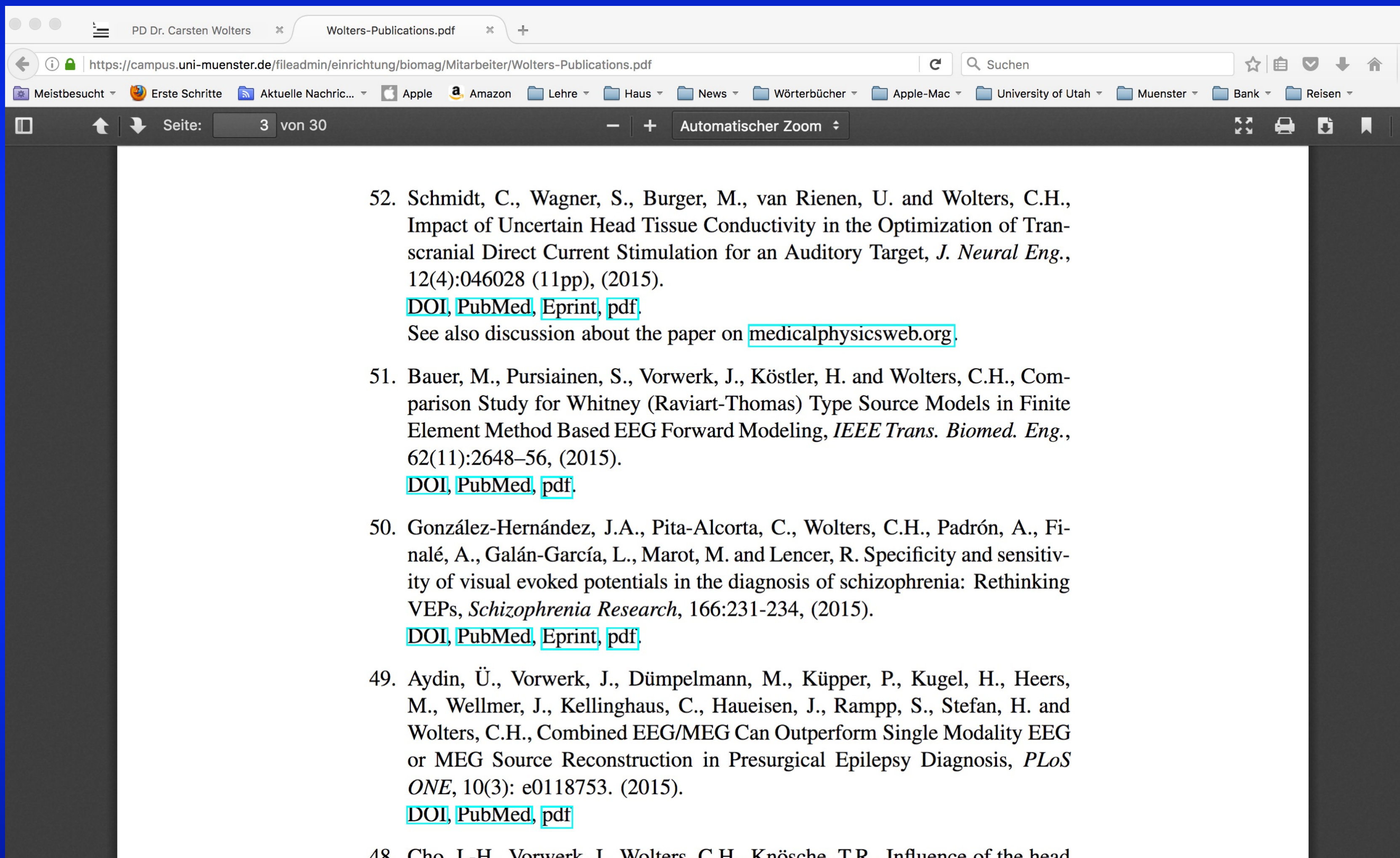


52. Schmidt, C., Wagner, S., Burger, M., van Rienen, U. and Wolters, C.H., Impact of Uncertain Head Tissue Conductivity in the Optimization of Transcranial Direct Current Stimulation for an Auditory Target, *J. Neural Eng.*, 12(4):046028 (11pp), (2015).
DOI, PubMed, Eprint, pdf.
See also discussion about the paper on medicalphysicsweb.org.

51. Bauer, M., Pursiainen, S., Vorwerk, J., Köstler, H. and Wolters, C.H., Comparison Study for Whitney (Raviart-Thomas) Type Source Models in Finite Element Method Based EEG Forward Modeling, *IEEE Trans. Biomed. Eng.*, 62(11):2648–56, (2015).
DOI, PubMed, pdf.

50. González-Hernández, J.A., Pita-Alcorta, C., Wolters, C.H., Padrón, A., Finalé, A., Galán-García, L., Marot, M. and Lencer, R. Specificity and sensitivity of visual evoked potentials in the diagnosis of schizophrenia: Rethinking VEPs, *Schizophrenia Research*, 166:231-234, (2015).
DOI, PubMed, Eprint, pdf.

49. Aydin, Ü., Vorwerk, J., Dümpelmann, M., Küpper, P., Kugel, H., Heers, M., Wellmer, J., Kellinghaus, C., Haueisen, J., Rampp, S., Stefan, H. and Wolters, C.H., Combined EEG/MEG Can Outperform Single Modality EEG or MEG Source Reconstruction in Presurgical Epilepsy Diagnosis, *PLoS ONE*, 10(3): e0118753. (2015).
DOI, PubMed, pdf

48. Cho, J.-H., Vorwerk, J., Wolters, C.H., Knösche, T.R., Influence of the head

[Pursiainen, Vorwerk & Wolters, *Phys Med Biol*, 2016]

# Introduction



**IOP** Publishing | Institute of Physics and Engineering in Medicine — Physics in Medicine & Biology

Phys. Med. Biol. **61** (2016) 8502–8520 — doi:10.1088/0031-9155/61/24/8502

## Electroencephalography (EEG) forward modeling via *H*(div) finite element sources with focal interpolation

**S Pursiainen[1,4], J Vorwerk[2,3] and C H Wolters[2]**

[1] Department of Mathematics, Tampere University of Technology, PO Box 553, FI-33101 Tampere, Finland
[2] Institute for Biomagnetism and Biosignalanalysis, University of Münster, Malmedyweg 15, 84149 Münster, Germany
[3] Scientific Computing and Imaging (SCI) Institute, University of Utah, 72 S Central Campus Drive, Salt Lake City, UT 84112, USA

E-mail: sampsa.pursiainen@tut.fi

Received 16 August 2015, revised 21 September 2016
Accepted for publication 18 October 2016
Published 15 November 2016

CrossMark

[Pursiainen, Vorwerk & Wolters, *Phys Med Biol*, 2016]

# Reminder: Link for literature to own work:

**https://campus.uni-muenster.de/biomag/das-institut/mitarbeiter/carsten-wolters/**

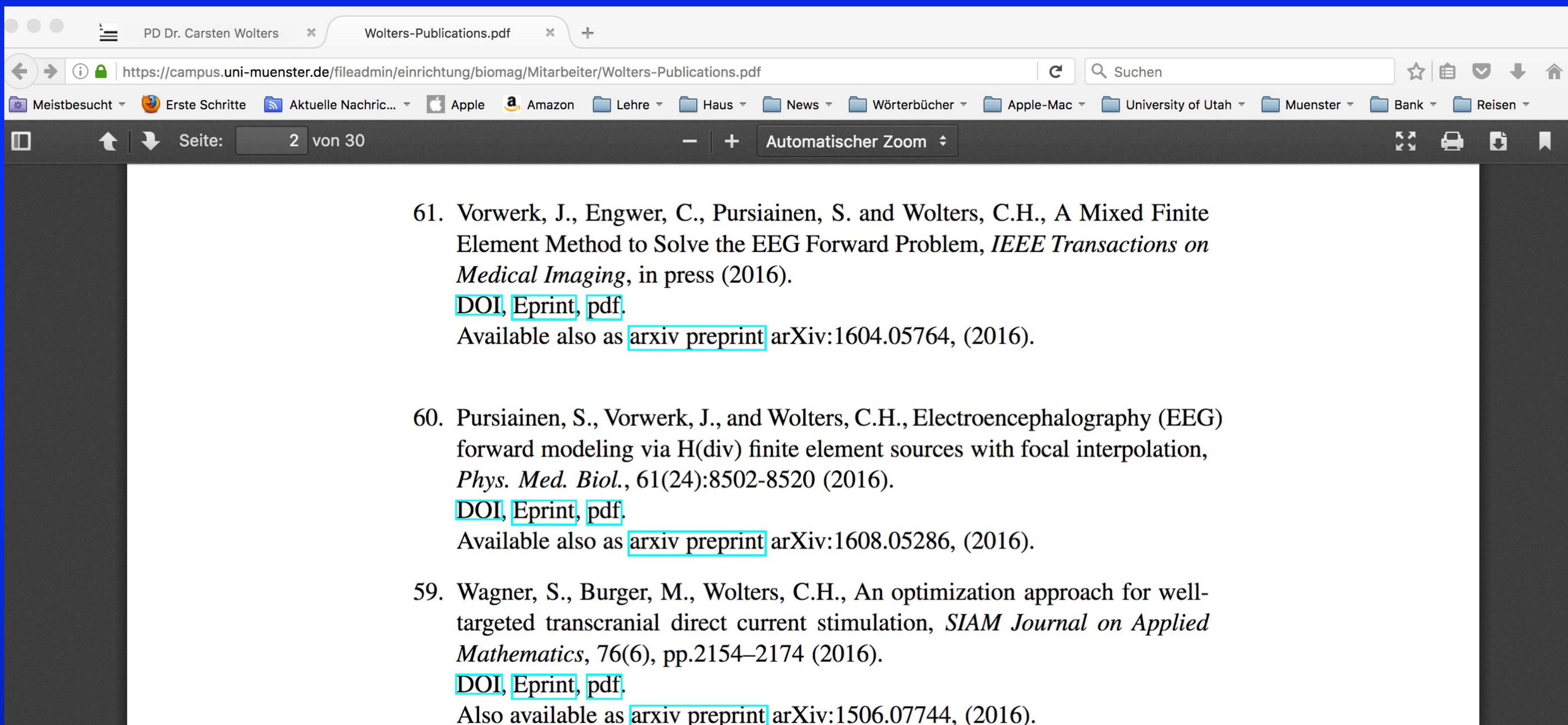


61. Vorwerk, J., Engwer, C., Pursiainen, S. and Wolters, C.H., A Mixed Finite Element Method to Solve the EEG Forward Problem, *IEEE Transactions on Medical Imaging*, in press (2016).
DOI, Eprint, pdf.
Available also as arxiv preprint arXiv:1604.05764, (2016).

60. Pursiainen, S., Vorwerk, J., and Wolters, C.H., Electroencephalography (EEG) forward modeling via H(div) finite element sources with focal interpolation, *Phys. Med. Biol.*, 61(24):8502-8520 (2016).
DOI, Eprint, pdf.
Available also as arxiv preprint arXiv:1608.05286, (2016).

59. Wagner, S., Burger, M., Wolters, C.H., An optimization approach for well-targeted transcranial direct current stimulation, *SIAM Journal on Applied Mathematics*, 76(6), pp.2154–2174 (2016).
DOI, Eprint, pdf.
Also available as arxiv preprint arXiv:1506.07744, (2016).

[Bauer, Pursiainen, Vorwerk, Köstler & Wolters, *IEEE TBME*, 2015]

# Source model extent and number of right-hand side non-zeros/computational amount of work

TABLE III
NUMBER OF FINITE-ELEMENT MESH NODES NEEDED TO MODEL A SINGLE DIPOLE SOURCE

| Source orientation | Whitney | St. Venant | PI |
|---|---|---|---|
| free | 8 | $\approx 27$ | 4 |
| fixed | 2 | $\approx 27$ | 4 |

**For free source orientation :**

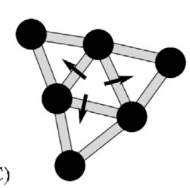

(C)

- Elements that share a face with a given element
- 8 FE mesh nodes
- 4 dipolar sources
- 4 FI sources (black)

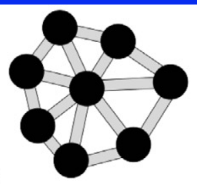

(F)

- Elements sharing a given node
- $\approx$16–27 FE mesh nodes
- $\approx$16–27 monopolar sources

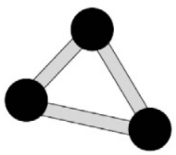

(E)

- A single element
- 4 FE mesh nodes
- 4 monopolar sources

[Bauer, Pursiainen, Vorwerk, Köstler & Wolters, *IEEE TBME*, 2015]

# 4 layer sphere model

TABLE II
PARAMETERIZATION FOR THE ISOTROPIC FOUR-LAYER SPHERE MODEL

| Compartment | Scalp | Skull | CSF | Brain |
|---|---|---|---|---|
| Outer shell radius (mm) | 92 | 86 | 80 | 78 |
| Conductivity (S/m) | 0.33 | 0.0042 | 1.79 | 0.33 |

- **FEM mesh generation: Constrained Delaunay Tetrahedralization with maximal tetrahedra volume of 1.12 $mm^3$ using TetGen, resulting in a tetrahedral mesh with 801K nodes**
- **200 electrodes, regularly distributed over the outer surface**
- **200 sources for each of the following eccentricities: 0.2, 0.4, 0.6, 0.8, 0.99**

[Bauer, Pursiainen, Vorwerk, Köstler & Wolters, *IEEE TBME*, 2015]

# Difference measures between analytical and numerical/simulated EEG forward solution

**Relative Difference Measure (topography difference)**

$$\mathrm{RDM}(\mathbf{u}_{\mathrm{ana}}, \mathbf{u}_{\mathrm{sim}}) = \frac{100}{2}\left\|\frac{\mathbf{u}_{\mathrm{ana}}}{\|\mathbf{u}_{\mathrm{ana}}\|_2} - \frac{\mathbf{u}_{\mathrm{sim}}}{\|\mathbf{u}_{\mathrm{sim}}\|_2}\right\|_2$$

**MAGnitude error**

$$\mathrm{MAG}(\mathbf{u}_{\mathrm{ana}}, \mathbf{u}_{\mathrm{sim}}) = 100\left(\frac{\|\mathbf{u}_{\mathrm{sim}}\|_2}{\|\mathbf{u}_{\mathrm{ana}}\|_2} - 1\right)$$

[Bauer, Pursiainen, Vorwerk, Köstler & Wolters, *IEEE TBME*, 2015]

# Synthetic dipole location and position for Whitney model

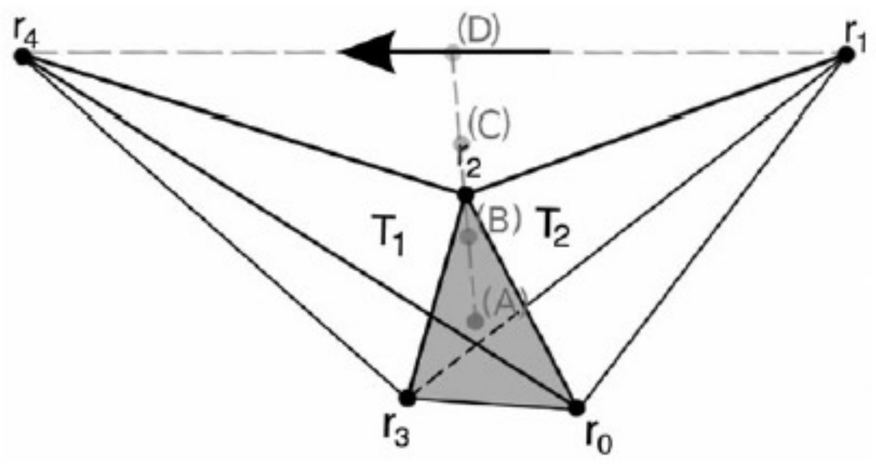


Fig. 1. Whitney basis function supported on two tetrahedra $T_1$ and $T_2$ with source locations (A)–(D) and resulting synthetic dipole for (D) shown by the arrow.

[Bauer, Pursiainen, Vorwerk, Köstler & Wolters, *IEEE TBME*, 2015]

# Whitney source model: Best synthetic source position

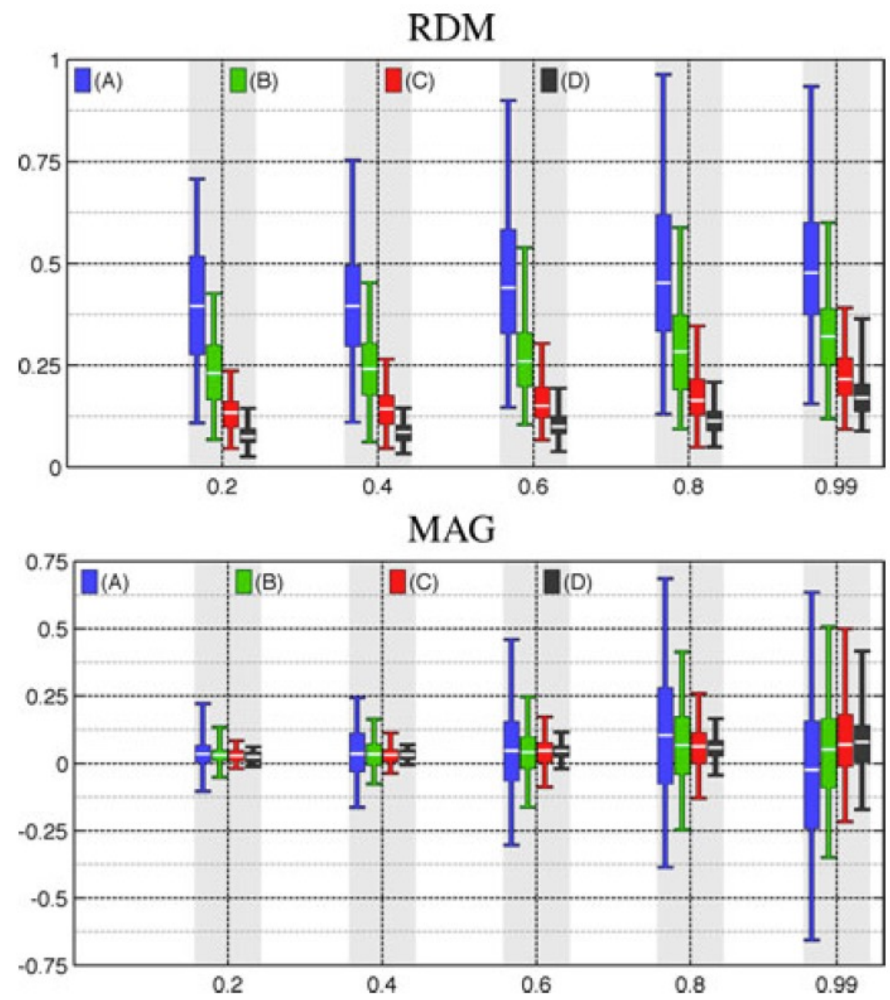


Fig. 3. Synthetic source positions for Whitney approach: RDM (top) and MAG (bottom) for points (A)–(D) as synthetic source positions as shown in Fig. 1 in % error

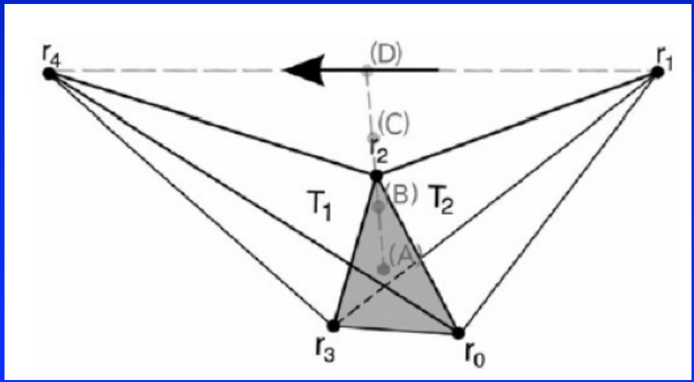


=> (D) is best!

[Bauer, Pursiainen, Vorwerk, Köstler & Wolters, *IEEE TBME*, 2015]

# Whitney source model with arbitrary or fixed orientation

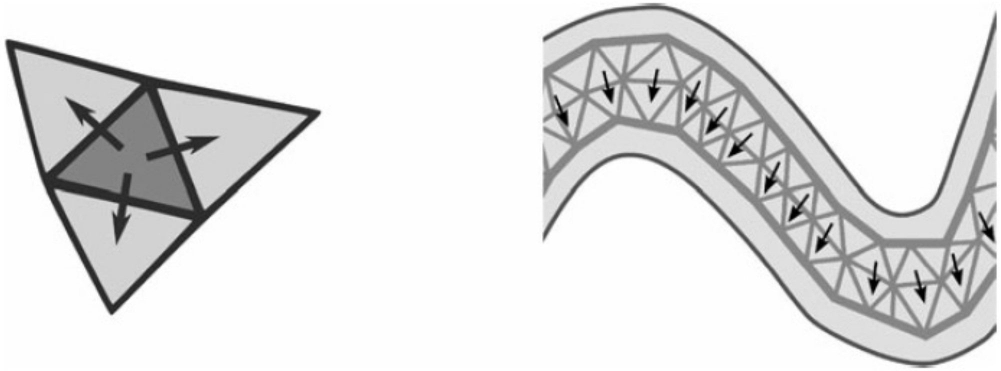

Fig. 2. (Left) To approximate a dipole with an arbitrary orientation, the PBO method utilizes a minimal symmetric combination of elements including a given tetrahedron (dark gray) together with those that share a face with it (light gray). (Right) In case that a very accurate tetrahedralization in the middle of the gray matter compartment (light gray) has been produced, source locations and radially inwards-pointing source orientations can be fixed [32], [33].

[Bauer, Pursiainen, Vorwerk, Köstler & Wolters, *IEEE TBME*, 2015]

# Comparison of source models: Part I: Synthetic source positions and orientations

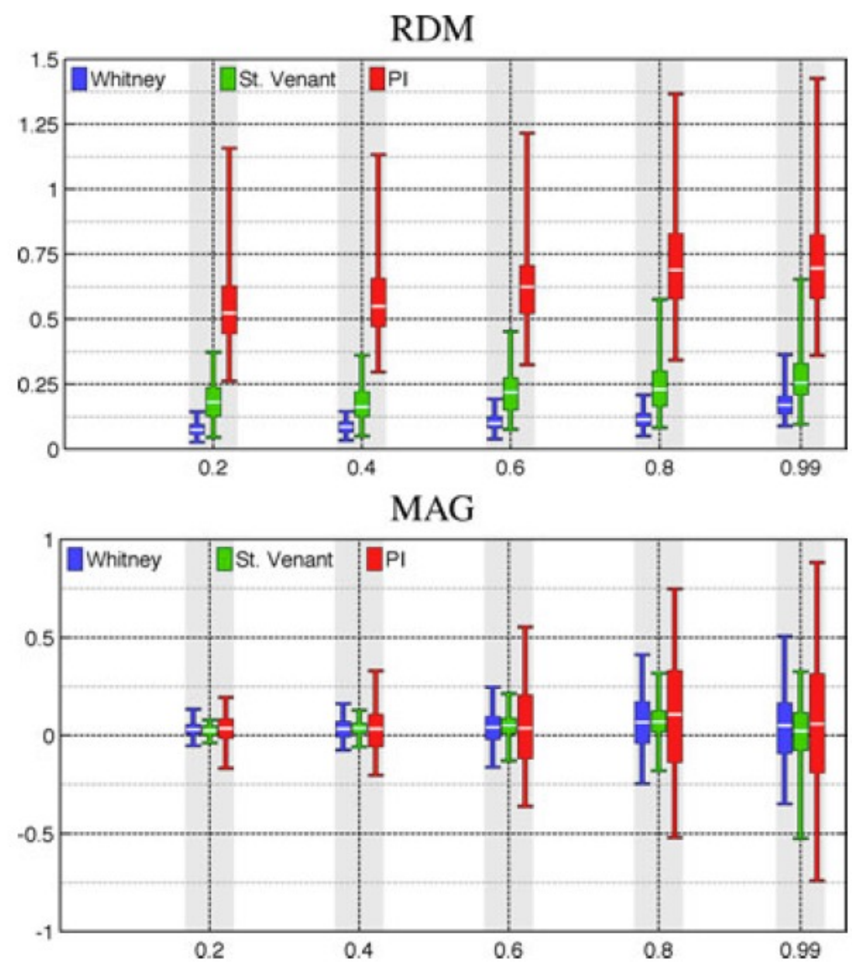


Fig. 4. Fixed source positions and Orientations: RDM (top) and MAG (bottom) in % error

[Bauer, Pursiainen, Vorwerk, Köstler & Wolters, *IEEE TBME*, 2015]

# Comparison of source models:
# Part II: Random source positions and orientations

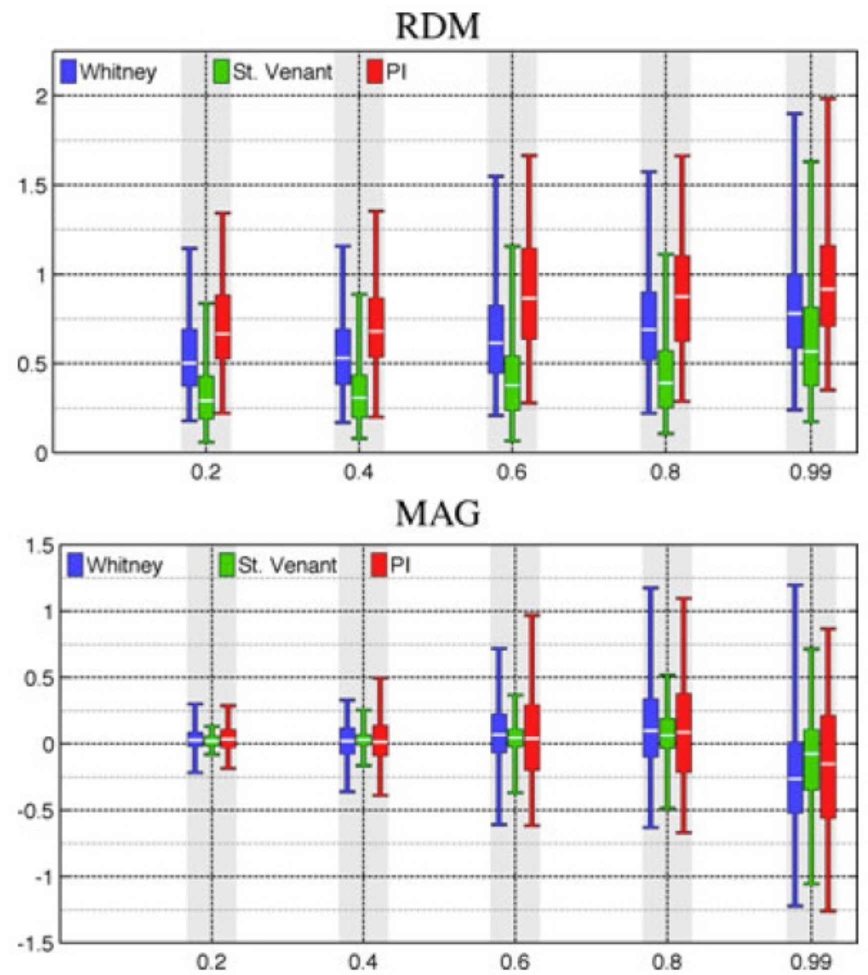


Fig. 5. Random source positions and orientations: RDM (top) and MAG (bottom).

# Discussion: Subtraction source model

- **Pro:**
  - **Theoretically well understood**
  - **Localized subtraction is also very fast (Höltershinken et al., 2023)**
- **Contra:**
  - **Highest sensitivity/inaccuracy for high eccentricities: For model with 519K nodes and P2 basis functions still up to 8% maximal RDM and 1.5% MAG at 0.99 eccentricity (0.78 mm to CSF): Such errors might cause trouble in applications**
  - **Full subtraction is computationally very expensive (will need newest generation of computers, parallelization)**
  - **Less realistic source model (mathematical point-dipole)**

# Discussion: PI source model

- Pro:
  - Very local, fits in one element
  - Computationally very fast
  - With less than 2% RDM and 1.5% MAG at 0.99 eccentricity (0.78 mm to CSF) good enough for application
  - Even more realistic than the mathematical point-dipole
- Contra:
  - Slightly less accurate than Whitney or Venant
  - No resolution within an element when using P1 basis functions

# Discussion: Venant source model

- Pro:
  - With less than 1.7% RDM and 1% MAG at 0.99 eccentricity (0.78 mm to CSF) very accurate source modeling approach
  - Computationally very fast
  - Even more realistic than the mathematical point-dipole
- Contra:
  - Less local, needs about 27 nodes that have to fit into the cortex, which might get difficult in infant models

# Discussion: Whitney source model

- Pro:
  - Theoretically well understood
  - Computationally very fast
  - Even more realistic than the mathematical point-dipole
- Contra:
  - In (Bauer et al., 2015) still slightly less accurate than Venant, but this was solved by face and edge-based bases functions in (Pursiainen et al., 2016), however, on the cost of a larger extent

# Structure of the lecture

- Convergence analysis for FEM subtraction approach (sections 6.5.1-6.5.3 of lecture scriptum)
- Other source models (section 6.5.4 of lecture scriptum)
- Overview: Multi-layer sphere model (section 6.2 of lecture scriptum)
- Forward modeling results
- The local subtraction approach

SIAM J. SCI. COMPUT.
Vol. 0, No. 0, pp. B1–B30



# THE LOCAL SUBTRACTION APPROACH FOR EEG AND MEG FORWARD MODELING*

MALTE B. HÖLTERSHINKEN†, PIA LANGE‡, TIM ERDBRÜGGER†,
YVONNE BUSCHERMÖHLE§, FABRICE WALLOIS¶, ALENA BUYX‖,
SAMPSA PURSIAINEN#, JOHANNES VORWERK††, CHRISTIAN ENGWER‡‡, AND
CARSTEN H. WOLTERS†

**Abstract.** In FEM-based electroencephalography (EEG) and magnetoencephalography (MEG) source analysis, the subtraction approach has been proposed to simulate sensor measurements generated by neural activity. While this approach possesses a rigorous foundation and produces accurate results, its major downside is that it is computationally prohibitively expensive in practical applications. To overcome this, we developed a new approach, called the local subtraction approach. This approach is designed to preserve the mathematical foundation of the subtraction approach, while also leading to sparse right-hand sides in the FEM formulation, making it efficiently computable. We achieve this by introducing a cut-off into the subtraction, restricting its influence to the immediate neighborhood of the source. We perform validation in multilayer sphere models where analytical solutions exist. There, we demonstrate that the local subtraction approach is vastly more efficient than the subtraction approach. Moreover, we find that for the EEG forward problem, the local subtraction approach is less dependent on the global structure of the FEM mesh when compared to the subtraction approach. Additionally, we show the local subtraction approach to rival, and in many cases even surpass, the other investigated approaches in terms of accuracy. For the MEG forward problem, we show the local subtraction approach and the subtraction approach to produce highly accurate approximations of the volume currents close to the source. The local subtraction approach thus reduces the computational cost of the subtraction approach to an extent that makes it usable in practical applications without sacrificing the rigorousness and accuracy the subtraction approach is known for.

# The local subtraction approach

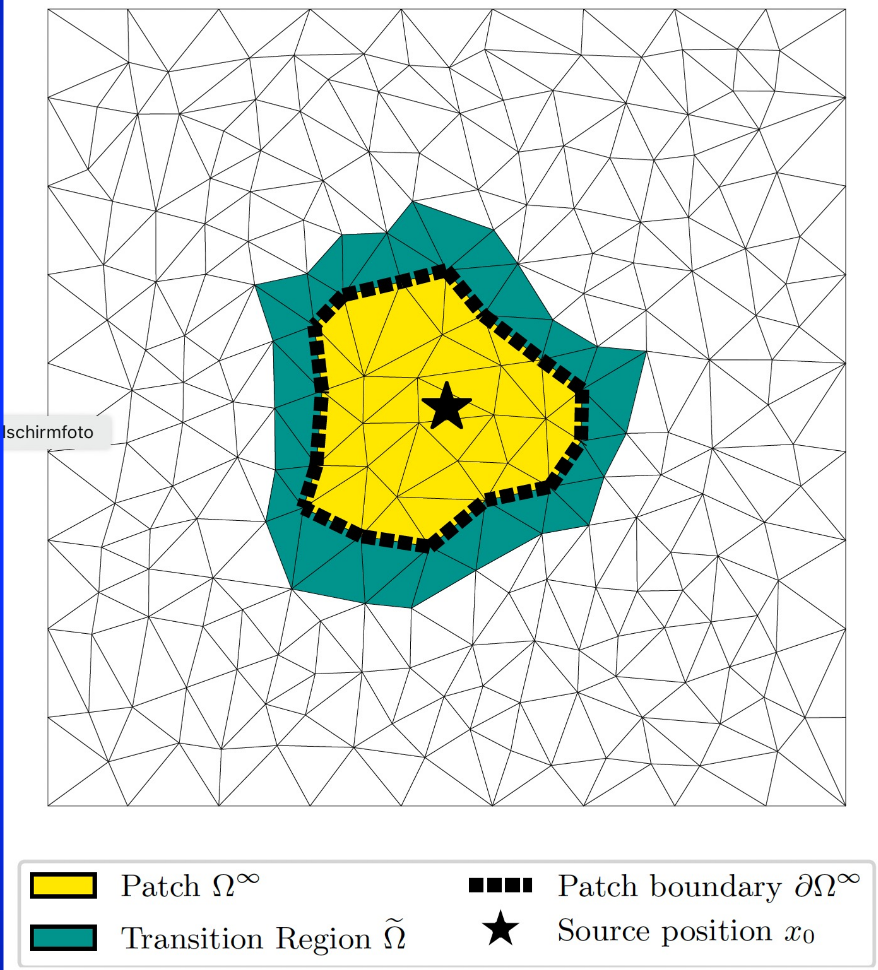


Fig. 1. 2-dim. visualization of a realization of the construction described in lemma 1. The whole square is $\boldsymbol{\Omega}$. In the yellow region we have $\boldsymbol{\chi} = \mathbf{1}$, in the white region we have $\boldsymbol{\chi} = \mathbf{0}$.

$$u^c := u - \chi \cdot u^\infty. \tag{4}$$

[Höltershinken, Lange,…, Engwer & Wolters, *SIAM SISC*, 2024]

# The local subtraction approach

Define a bilinear form $a : H^1(\Omega) \times H^1(\Omega) \to \mathbb{R}$ by

$$a(w, v) = \int_\Omega \langle \sigma \nabla w, \nabla v \rangle \, dV \tag{7}$$

and a linear form $l : H^1(\Omega) \to \mathbb{R}$ by

$$\begin{aligned} l(v) = &- \int_{\widetilde{\Omega}} \langle \sigma \nabla \left( \chi \cdot u^\infty \right), \nabla v \rangle \, dV \\ &- \int_{\partial\Omega^\infty} \langle \sigma^\infty \nabla u^\infty, \eta \rangle v \, dS - \int_{\Omega^\infty} \langle \sigma^c \nabla u^\infty, \nabla v \rangle \, dV, \end{aligned} \tag{8}$$

where $\eta$ is the unit outer normal of $\Omega^\infty$. Then the *continuous Galerkin localized subtraction approach* is given by the problem of finding $u^c \in H^1(\Omega)$ such that for all $v \in H^1(\Omega)$ we have $a(u^c, v) = l(v)$.

[Höltershinken, Lange,…, Engwer & Wolters, *SIAM SISC*, 2024]
[Beltrachini, *J Neur Eng*, 2019]

# The local subtraction approach

Finally, we want to elaborate on the computation of the FEM right-hand side. Let $K$ be a mesh element and $F$ a face of a mesh element

we need to compute integrals of the form

$$I_P = \int_K \langle \sigma^c \nabla u^\infty, \nabla \varphi \rangle \, dV, \tag{11}$$

$$I_S = \int_F \langle \sigma^\infty \nabla u^\infty, \eta \rangle \varphi \, dS, \tag{12}$$

$$I_T = \int_K \langle \sigma \nabla \left( \chi \cdot u^\infty \right), \nabla \varphi \rangle \, dV \tag{13}$$

We call $I_P$ a *patch integral*, $I_S$ a *surface integral* and $I_T$ a *transition integral*.

In the case of isotropic $\sigma^\infty$ and piecewise affine trial functions on tetrahedral meshes, analytical expressions for the patch and surface integrals were derived

[Höltershinken, Lange,…, Engwer & Wolters, *SIAM SISC*, 2024]

# The local subtraction approach

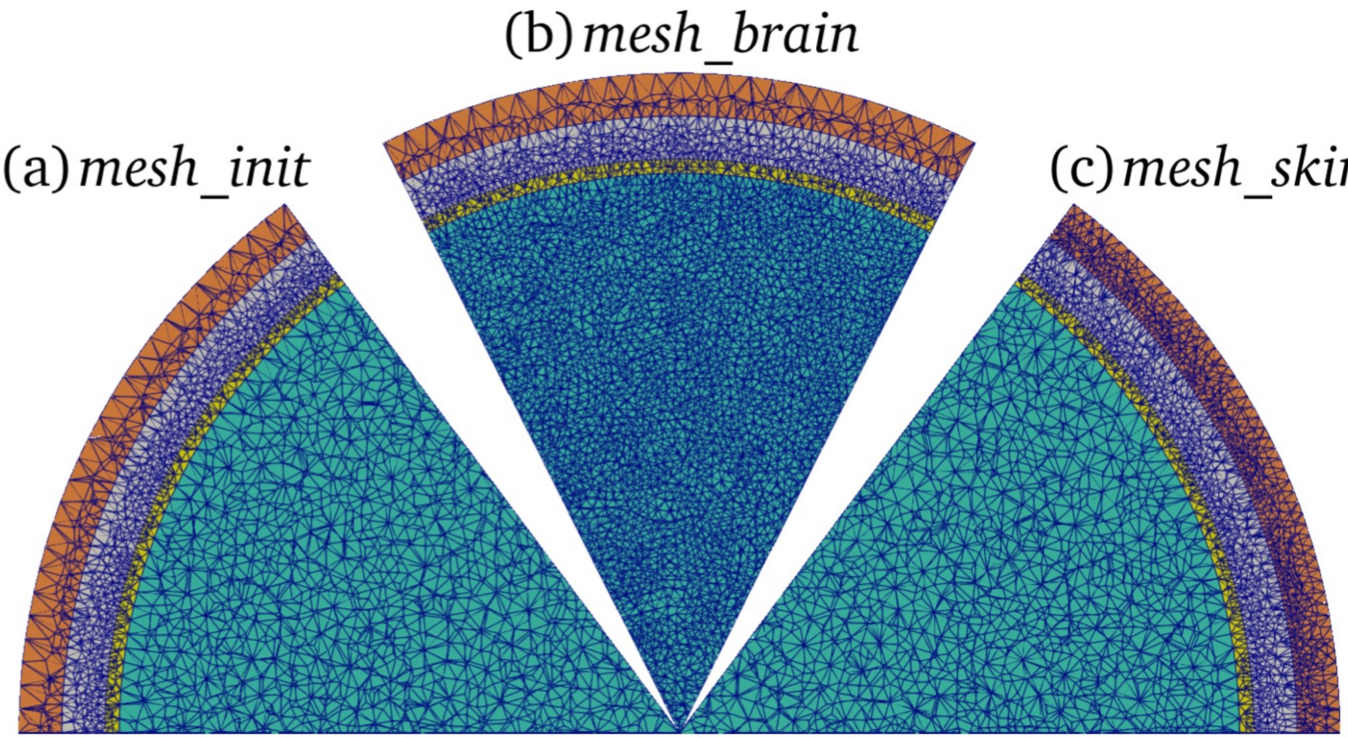


Figure 3: Circular sections of the meshes used in the numerical tests. (a) shows the initial mesh with a high concentration of nodes in the CSF and skull compartment. (b) shows the mesh from (a) after refining the brain compartment. (c) shows the mesh from (a) after refining the skin compartment. Mesh (a) consists of ca. 800k nodes, mesh (b) consists of ca. 1.8 million nodes and mesh (c) consists of ca. 1.3 million nodes.

[Höltershinken, Lange,…, Engwer & Wolters, *SIAM SISC*, 2024]

# The local subtraction approach

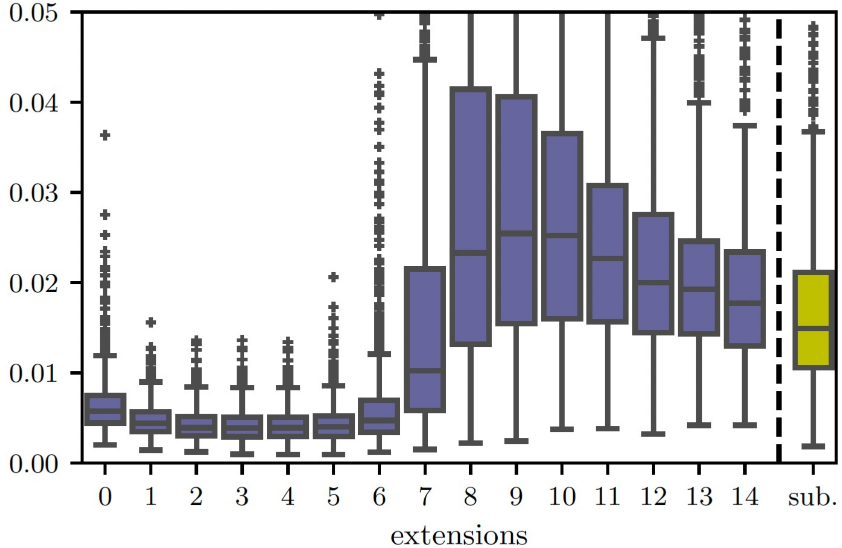


Fig. 4. Relative error in the EEG case for 1000 tangential dipoles at 0.99 eccentricity for different numbers of vertex extensions during patch construction, computed using *mesh_init*. The rightmost yellow boxplot shows the errors when employing the analytical subtraction approach from [10].

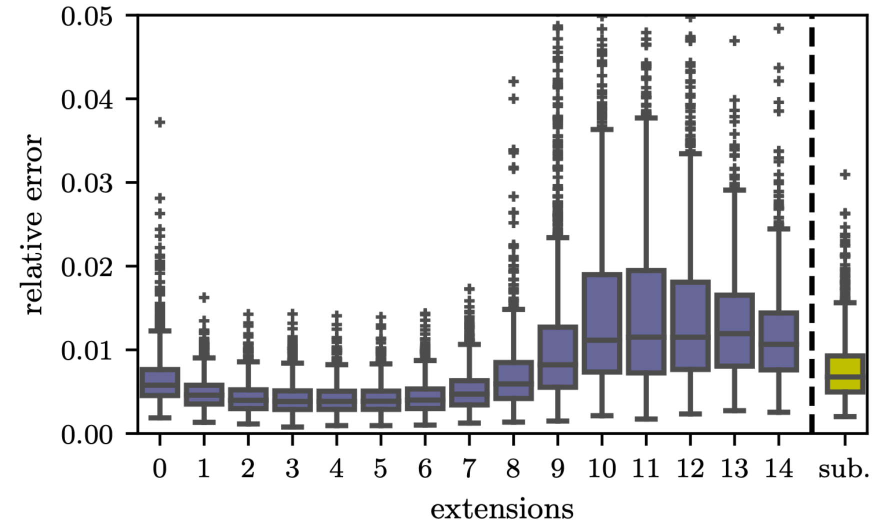


Figure F.2: Relative error in the EEG case for 1000 tangential dipoles at 0.99 eccentricity for different numbers of vertex extensions during patch construction, computed using *mesh_skin* (see Figure 3(c)). The rightmost yellow boxplot shows the errors when employing the analytical subtraction approach from [14].

# The local subtraction approach

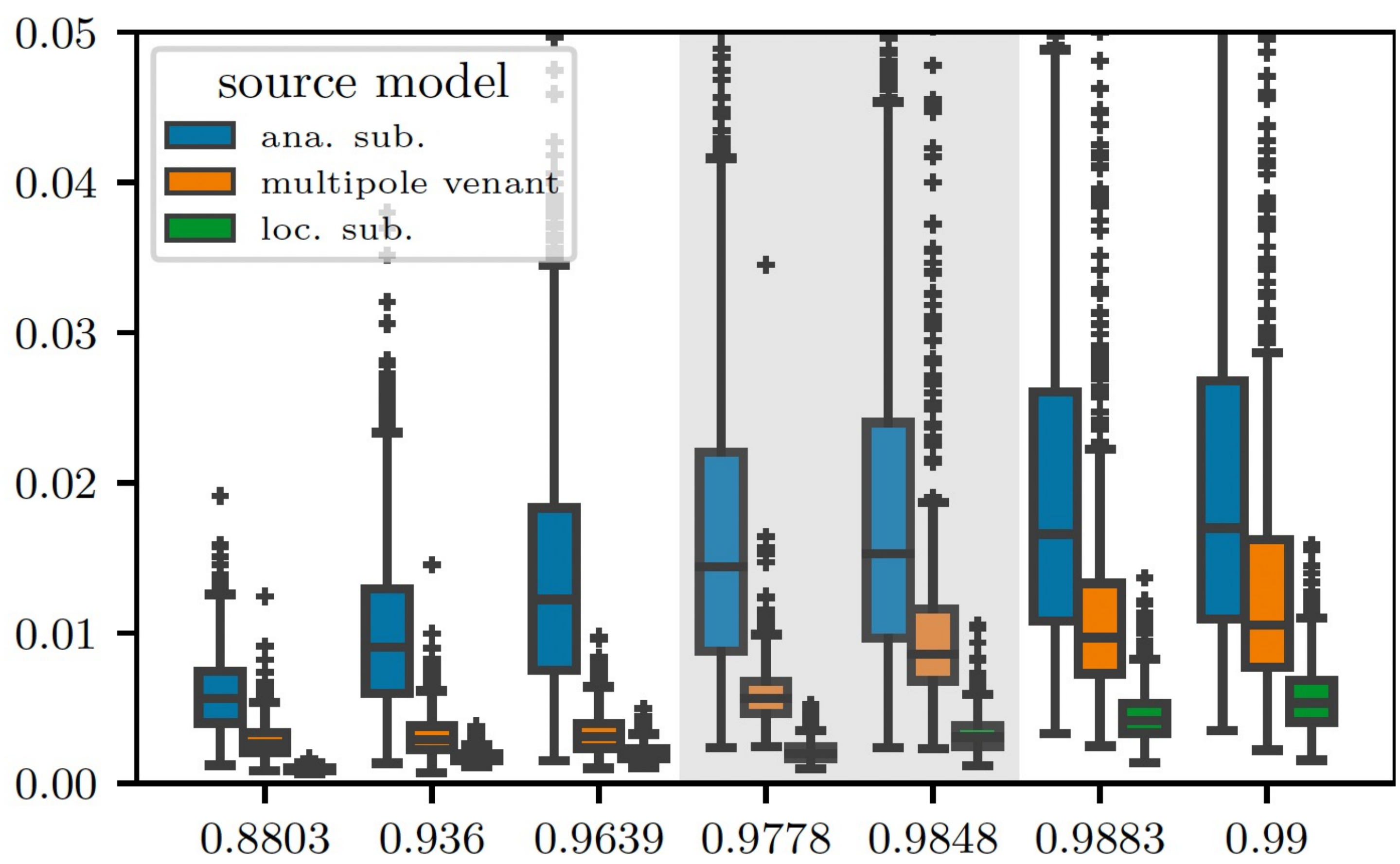


Fig. 5. Accuracy comparison of EEG forward simulations using the subtraction, multipolar venant, and localized subtraction potential approaches for radial dipoles at different eccentricities using *mesh_init*. The $y$-axis shows the relative error. The physiologically relevant sources at 1-2mm distance from the CSF are highlighted.

[Höltershinken, Lange,…, Engwer & Wolters, *SIAM SISC*, 2024]

# The local subtraction approach

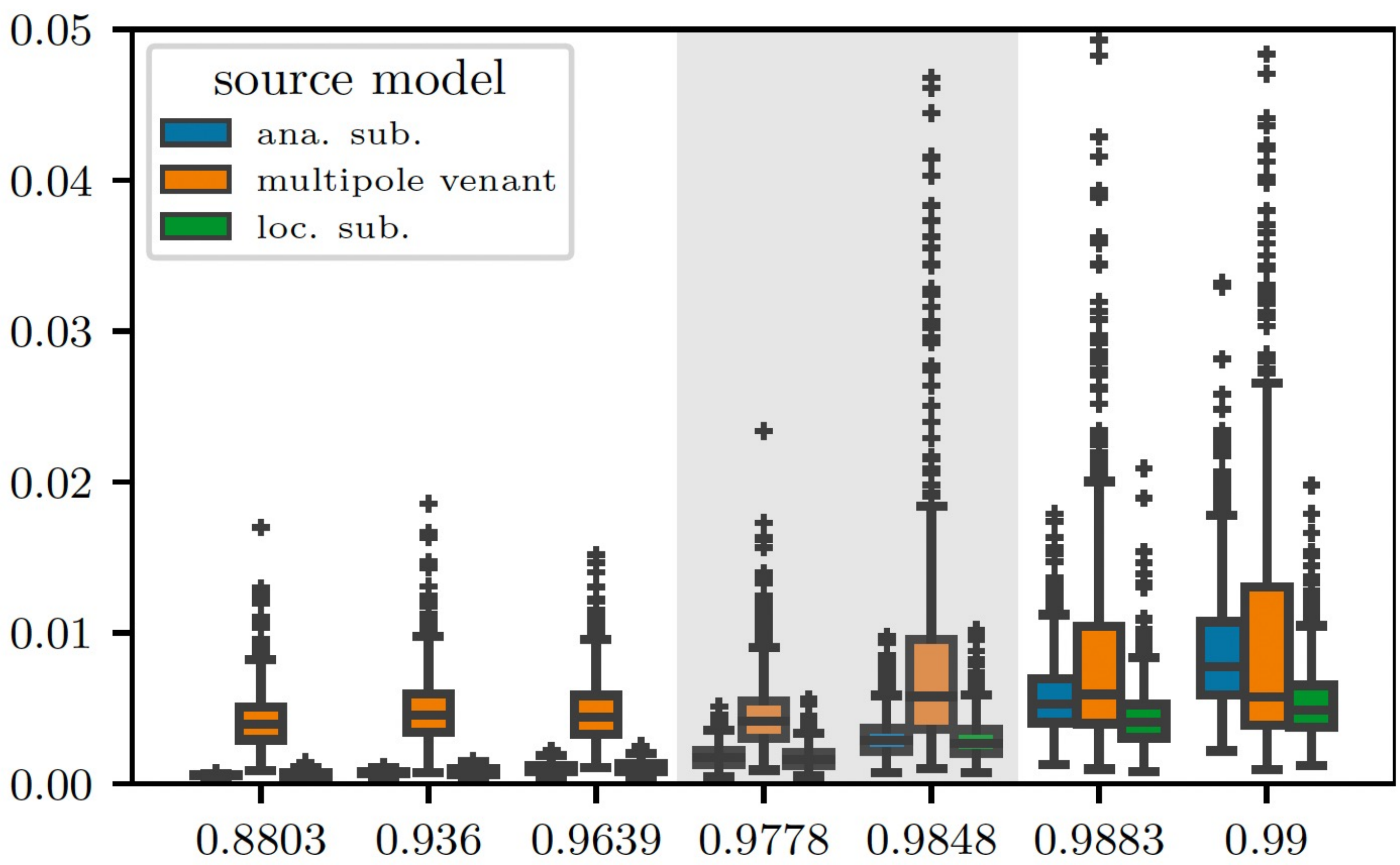


Fig. 6. Accuracy comparison of MEG forward simulations using the subtraction, venant, and localized subtraction potential approaches for tangential dipoles at different eccentricities using *mesh_init*. The $y$-axis shows the relative error. The physiologically relevant sources at 1-2mm distance from the CSF are highlighted.

[Höltershinken, Lange,…, Engwer & Wolters, *SIAM SISC*, 2024]

# The localized subtraction approach

TABLE II

FORWARD SIMULATION TIMES FOR $1000$ SOURCES AT AN ECCENTRICITY OF $0.99$ IN *mesh_init*

| Approach | loc. sub. | sub. | mul. venant |
|---|---|---|---|
| EEG time (s) | 0.93 | 655 | 0.02 |
| MEG time (s) | 13 | 18925 | 0.04 |

TABLE III

FORWARD SIMULATION TIMES FOR $1000$ SOURCES AT AN ECCENTRICITY OF $0.99$ IN *mesh_brain*

| Approach | loc. sub. | sub. | mul. venant |
|---|---|---|---|
| EEG time (s) | 0.96 | 1396 | 0.02 |
| MEG time (s) | 6.8 | 43175 | 0.04 |

# Thank you for your attention!


SIM-NEURO work-group at IBB